

Copyright
by
Yichuan Niu
2015

The Dissertation Committee for Yichuan Niu
certifies that this is the approved version of the following dissertation:

Quantifying and Mitigating Wind Power Variability

Committee:

Surya Santoso, Supervisor

Aristotle Arapostathis

Ross Baldick

Raul G. Longoria

Mohit Tiwari

Quantifying and Mitigating Wind Power Variability

by

Yichuan Niu, B.E., M.E.

DISSERTATION

Presented to the Faculty of the Graduate School of
The University of Texas at Austin
in Partial Fulfillment
of the Requirements
for the Degree of

DOCTOR OF PHILOSOPHY

THE UNIVERSITY OF TEXAS AT AUSTIN

December 2015

Dedicated to my beloved parents and wife for their unconditioned support
and unwavering faith on me.

Acknowledgments

This work has been finalized with the ardent help and meticulous supervision from Dr. Surya Santoso, my academic supervisor, at the University of Texas at Austin. I herein would like to heartily express my thanks to him for his guidance and support during my entire study and research process. When I joined Dr. Santoso's group in fall of 2012, I was passionate, yet inexperienced, to the academic world. He managed to enlighten me and provided new ideas for my research. These ideas finally became my topics and achievements presented in this work. In addition to my study, I have benefitted from and been influenced by Dr. Santosos rigorous and dedicated attitude towards academic research, which I believe will be the paradigm in my life.

I am very grateful to my committee members, Dr. Aristotle Arapostathis, Dr. Ross Baldick, Dr. Raul G. Longoria, and Dr. Mohit Tiwari for agreeing to serve on my committee and for valuable suggestions, advice, and inputs about my work.

I would also like to thank all the staff members at the Electrical and Computer Engineering Department. Personally, I especially thank Melanie Gulick, who helped me countless times and might be most acknowledged by ECE students. Her help is always the warmest backing for international students like me who would feel alone and helpless when facing difficult situations.

Many thanks go out to my lab colleagues, classmates, and people who shared their ideas and valuable thinking with me.

Last, but certainly not least, my sincere gratitude goes out to my parents and my wife who endowed their unconditioned support and unwavering faith to me during my hardest time. Performing research towards a PhD degree is very stressful and sometimes makes one feel desperate. Encouragement from my family members heartened me towards optimism when I was frustrated. I am grateful to you all.

Quantifying and Mitigating Wind Power Variability

Publication No. _____

Yichuan Niu, Ph.D.

The University of Texas at Austin, 2015

Supervisor: Surya Santoso

Understanding variability and unpredictability of wind power is essential for improving power system reliability and energy dispatch in transmission and distribution systems. The research presented herein intends to address a major challenge in managing and utilizing wind energy with mitigated fluctuation and intermittency. Caused by the varying wind speed, power variability can be explained as power imbalances. These imbalances create power surplus or deficiency in respect to the desired demand. To ameliorate the aforementioned issue, the fluctuating wind energy needs to be properly quantified, controlled, and re-distributed to the grid.

The first major study in this dissertations is to develop accurate wind turbine models and model reductions to generate wind power time-series in a laboratory time-efficient manner. Reliable wind turbine models can also perform power control events and acquire dynamic responses more realistic to a real-world condition. Therefore, a Type 4 direct-drive wind turbine with

power electronic converters has been modeled and designed with detailed aerodynamic and electric parameters based on a given generator. Later, using averaging and approximation techniques for power electronic circuits, the order of the original model is lowered to boost the computational efficiency for simulating long-term wind speed data.

To quantify the wind power time-series, efforts are made to enhance adaptability and robustness of the original conditional range metric (CRM) algorithm that has been proposed by literatures for quantitatively assessing the power variability within a certain time frame. The improved CRM performs better under scarce and noisy time-series data with a reduced computational complexity. Rather than using a discrete probability model, the improved method implements a continuous gamma distribution with parameters estimated by the maximum likelihood estimators.

With the leverage from the aforementioned work, a wind farm level behavior can be revealed by analyzing the data through long-term simulations using individual wind turbine models. Mitigating the power variability by reserved generation sources is attempted and the generation scenarios are generalized using an unsupervised machine learning algorithm regarding power correlations of those individual wind turbines. A systematic blueprint for reducing intra-hour power variations via coordinating a fast- and a slow- response energy storage systems (ESS) has been proposed. Methods for sizing, coordination control, ESS regulation, and power dispatch schemes are illustrated in detail. Applying the real-world data, these methods have been demonstrated

desirable for reducing short-term wind power variability to an expected level.

Table of Contents

Acknowledgments	v
Abstract	vii
List of Tables	xiv
List of Figures	xv
Chapter 1. Introduction	1
1.1 Background and Motivation	1
1.2 Research Objective and Tasks	4
1.2.1 Task I: Concepts and Designs	4
1.2.2 Task II: Implementations and Simulations	7
1.3 Research Approach and Contributions	9
1.3.1 Development of Direct-Drive Wind Turbine Model in Time Domain	9
1.3.2 Development of Reduced Order Simulation Models	10
1.3.3 Improvement of the Computational Algorithm for Quantifying Wind Power Variability	10
1.3.4 Employment of Reserved Generation Sources and Energy Storage Systems to Mitigate Wind Power Variations	11
Chapter 2. Modeling and Parametric Design of Direct-Drive Wind Turbines	14
2.1 System Configuration	15
2.2 Blade Aerodynamic Design	16
2.3 Design of Electrical and Control Parameters	19
2.3.1 DC Link	20
2.3.1.1 DC-link Voltage V_{dc}	20
2.3.1.2 Capacitor Size C	21

2.3.2	Grid-Connected Inverter	23
2.3.2.1	Limits for PI Controllers $G_{V_{dc}}(s)$, $G_{i_d}(s)$ and $G_{i_q}(s)$	23
2.3.2.2	AC Inductance L_{ac}	25
2.3.3	Machine-Side Converter	27
2.3.3.1	Limits for PI Controllers $G_{\omega_m}(s)$, $G_{i_{sd}}(s)$ and $G_{i_{sq}}(s)$	28
2.3.3.2	Machine-Side Filter L_f	29
2.4	Design Verificaiton and Simulation	30
2.5	Summary	31
Chapter 3. Model Reduction, Validation and Analysis of Direct-Drive Wind Turbine		35
3.1	Possibility of Modeling Reduction Regarding Desired Time Scale	37
3.1.1	Long-Term Operations	37
3.1.2	Transient Responses	38
3.2	Switching-Function and Switching-Average Models	39
3.2.1	Switching-Function Model	40
3.2.2	Switching-Average Model	41
3.3	Quasi-Dynamic Model	43
3.3.1	Model Derivation	45
3.3.2	Reduced Controllers	47
3.4	Validation of the Model Reductions	49
3.4.1	Case 1: Steady-State Operation	49
3.4.2	Case 2: Response during a Symmetrical Fault	50
3.4.3	Case 3: Model Validation Using Data from NREL	54
3.5	Summary	57
Chapter 4. Quantification of Wind Power Variability		59
4.1	The Conditional Range Metric in Wind Power Variability	61
4.1.1	Concept of Quantifying Wind Power Variability	61
4.1.2	Definition of the Conditional Range Metric	63
4.1.3	Computational Methodology of CRM and CR	64
4.2	Conditional Range Metric for Scarce and Noise Data	67

4.2.1	Probability Model of Deviation Series	67
4.2.2	Parameter Estimation for the Probability Model	71
4.2.3	Reduction on the Joint Probability Density Matrix	75
4.3	Bayesian Inference for the Probability Model	80
4.3.1	Determination of the Prior	82
4.3.2	Posterior Analysis	84
4.4	Performance of the sCRM under Scarce and Noisy Data	89
4.5	Summary	96
Chapter 5. Evaluation of Quasi-Dynamic Wind Turbine Model and sCRM		98
5.1	Introduction and Literature Study	99
5.2	Wind Turbine Level Simulation	101
5.3	Wind Farm Level Simulation	108
5.3.1	Simulation of Small Wind Farms and Reserved Generation Sources	108
5.3.2	Analysis of Correlation	112
5.4	Scenario Generation of Wind Farms	115
5.4.1	Unsupervised Machine Learning for Clustering Wind Power Generation Data	117
5.4.1.1	K -Means Clustering Algorithm	118
5.4.1.2	Random Initialization of K -Means Algorithm	120
5.4.2	Principal Component Analysis	121
5.4.3	Generalizing Wind Power Generation Scenarios	123
5.5	Summary	129
Chapter 6. Sizing and Coordinating Fast- and Slow-Response Energy Storage Systems to Mitigate Wind Power Variations		130
6.1	Wind Power Data and ESS Lifetime Evaluation	133
6.1.1	Wind Power Time Series	133
6.1.2	Battery Lifetime Assessment of the Fast-Response ESS	134
6.2	Generic ESS Modeling and Power Forecasts	137
6.2.1	A Generic ESS Model	137

6.2.2	Wind Power Forecast	138
6.2.2.1	Persistence forecast	139
6.2.2.2	Power step-change (PSC) forecastt	140
6.3	Sizing the ESSs	141
6.3.1	Sizing the Power Capacity Ratings P_{ess}	141
6.3.2	Sizing the Energy Capacity Ratings E_{ess}	143
6.3.2.1	Determining Energy Capacity of the Slow-Response ESS	144
6.3.2.2	Determining Energy Capacity of the Fast-Response ESS	145
6.4	Control Methods and Power Dispatch Schemes	147
6.4.1	System Configurations	148
6.4.1.1	Series Regulation	148
6.4.1.2	Parallel Regulation	149
6.4.2	ESS Control Methods	151
6.4.2.1	SOC Band Control (BC)	151
6.4.2.2	Fuzzy Control (FC)	152
6.5	Result Evaluation and Analysis	153
6.6	Summary	157
Chapter 7. Conclusions		160
Appendices		164
Appendix A. Machine and Converter Data		165
Bibliography		166
Vita		186

List of Tables

2.1	Design Requirements and Systems Actual Response	34
3.1	Lifetime Depreciation Assessment of the Fast-Response ESS	52
4.1	Relative Estimation Errors Between MLE and BE [%]	89
4.2	<i>LC</i> Values at Different Coverage Rates	96
5.1	Averaged CR from a 95% Coverage Rate	104
5.2	Averaged CR from Simulated Wind Farm without Reserved Generation Source	110
5.3	Averaged CR from Distributed and Centralized Generation Sources	112
5.4	Minimum Cost, Valid Clusters and Retained Variance for Gen- eralized Scenarios	126
5.5	10-Scenario Power Outputs and Corresponding Probabilities af- ter Performing PCA	128
6.1	Power Ratings of the Fast-Response ESS (p.u.)*	143
6.2	Energy Capacity Ratings of the Slow-Response ESS (p.u.h)*	145
6.3	Energy Capacity Ratings of the Fast-Response ESS (p.u.h)	147
6.4	Optimal Ranges for SOC_C and SOC_D	152
6.5	Operational Independence of Control Methods	154
6.6	Lifetime Depreciation Assessment of the Fast-Response ESS	156

List of Figures

1.1	Demonstration of objective and demonstrations in reducing wind power variability. Task I: Concepts and Designs	6
1.2	Demonstration of objective and demonstrations in reducing wind power variability. Task II: Implementations and Simulations	8
2.1	Circuit configuration of a direct-drive Type 4 wind turbine	16
2.2	Characteristics of C_p regarding various pitch angle β and tip speed ratio λ ($\lambda = R\omega_m/V_w$)	17
2.3	Maximum power point tracking curve for wind speed under the cut-in speed.	19
2.4	Control block of rotor pitch angle β	19
2.5	Control block diagram of the grid-connected inverter	24
2.6	Control block diagram of the Machine-Side Converter	28
2.7	Steady-state performance of the designed wind turbine. (a) Power curve and blade performance versus the wind speed; (b) Pitch angle and rotor speed versus wind speed.	32
2.8	Voltages and currents under rated wind speed operation. (a) DC-link voltage; (b) Grid voltage and current of phase A	33
3.1	Time-scale boundaries between dynamics and steady-state operations in a wind turbine system.	39
3.2	Reduced power circuit of the switching-function model. This topology is then used to derive the switching-average model and quasi-dynamic model.	42
3.3	Reduced controller for the DC-link voltage. It controls the active power following from the grid to the wind turbine system ignoring the reactive component.	47
3.4	Reduced controller for the PMSM. The active current flowing into the machine is converted into electromagnetic torque using the torque equation and energizes the rotor-blades mass model.	48
3.5	Block diagram of the quasi-dynamic Type 4 wind turbine model. With reduced electrical system and non-reduced aerodynamics, it is capable for capturing an accurate steady-state information and major dynamics as well as control events.	49

3.6	Steady-state operation. (a) DC-link voltage. Ripples can be represented by the full and switching-function models but not by the switching-average and quasi-dynamic models; (b) Grid line current of phase A. Current harmonics at switching frequency can be found in full and switching-function models and is the root cause for the DC ripples and power oscillation; (c) Active power generated. The power is recorded by a power meter with a smoothing constant to approach the real-world situation.	51
3.7	Response in a symmetrical fault. (a) DC-link voltage. The over-voltage is due to the power difference between the input (power captured by the rotor blades) and the output (power fed into the grid); (b) Grid line current of phase A. The current swell is caused by ‘pumping’ the excessive power into the grid during and after the fault; (c) Active power generated. This power profile is a typical response of the modeled Type 4 wind turbine, however, it can be modified by different control strategies.	53
3.8	Comparison of power released by NREL and power simulated by the quasi-dynamic model. The analysis is executed using the data at location ID 12 in January 2004 in [1].	57
3.9	Comparison of aggregated power from three wind turbines of ID 12, ID 39 and ID 110. Sub-figure (a) shows the working condition of power ramping up and down in a fluctuated wind speed while sub-figure (b) illustrates the plateau region with a relatively steady state. The base is 30 MW.	58
4.1	Wind power variability related to a time window. Production level l_j and power-deviation series are derived through the moving average of all sampled data points.	62
4.2	Illustration of fitting the deviation series into gamma distributions. They are calculated with $k = 60$ min while the resolution for l_j is 0.01 p.u. The data is chosen from a_{60} and b_{60} with $l_j = 0.3$ p.u. and $l_j = 0.9$ p.u.	74
4.3	Probability density model using gamma distribution approach through the entire production level l_j with a resolution of 0.01 p.u. The length of the analyzed observation interval is $k = 60$ min.	76
4.4	Three dimensional display of the upper and lower deviation through the entire coverage rate p and production level l_j . The length of the observation interval is $k = 60$ min.	79

4.5	Conditional range estimation through the entire domain of production level l_j and coverage rate p with an observation interval $k = 60$ min. The red mesh is M_{up60} calculated from g_{b60} while the blue mesh represents M_{low60} derived from g_{a60}	81
4.6	Comparison of α and β estimation results from MLE and BE, the left vertical axis is the value of α while the right vertical axis denotes the value of β . The resolution of the production level is increased to 0.1 p.u. for a better visual inspection. The observation interval is still $k = 60$ min.	88
4.7	Comparisons of computational methodologies between oCRM and sCRM. oCRM uses a discrete quantile model, while sCRM employs the continuous gamma distribution as its probability model.	90
4.8	The conditional range is plotted from 1-minute data resolution to 30 min data resolution for both oCRM. The coverage rate p , observation interval k , and the production level resolution are $p = 90\%$, $k = 60$ min and 0.01 p.u., respectively.	92
4.9	The conditional range is plotted from 1-minute data resolution to 30 min data resolution for both sCRM. The coverage rate p , observation interval k , and the production level resolution are $p = 90\%$, $k = 60$ min and 0.01 p.u., respectively.	93
4.10	Conditional range comparison of oCRM and sCRM under 2% noise points in the upper and lower deviation series with a coverage rate of 98% and an observation interval $k = 60$ min. . .	95
4.11	Correction factor under different percentages of noise points with coverage rates $p = 90\%$, 92%, 94%, 96%, 98%.	96
5.1	Reducing and managing wind power variability on a wind turbine level	102
5.2	Conditional range metric estimations using 0.35-p.u. and 0.65-p.u. generation sources with $p = 95\%$ and $k = 60$ min	105
5.3	Averaged conditional range in respect to generation source rating and length of averaged hours with $p = 95\%$ and $k = 60$ min	107
5.4	Two configurations for operating generation sources. The total power ratings are the same for both layouts.	109
5.5	Conditional range estimation for single wind turbines and wind farm with $p = 95\%$ and $k = 60$ min.	111
5.6	Conditional range using distributed and centralized generation sources with $p = 95\%$ and $k = 60$ min.	112

5.7	Correlation coefficients calculated from wind speed, power generated by quasi-dynamic model and reserved generation source	113
5.8	Correlation matrix among ID 12, ID 39 and ID 110	115
5.9	Illustration of clustering generation scenarios for two wind turbines. The original 2000 scenarios are generalized into 5 basic patterns.	117
5.10	An example of clustering data using K -means algorithm.	120
5.11	Projecting 2-D wind power data onto a 1-D domain. The two data sources must be correlated.	122
5.12	Wind power data samples to be generalized.	124
5.13	Generalizing wind power generation into 10, 50, and 100 scenarios with their respective occurrence probability.	127
5.14	Comparison of reduced power dimension from PCA and actual power from aggregations.	128
6.1	Battery lifetime cycle versus DOD in logarithmic domain. This curve is derived by linear extrapolating the data from manufacturer.	135
6.2	An example of counting incomplete ESS charge/discharge cycles in a complex working condition using the rainflow algorithm: (a) Input SOC time-series data; (b) Incomplete cycles counted by rainflow algorithm.	136
6.3	Demonstration of persistence forecast and PSC forecast with a prediction period of $T = 120$ min.	140
6.4	Quantified wind power variability from the raw wind power, persistence-forecasted power, and PSC-forecasted power. A larger CRM can be found from PSC method due to its sudden power change between consecutive steps.	142
6.5	Sizing power ratings of the fast-response ESS using CR and w_j . The ESS size is determined by the expectation of CR for $k = 30$ min and $p = 90\%$.	144
6.6	Incapability of the fast-response ESS in supporting energy deficiency or absorbing the surplus. This incapability will increase the variability in terms a high rate power change.	148
6.7	Series power regulation layout with the slow-response ESS at the upstream.	150
6.8	Parallel power regulation layout with a rate separator.	151
6.9	Output surface of the fuzzy control (FC) membership functions.	154

6.10	Comparison of wind power variability mitigation effectiveness with methods in Table 6.5.	156
6.11	CR from series regulation with persistence and PSC power forecasts: (a) CR from persistence forecast; (b) CR from PSC forecast.	158

Chapter 1

Introduction

This chapter presents the motivation and background on quantifying and mitigating short-term wind power variability. In addition, it describes the research objective, scope of work, and contributions. Section 1.1 sets the notion of researching wind power via dynamical modeling. Control schemes and incorporation of energy storage systems can, thereby, be investigated based on the system models. Power variability quantification metrics will be proposed to evaluate the control effectiveness. The main research objective and tasks are stated in Section 1.2 with approach in Section 1.3. Original contribution and dissertation outline are also given in Section 1.3.

1.1 Background and Motivation

By the end of 2014, the installed wind power capacity has reached an unprecedented 370 GW worldwide, including 129 GW in the EU, 115 GW in China, and 66 GW in the US [2]. The increasing wind power penetration gives rise to potential problems in system stability, power quality, system protection, and, most of all, unexpected power variations.

Understanding wind power variability and unpredictability is essential

for maintaining and improving power system reliability and energy dispatch from transmission and distribution systems. Power imbalances from wind farms can be regulated in various manners [3–8]. Typically, geographical layout will ameliorate the power variations by evening out the total power throughout a widespread region according to stochastic process. Operating reserve and system reliability can, therefore, be evaluated via correlations from geographical distribution [9,10]. Further, modern wind turbines such as Type 3 or Type 4 with pitch control capability can accomplish regulations by controlling the grid-side converter and pitch. In multi-machine or network systems [11, 12], managing power output from wind turbines can dispatch power without additional infrastructure investment. Sadly, none of the aforementioned endeavors can provide additional generation capacity for specific grid demands during low wind speed. Power regulations, from this perspective, have been accomplished via energy storage systems (ESSs) and via coordination control with other power sources and unused generation capacity [4, 5, 7]. Current studies involving sizing and controlling of ESSs are mainly based on historical wind power operational data, which can be a feasible approach for system planning level designs.

In extending the usage of ESS, this work proposes system layouts and coordination control strategies for fast- and slow-response ESSs. The two types of ESSs are sized by probabilistic sizing methods from a novel variability quantifications metric. Short-term power variability can, thus, be mitigated to a desired level using a minimum ESS volume. To explore the interaction of

a wind turbine during power control and energy regulation, accurate system modeling is studied. Present models are developed based on Type 1 to Type 4 with aerodynamics, mechanical, and electrical sub-models [13–16]. The detailed modeling is capable of reproducing transients and dynamic responses, but with low computational efficiency. Due to the model complexity, data acquisitions from long-term simulations, such as producing monthly or annual power profiles, are not possible. For example, it will take more than 20 seconds to run a single instance of the Type 4 wind turbine for 1 second duration with a complete order representation in PSCADTM. Therefore, the concept of model reductions is desirable to obtain a realistic simulation for gathering long-term operational data and implementing controls.

Aiming for solutions to manage wind power variations and increasing reliability and power availability, the following aspects are, herein, investigated in order to develop a system for simulating, quantifying, and controlling the wind power variability:

1. Suitable models with a lower order of computational complexity, validated by real-world data for partial transient responses and long-term steady-state operations;
2. Approach to generalize wind power generation scenarios among wind turbines that share correlated wind speeds within a regional wind farm;
3. A method for quantifying wind power variability with a simpler computational process and improved adaptability and robustness for the field

data;

4. Optimized layouts and operational schemes for ESSs to reduce the wind power variations and imbalances with minimal ESS lifetime consumption.

1.2 Research Objective and Tasks

The objective of this dissertation is to develop theories and methodologies for controlling and regulating wind power variability and to demonstrate their efficacy through simulation. The theme of the research can be divided into two parts. Graphical demonstrations of each are illustrated in Figures 1.1 and 1.2.

1.2.1 Task I: Concepts and Designs

The concept and design begin with characterizing the variability of the wind power and by proposing a reference power profile with reduced variability. Sizing, control, and regulation methods at this stage are based on analyses of historical wind power data.

Shown in Figure 1.1, the raw wind power data $P_{raw}(t)$ with an unmitigated variability is processed by statistical methods to determine its variability measures in terms of CRM_{raw} and CR_{raw} . In Figure 1.1, the larger block in red performs variability quantification using the conditional range metric (CRM). The CRM is a state-of-the-art approach that can deliver an empirical pattern

of short-term variability via statistical models and historical time-series data. This metric is based on the general idea of characterizing a varying source by its range of outputs and predicts the power variations regarding the current production level. The conditional range CR which takes much smaller values than the wind farm rated capacity is the range of the power output determined by the length of an observation time interval and a desired coverage rate. This proposal aims to extend the CRM-based method for applications to scarce or noisy wind power data by reformulating the probability model for characterizing the power-deviation series. It improves adaptability and robustness while reducing the computational complexity.

The ultimate goal of this work is to mitigate short-term wind power variability, i.e., to reduce the intra-hour power variations of a wind farm, so that its variability can be controlled and regulated down to a desired value. With this expectation, two reference parameters are defined: desired power time-series $P_{reference}(t)$ and variability characteristics $CRM_{reference}$. Parameter $P_{reference}(t)$ is a calculated power profile, satisfying the variability requirement $CRM_{reference}$. ESSs or third-party generation sources are applied to achieve $P_{reference}(t)$. Sizing and dispatch strategies are derived based on $CRM_{reference}$ from a statistical perspective. The smoothed or variability-mitigated power output $P_{smooth}(t)$ is sent back to the CRM block to verify the effectiveness of variability mitigation technique and to update the desired power profile $P_{reference}(t)$ as well.

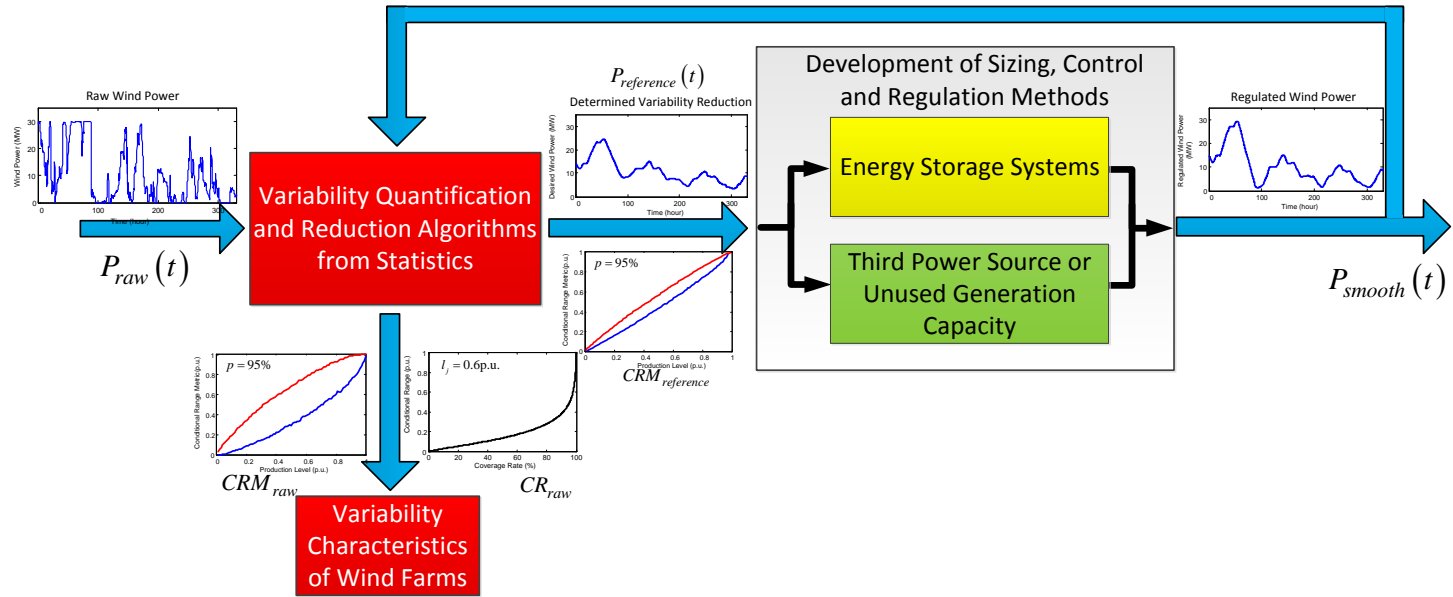


Figure 1.1: Demonstration of objective and demonstrations in reducing wind power variability. Task I: Concepts and Designs

1.2.2 Task II: Implementations and Simulations

Because the methods developed in Part I are based on data analysis, they shall be validated and proven to be feasible by simulations in the implementation stage depicted in Figure 1.2. The wind farm modeled as individual quasi-dynamic wind turbines is simulated with real-world wind speed $V_{wind,1}(t)$ through $V_{wind,n}(t)$, producing an aggregated raw power output $P_{WF}(t)$. Using the ESS sizing and dispatch strategy developed in Part I, wind turbine level and wind farm level ESSs are employed to smooth $P_{WF}(t)$. Subjects on system modeling and coordination control are investigated in this part.

Considering the-state-of-the-art in wind power technology, this work focuses on wind farms with direct-drive wind turbines. Such wind turbines possess full controllability on the rotor speed as well as independent active and reactive power control. A complete modeling of direct-drive wind turbines is investigated and designed. Parameters of blade aerodynamics, expected cut-in, rated, and cut-out wind speeds, sizes of inline inductors on the machine, grid sides, the DC capacitor, and controller limits are derived and calculated. Dynamic responses and steady-state data acquired from case studies evaluate the design validity and accuracy.

To enhance the computational efficiency for simulating wind power plants, reduced-order models are proposed. They are shown as the red blocks in Figure 1.2. The aim of these models is to develop wind farms using individual or partially aggregated turbine models with time efficiency. Reduced-order models are equipped with dynamic controls and precise energy management

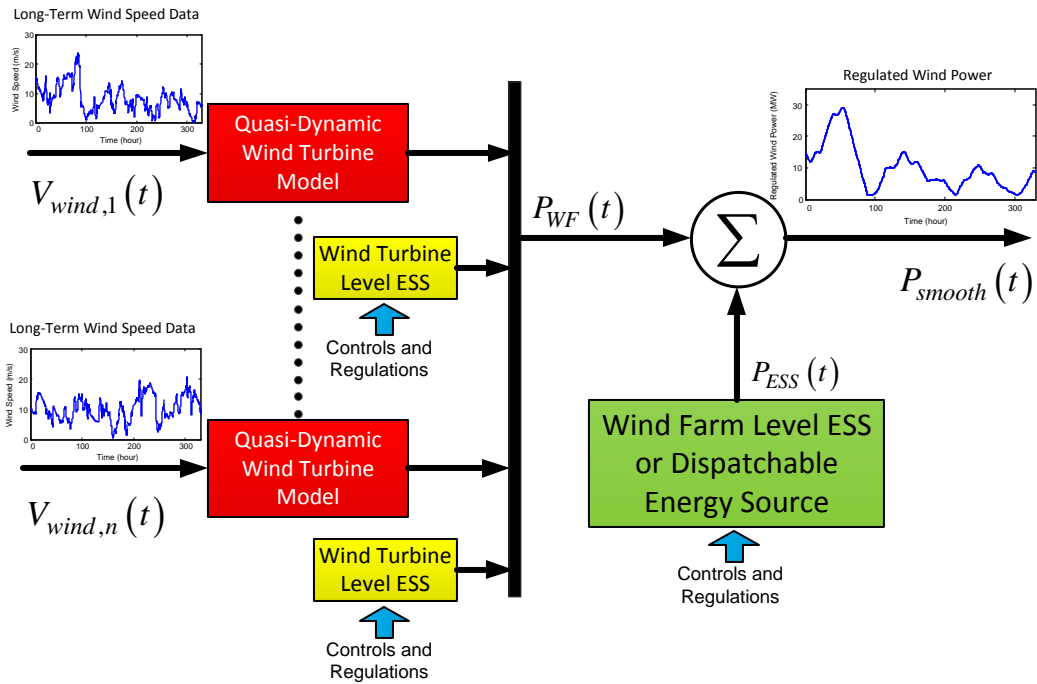


Figure 1.2: Demonstration of objective and demonstrations in reducing wind power variability. Task II: Implementations and Simulations

for regulating wind power variation. Reduced-order models also allow long-term operations of wind power plants for statistical wind power quantification. Based on the full wind turbine model, three reduced-order models are investigated through proper assumptions, linearization, and simplifications to shorten simulation runtime. They are compared in terms of performance and accuracy with respect to the full model in the time domain simulation. Despite the simplifications, the reduced-order model is responsive to wind speed change or fault events with a response time down to 1 ms.

1.3 Research Approach and Contributions

Specific research approach and contributions, which correspondingly meet the dissertation objective defined previously, are summarized in this section. Dissertation outline and chapter arrangement are also incorporated.

1.3.1 Development of Direct-Drive Wind Turbine Model in Time Domain

The first contribution of this research, presented in Chapter 2 and published in [17], is to develop direct-drive wind turbine models in time-domain. Wind turbine models with manufacturer specifications are favorable for wind power interconnection and power flow studies. Although detailed and accurate, their usages are limited by industrial non-disclosure agreements. The primary work in this section is to develop direct-drive wind turbine models with desired design parameters based on the publicly available information. Starting with rotor blade performance and permanent magnet synchronous machine data, a series of equations for determining preliminary aerodynamic and electrical design parameters of a direct-drive wind turbine with a given converter topology is presented. Serving as a case study, these equations, derived based on aerodynamic, circuit analysis, and electric machine theories, can determine blade radius, expected cut-in, rated, and cut-out wind speeds, sizes of inline inductors on machine and grid sides as well as the DC capacitor, and controller limits accurately. Researchers and practicing engineers who want to develop a wind turbine system will find this section useful as a benchmark and a basis

for initial design with complete manufacturer independence.

1.3.2 Development of Reduced Order Simulation Models

In order to simulate wind farms using individual or partially aggregated wind turbine models through long-term operations for power data acquisition, model reductions of direct-drive wind turbines are proposed in Chapter 3 to reduce computational burden and complexity. Based on the direct-drive wind turbine model, three reduced order models are developed regarding accuracy and computational efficiency. Two of these models are developed with complete system dynamics using circuit analysis. The third model is analyzed based on a perspective of system energy flow. It features a quasi-dynamic response by assuming a steady-state operation of certain variables while maintaining critical differential equations for necessary dynamics during variable wind speeds and power system faults. These materials are organized in [18]. Long-term power time-series can, subsequently, be gathered by simulating the reduced models with real-world wind speeds.

1.3.3 Improvement of the Computational Algorithm for Quantifying Wind Power Variability

Using a relatively large volume of measured wind power time-series, the conditional range metric (CRM) has been successfully employed to quantify intra-hour wind power variability. To effectively quantify wind power variability, the algorithm of the conditional range metric has been improved by reformulating its probability kernel in Chapter 4. Aiming for accuracy and

adaptability, a gamma distribution is proposed to model the power-deviation series without introducing the joint probability density matrix. The shape and inverse scale parameters α and β of the gamma distribution are calculated by the maximum likelihood estimators (MLE) at each production level. Bayesian estimators (BE) for α and β are then developed as a posterior joint distribution to calculate their expectations by taking the mean value of the paired sample points via a modified rejection sampling strategy. The match between MLE and BE indicates a valid assumption of the likelihood distribution and exact estimated parameters. Applying data from the National Renewable Energy Laboratory (NREL) and their down-sampled subsets, the efficacy of the proposed CRM with the gamma distribution approach is compared to that of the existing CRM using a quantile model. Published in [19], this improved method can estimate an output range under a certain duration and coverage rate with adaptability for scarce data up to 30 minute per sample point and a tolerance for noisy sampled data up to 10% in the power time-series. System operators can apply this metric to predict future wind power variations and prepare reserved generation. This method is also capable for access variability of other time-series such as load fluctuation analysis.

1.3.4 Employment of Reserved Generation Sources and Energy Storage Systems to Mitigate Wind Power Variations

To mitigate intra-hour wind power variability evaluated by the conditional range metric, reserved generation sources and energy storage systems are employed to compensate the wind power imbalances.

In Chapter 5, the quasi-dynamic models are simulated with a third-party generation sources to study the operation and correlation on power management. Characteristics of operating a generation source on single wind turbine and wind farm levels are outlined. Data gathered from simulations are generalized into power generation scenarios. By introducing an unsupervised machine learning algorithm, correlated generation scenarios can be grouped by an unsupervised machine learning methods. Detailed contents are included in [20].

Probabilistic-based sizing and coordination control methods for fast- and slow-response energy storage systems (ESS) are described in Chapter 6. The fast-response ESS is designed to compensate for the hourly wind power variation, whereas the slow-response ESS coordinates with the energy deficiency or surplus. Aiming for a desired coverage and optimum sizing, the ESS capacities are determined using the conditional range metric (CRM) and desired power profiles from forecasts. Considering various real-world operational requirements, two ESS configurations and control strategies are proposed for power dispatch. The validity and effectiveness of these methods are evaluated by the CRM. Lifetime depreciation of the fast-response ESS is assessed by a rainflow counting algorithm for comparison among different power dispatch schemes. Therefore, with reasonable ESS power and energy ratings, the variability-reduced power profile can be achieved regarding a minimum lifetime consumption of the fast-response ESS. With preliminary studies published in [21], this work, summarized in [22], contributes systematic designs and

implementations on ESS sizing, operating, and controlling methods regarding future power predictions. Power dispatch and regulation solutions proposed herein can be applied in reality to meet specific requirements from wind farms owners and grid operators.

Chapter 2

Modeling and Parametric Design of Direct-Drive Wind Turbines

As mentioned in Section 1.2, preliminary research must be conducted on accurately modeling wind turbines for long-term. The modeling process commences with the complete parametric design for the full model. Model reductions and validations are proposed based on this design for a more time efficient simulation subsequently. Considering the current technologies, the research subject is chosen to be a Type 4 wind turbine with direct-drive configuration and full controllability on rotor speed, DC voltage, and power factor. The objective of this chapter is to develop a series of equations as a case study to determine design parameters of a direct-drive wind turbine (Type 4) with the assumptions that the converter topology along with turbine rotor performance C_p and electric machine data are given. Starting with rotor blade performance and permanent magnet synchronous machine data, a series of equations for determining preliminary aerodynamic and electrical design parameters of a direct-drive wind turbine with a given converter topology is presented. These equations, derived based on aerodynamic, circuit analysis, and electric machine theories, can determine blade radius, expected cut-in, rated, and cut-out wind speeds, sizes of inline inductors on machine, and grid

sides and the DC capacitor, and controller limits accurately.

The wind turbine configuration is given in Section 2.1. Blade and aerodynamic information from MOD-2 turbines is introduced in Section 2.2, while Sections 2.3.2 and 2.3.3 provide mathematical models and controllers for the grid-connected and machine-side converters of the wind turbine system, respectively. Parameters of the power circuits and controllers are calculated in detail. In Section 2.4, the complete wind turbine system is modeled in PSCADTM and the designed parameters are shown to be viable by simulation results.

2.1 System Configuration

Among modern wind turbines, Type 4 direct-drive wind turbines hold an advantage in the gearless drive train, eliminating the possibility of gearbox failures experienced by other types. Furthermore, by applying a permanent magnet synchronous machine (PMSM), it is even more preferable to remove slip rings and brushes, which require continuous maintenance. Research on Type 4 wind turbines involves control schemes and converter topology designs. A full-converter wind turbine with independent active and reactive power control has been demonstrated in [14]. Literature [23] offers a multi-level configuration for wind turbine converters with the goal of increasing power and voltage ratings while reducing the total weight of the system. Control strategies for low-voltage ride-through capability during a fault condition are presented in [24].

Figure 2.1 illustrates a Type 4 direct-drive wind turbine system. The grid-side inductor L_{ac} represents a combined equivalent of transformer leakage and system short-circuit inductances, and an additional inline inductor for harmonic mitigation. The inclusion of inductor L_{ac} is necessary to account for the voltage difference between PWM and sinusoidal grid voltages. Similar to inductor L_{ac} , inductor L_f is inserted in series on the machine side to help reduce current distortions caused by switching operations [13]

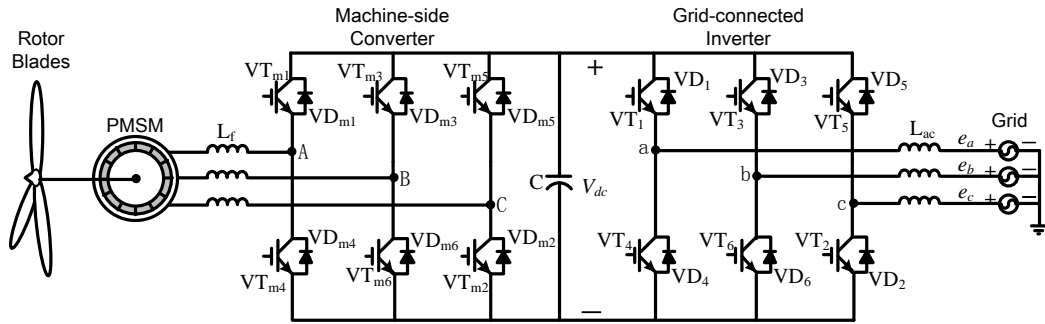


Figure 2.1: Circuit configuration of a direct-drive Type 4 wind turbine

2.2 Blade Aerodynamic Design

The direct-drive wind turbine employs a 2.0-MW non-salient pole permanent magnet synchronous machine (PMSM) with 39 pole pairs as the generator, which is interfaced to the grid through two PWM converters with back-to-back connections [15]. Blade aerodynamic performance C_p is adopted from the MOD-2 wind turbine [16]:

$$C_p = \frac{1}{2} \left(2.2369 \frac{V_w}{\omega_m} - 0.022\beta^2 - 5.6 \right) e^{-0.38028 \frac{V_w}{\omega_m}} \quad (2.1)$$

where β is the pitch angle of rotor blades in degrees. The characteristics of C_p is plotted in Figure 2.2.

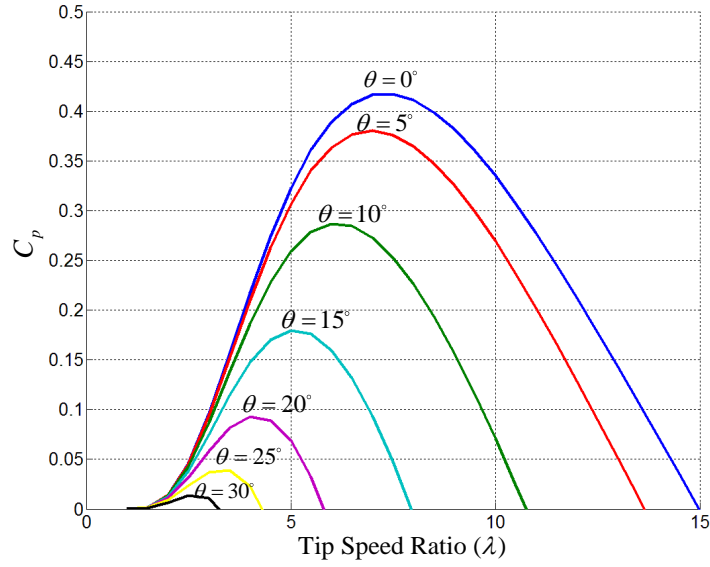


Figure 2.2: Characteristics of C_p regarding various pitch angle β and tip speed ratio λ ($\lambda = R\omega_m/V_w$)

Power extracted from the air stream follows the equation:

$$P_{rotor} = \frac{1}{2} \rho \cdot C_p \cdot \pi R_{rotor}^2 V_w^3 \quad (2.2)$$

The nominated power of the turbine rotor blades P_{rotor} , is set to 1.5 MW with a rated wind speed $V_w = 13$ m/s, despite the machine rating is 2.0 MW. Thus, the rotor radius can be calculated from (2.2):

$$R_{rotor} = \sqrt{\frac{2P_{rotor,rated}}{\rho \cdot C_{p,rated} \cdot \pi \cdot V_{w,rated}^3}} = 35.76 \text{ m}$$

The cut-in wind speed is defined when the power exacted is higher than the system power losses, while the cut-out wind speed is when the rotor blades cannot capture 1.5 MW even with $\beta = 0$ due to stall. The cut-in and cut-out wind speeds are determined empirically through simulation after the model has been developed in PSCADTM. The cut-in and cut-out wind speeds are 4 m/s and 23 m/s, respectively.

Since the Type 4 wind turbine has a full control of its rotational speed, it is preferable to achieve the maximum power point tracking (MPPT) when the wind speed is blow the cut-in speed. In order to keep (2.1) at the maximum value, the rotator speed ω_m must follow the wind speed accordingly, such that the ratio V_w/ω_m is constant. A constant tip speed ratio method can be applied as follows:

$$\lambda_{opt} = \frac{R\omega_{m,opt}}{V_w} = 6.97$$

Threrfore, ω_m can be calculated as: $\omega_{m,opt} = 0.1948V_w$.

The MPPT curve under various wind speed is shown in Figure 2.3. When V_w exceeds the rated wind speed, C_p is regulated by the pitch angle β to keep P_{rotor} at the rated power output. β is regulated by the power generated to the grid and the rotor speed for protection purposes. The pitch control block is illustrated in Figure 2.4.

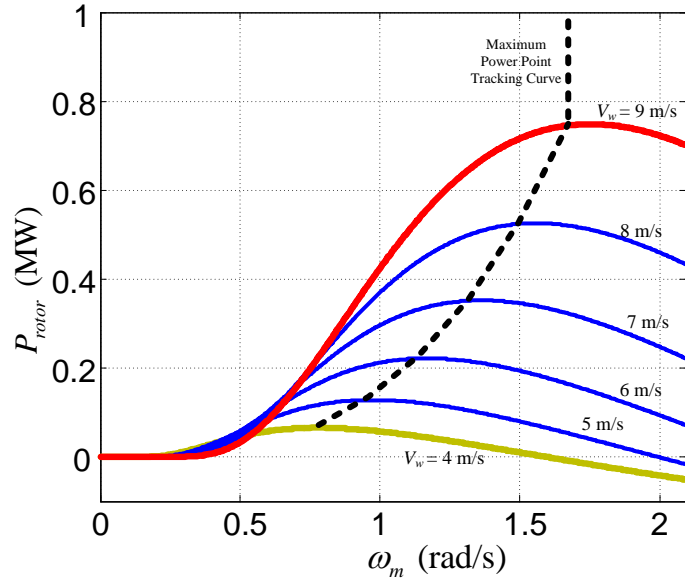


Figure 2.3: Maximum power point tracking curve for wind speed under the cut-in speed.

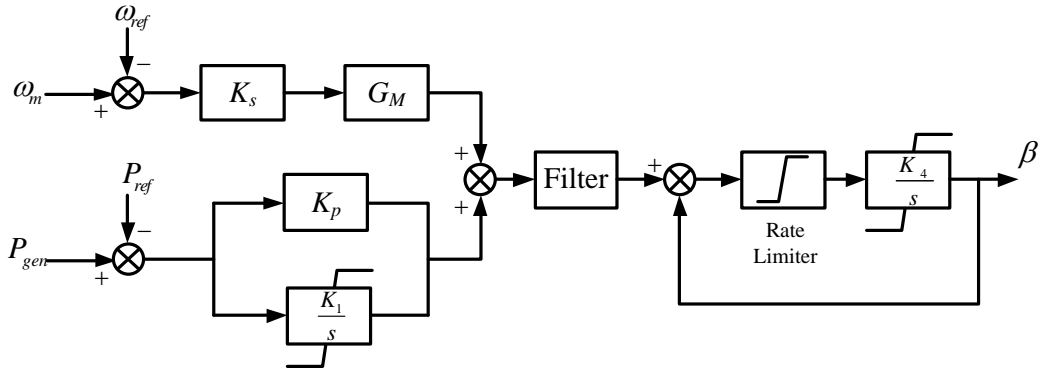


Figure 2.4: Control block of rotor pitch angle β .

2.3 Design of Electrical and Control Parameters

Base on the system circuit configuration and control blocks, parameters of electrical components and controllers can be developed by applying circuit

analysis and control theory.

2.3.1 DC Link

The DC link behaves as an intermedium between the grid-connected inverter and the machine-side converter. It is represented by the following differential equation:

$$C \frac{dV_{dc}}{dt} = S_a i_a + S_b i_b + S_c i_c - (S_{mA} i_{sA} + S_{mB} i_{sB} + S_{mC} i_{sC}) \quad (2.3)$$

In (2.3), i_a , i_b , and i_c are grid the line currents flowing into the converter. V_{dc} is the DC-link voltage. S_a , S_b , S_c and S_{mA} , S_{mB} , S_{mC} are the switching functions are the switching functions for the grid-connected inverter and machine-side converter, respectively.

2.3.1.1 DC-link Voltage V_{dc}

The DC-link of the wind turbine system provides an energy linkage between the two converters. The DC voltage is responsible for calculating other unknowns and has to be determined first. In order to have a lower THD in the grid currents, the amplitude-modulation index is chosen at the typical value $m_a = 0.8$. Then, V_{dc} can be obtained by the definition of the amplitude-modulation index given below:

$$V_{dc} = \frac{\sqrt{6} \cdot V_{ph}}{m_a} = \frac{\sqrt{6} \cdot 690 / \sqrt{3}}{0.8} = 1220V$$

2.3.1.2 Capacitor Size C

The capacitor size of the DC-link can be as large as possible to maintain a constant DC voltage. However, an unnecessarily enlarged capacitance will lead to a slower voltage response and excessive equipment volume required in the nacelle. Therefore, the actual capacitance is constrained by an upper bound and a lower bound. The lower bound capacitance is affected by the requirement of maximum DC voltage ripple. By considering the machine-side converter as a perfect resistive load, the capacitor dynamics in (2.3) can be re-written as [25]:

$$C_{\min} \frac{\Delta V_{dc}}{\Delta t} = S_a i_a + S_b i_b + S_c i_c - \frac{V_{dc}}{R_L} = i_{dc} - I_L \quad (2.4)$$

where ΔV_{dc} is the DC voltage ripple during a time period Δt , and S_a, S_b, S_c are the switching states of each phase realized by power electronic devices (VT in Figure 2.1). Because the instantaneous DC current i_{dc} acquires its largest value $i_{dc,max}$ from the switching state $S_a = S_b = S_c = 1$ and a minimum value of zero from $S_a = S_b = S_c = 0$, (2.4) can be split into two equations:

$$\begin{cases} C_{\min} \frac{\Delta V_{dc,up}}{T_{V,up}} = i_{dc,max} - I_{L,max} \\ C_{\min} \frac{\Delta V_{dc,down}}{T_{V,down}} = 0 - I_{L,max} \end{cases} \quad (2.5)$$

where $\Delta V_{dc,up}$ is the voltage rise during the capacitor charging time $T_{V,up}$, $\Delta V_{dc,down}$ is the voltage drop during the capacitor discharging time $T_{V,down}$, and $I_{L,max}$ is the maximum linear current equivalent of the DC-link. Taking

$\Delta V_{dc,ref} = \Delta V_{dc,up} = -\Delta V_{dc,down} = 24.4 \text{ V}$ (2%) and $T_{V,up} + T_{V,down} = T_s/2 = 1/(2 \cdot f_{cr})$, (2.5) becomes:

$$C_{\min} = \frac{i_L (i_{dc,\max} - i_L)}{2i_{dc,\max} f_{cr} \cdot \Delta V_{dc,ref}} = 1.2067 \times 10^4 \mu\text{F}$$

where $i_{dc,\max} = 7958.7 \text{ A}$, $i_L = 1837.6 \text{ A}$, and $f_{cr} = 2.4 \text{ kHz}$.

The upper bound capacitance is ruled by the dynamic requirement represented by voltage ascending time t_r that denotes the charging time for the DC capacitor to charge from its initial voltage to the desired 1220 V. The voltage response of the capacitor is given by:

$$V_{dc} - V_{d0} = (i_{dc,\max} R_{L,eq} - V_{d0}) \left(1 - e^{-\frac{t_r}{R_{L,eq} C_{\max}}} \right) \quad (2.6)$$

where V_{d0} is the initial DC voltage rectified by the six diodes (VD) from the three-phase grid with six IGBTs (VT) turned off. The value of V_{d0} is $V_{d0} = 1.3505 V_{l-l} = 931.8 \text{ V}$. $R_{L,eq}$ is the equivalent resistivity when the converter is working at its rated power, therefore its value is defined as: $R_{L,eq} = V_{dc}^2 / S_{rated} = 0.6639 \Omega$.

Setting $t_r = 0.005 \text{ s}$ in (2.6) and solving for C_{\max} :

$$C_{\max} = \frac{t_r}{R_{L,eq} \ln \left(\frac{i_{dc,\max} R_{L,eq} - V_{d0}}{i_{dc,\max} R_{L,eq} - V_{dc}} \right)} = 1.0992 \times 10^5 \mu\text{F}$$

The DC-link capacitance can be any value between C_{\max} and C_{\min} . Considering the margin, it is chosen barely larger than twice of C_{\min} as $C =$

24.98 mF.

2.3.2 Grid-Connected Inverter

Figure 2.5 illustrates the voltage oriented control (VOC) block diagram for the grid-connected inverter. The three controllers ($G_{V_{dc}}(s)$, $G_{i_d}(s)$ and $G_{i_q}(s)$) must acquire a favorable dynamic response without steady-state errors so PI controllers with limits can be adopted [26]. Parameters determined are DC-link voltage V_{dc} , DC capacitance C , AC inductance L_{ac} , and the limit settings for PI controllers ($G_{V_{dc}}(s)$, $G_{i_d}(s)$ and $G_{i_q}(s)$). In this section, the grid-connected inverter is designed to have the same power rating as the PMSM ($P_{rated} = 2$ MW, $S_{rated} = 2.2419$ MVA), therefore, it can mimic the power output properties of a synchronous machine in terms of adjusting active and reactive power independently within the rated apparent power. the model of the grid-connected converter is given as [27]:

$$\begin{cases} L_{ac} \frac{di_a}{dt} = -(S_a - \frac{S_a + S_b + S_c}{3}) \cdot V_{dc} + e_a \\ L_{ac} \frac{di_b}{dt} = -(S_b - \frac{S_a + S_b + S_c}{3}) \cdot V_{dc} + e_b \\ L_{ac} \frac{di_c}{dt} = -(S_c - \frac{S_a + S_b + S_c}{3}) \cdot V_{dc} + e_c \end{cases} \quad (2.7)$$

where e_a , e_b , and e_c are the grid line-to-neutral voltages.

2.3.2.1 Limits for PI Controllers $G_{V_{dc}}(s)$, $G_{i_d}(s)$ and $G_{i_q}(s)$

The limits of the PI controllers are important for regulating the maximum line current flowing between the converter and the grid. The limit of

The variable i_q is mostly ragged due to the switching, and thus a low pass filter can be implemented to smooth the waveform.

2.3.2.2 AC Inductance L_{ac}

Similar to the DC capacitance, the AC inductance is also limited by both an upper bound and a lower bound. Using phase A and an assumption of unity power factor, the inductor differential equation is introduced as follows:

$$L_{ac} \frac{di_a}{dt} = -\left(S_a - \frac{S_a + S_b + S_c}{3}\right) \cdot V_{dc} + e_a \quad (2.8)$$

The largest harmonic magnitude at switching frequency determines the minimum value of L_{ac} when the sinusoidal line current is at the peak point. Due to the unity power factor, e_a is also at its peak value: $e_a = V_m$. Switching states $S_a = S_b = S_c = 1$ and $S_a = S_b = S_c = 0$ renders a maximum current increasing rate to (2.8), while the state $S_a = 1, S_b = S_c = 0$ decrease the line current the most. Substituting $S_a = S_b = S_c = 0$ and $S_a = 1, S_b = S_c = 0$ into (2.8) respectively yields [25]:

$$\begin{cases} L_{ac,\min} \frac{\Delta i_{a,up}}{T_{i,up}} = V_m \\ L_{ac,\min} \frac{\Delta i_{a,down}}{T_{i,down}} = -\frac{2}{3}V_{dc} + V_m \end{cases} \quad (2.9)$$

where $\Delta i_{a,up}$ is the current increment during the switching time period $T_{i,up}$, and $\Delta i_{a,down}$ is the current drop during $T_{i,down}$. Setting $\Delta i_{ref} = \Delta i_{a,up} = -\Delta i_{a,down} = 300$ A and $T_{i,up} + T_{i,down} = T_s/2 = 1/(2 \cdot f_{cr})$, and substituting

in the known values: $V_{dc} = 1220$ V, $f_{cr} = 2400$ Hz, and $V_m = \sqrt{2/3} \times 690$ V into (2.9), the minimum inductance is:

$$L_{ac,\min} = \frac{V_m (2V_{dc} - 3V_m)}{4V_{dc}f_{cr} \cdot \Delta i_{ref}} = 0.1202 \text{ mH}$$

The maximum inductance is limited by two factors: the maximum apparent power flowing through the inductor and the AC current's rate of change. The maximum inductance limited by the power flow can be computed as:

$$L_{ac,\max 1} = 3V_{ph} \frac{V_{a,\max} - V_{ph}}{\omega S_{rated}} = 0.1409 \text{ mH}$$

Still, the chosen inductance has to be small enough to follow the changing rate of the AC current. According to (2.8), there is:

$$L_{ac,\max 2} \frac{di_a}{dt} = -(S_a - \frac{S_a + S_b + S_c}{3}) \cdot V_{dc} + e_a \quad (2.10)$$

The maximum current changing rate (di_a/dt) for phase A current $di_a/dt = I_{m,rated} \sin(\omega t + \phi)$ is ωI_m if I_m is constant, thus, the maximum di_a/dt occurs at the zero-crossing ($e_a = 0$) due to the unit power factor. The maximum controllable AC voltage on right-hand side of (2.10) can be achieved by setting $S_a = 0$ and $S_b = S_c = 1$. Substituting the aforementioned switching state into (2.10) yields $L_{ac,\max 2}$:

$$L_{ac,max2} = \frac{2V_{dc}}{3\omega I_{m,rated}} = 0.8132 \text{ mH} \quad (2.11)$$

Taking the smaller of $L_{ac,max1}$ and $L_{ac,max2}$, the maximum inductance for the grid-connected inverter is $L_{ac,max} = 0.1409$ mH. Considering $L_{ac,min}$ and $L_{ac,max}$, the AC inductance is chosen as $L_{ac} = 0.1296$ mH.

2.3.3 Machine-Side Converter

The machine-side converter is responsible for governing the electromagnetic torque and mechanical speed of the PMSM and has the same configuration as the grid-connected inverter, as shown Figure 2.1. The PMSM used here is a non-salient-pole machine with a low-rated frequency. The PMSM is modeled together with the converter as follows:

$$\begin{cases} (S_{mA} - \frac{S_{mA} + S_{mB} + S_{mC}}{3}) \cdot V_{dc} = R_s i_{sA} + \frac{d\lambda_{sA}}{dt} \\ (S_{mB} - \frac{S_{mA} + S_{mB} + S_{mC}}{3}) \cdot V_{dc} = R_s i_{sB} + \frac{d\lambda_{sB}}{dt} \\ (S_{mC} - \frac{S_{mA} + S_{mB} + S_{mC}}{3}) \cdot V_{dc} = R_s i_{sC} + \frac{d\lambda_{sC}}{dt} \end{cases} \quad (2.12)$$

where R_s is the stator winding resistance. λ_{sA} , λ_{sB} , and λ_{sC} are the total magnetic flux linkage of the stator. The machine-side converter control block is shown in Figure 2.6 [28].

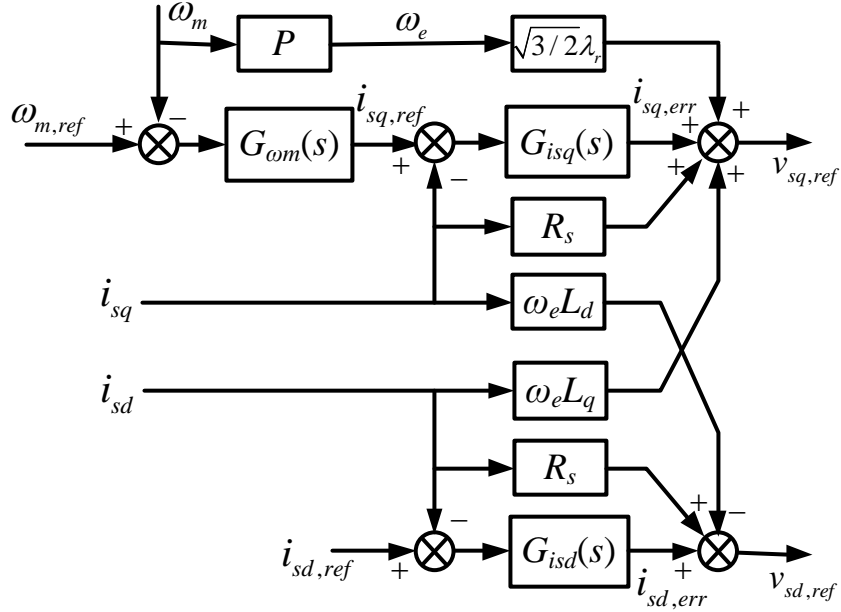


Figure 2.6: Control block diagram of the Machine-Side Converter

2.3.3.1 Limits for PI Controllers $G_{\omega_m}(s)$, $G_{i_{sd}}(s)$ and $G_{i_{sq}}(s)$

The PI controllers $G_{\omega_m}(s)$ and $G_{i_{sq}}(s)$ regulate the active current i_{sq} of the machine in series. These two controllers share the same limit in respect to the power equation of the PMSM:

$$i_{sq,rated} = \sqrt{\frac{2}{3}} \frac{P_{gen}}{P\lambda_r\omega_m} = 3249.1 \text{ A}$$

For the magnetizing current, i_{sd} is normally set to zero to acquire an optimal torque control. The limit of its controller $G_{i_{sd}}(s)$ is thus fixed and can be computed by the rated parameter of the machine, below:

$$i_{sd,rated} = \frac{\sqrt{S_{rated}^2 - P_{rated}^2}}{\sqrt{3}V_{l-l}} = 847.60 \text{ A}$$

2.3.3.2 Machine-Side Filter L_f

Due to the small inductance of the machine, the harmonic current will be large, causing torque pulsation. A filter, L_f , shown in Figure 2.1, is preferred in order to smooth the stator current. Calculation of inductance L_f is in the same fashion as that of L_{ac} . The minimum value of L_f is calculated as:

$$(L_s + L_{f,min}) = \frac{E_{sa}(2V_{dc} - 3E_{sa})}{4V_{dc}f_{cr} \cdot \Delta i_{s,ref}} = 0.4168 \text{ mH}$$

where L_s is the per-phase stator inductance in abc frame. For $i_{sd} = 0$, i_{sq} is equal to i_s and L_s is equal to L_q . E_{sa} is the internal phase voltage of the PMSM, given as 0.8921 p.u. of the rated phase voltage. $\Delta i_{s,ref}$ is the desired current harmonic at switching frequency and is set to 100 A. Since $L_s = 1.5731 \text{ mH} > 0.4168 \text{ mH}$, the minimum value of L_f is $L_{f,min} = 0$.

$L_{f,max}$ can be derived similarly as $L_{ac,max}$. Regarding a rated active power, power flow from the machine to the converter is written as:

$$P_{rated} = 3E_{sa} \frac{E_{sa}}{\omega_m (L_s + L_{f,max1})} \quad (2.13)$$

From (2.4), $L_{f,max1}$ can be determined as:

$$L_{f,max1} = 3E_{sa} \frac{E_{sa}}{\omega_m P_{rated}} - L_s = 1.5194 \text{ mH}$$

Similar to the calculation procedure of $L_{ac,max2}$, using (2.11) and subtract the value of L_s from its right-hand side, $L_{f,max2}$ is:

$$L_{f,max2} = \frac{2V_{dc}}{3\omega_m I_{m,rated}} - L_s = 3.4314 \text{ mH}$$

Finally the maximum bound of L_f is $L_{f,max} = 1.5194 \text{ mH}$. Based on the large dispersion of $L_{f,min}$ and $L_{f,max}$, L_f can be chosen within a wide range of values. In order to minimize the inductor size, L_f is set to just over one-third of the maximum value, which is $L_f = 0.52 \text{ mH}$.

2.4 Design Verificaiton and Simulation

The complete model of the Type 4 wind turbine is developed in PSCADTM using a $1 \mu\text{s}$ solution time step. The parameters of power circuits and controllers are set to values derived from previous sections. Steady-state operations are simulated from cut-in wind speed up to the cut-out point. Power curve and rotor performance under various wind speed are shown in Figure 2.7(a). Above 13 m/s, the rotor pitch control maintains the constant rated power output and prevents from overloading. The rotor performance C_p has its highest value at a lower wind speed and begins to drop when the wind speed is larger than 8 m/s. Keeping the highest value of C_p at a lower wind speed is achieved by varying the rotor speed to acquire the optimal tip speed

ratio, as expressed in Figure 2.7(b). The rotor speed will reach its rated value at a wind speed of 8 m/s and will maintain the rated value until the cut-out wind speed. Figure 2.7(b) also shows the pitch angle, which has its largest value at a wind speed of 19 m/s and starts to decrease due to the stall of the rotor blades.

DC-link voltage under steady-state is displayed in Figure 2.8(a). The DC voltage is bouncing around the designed 1220 V and the ripple is within the requirement $\Delta V_{dc,ref}$. Figure 2.8(b) illustrates the grid current and phase-to-ground voltage of phase A under the rated wind speed. The grid voltage and current are in per-unit on a base of the PMSM. Since the current flowing into the wind turbine system is defined as positive, it is out of phase with the grid voltage when the power factor is unity.

The designed values and simulation results are listed and compared in Table 2.1. The simulation results meet the designed value well, however, the maximum harmonic current at switching frequency in both the grid side and the PMSM exceeds the designed value. This inconsistency is caused by PWM dead zones and the previous assumptions of a constant DC voltage and an ideal switching process for power electronic devices.

2.5 Summary

This section has described the design of parameters for a 2-MW Type 4 direct-drive wind turbine. The wind turbine has been considered as a full model including aerodynamics, PMSM, machine-side converter and grid-

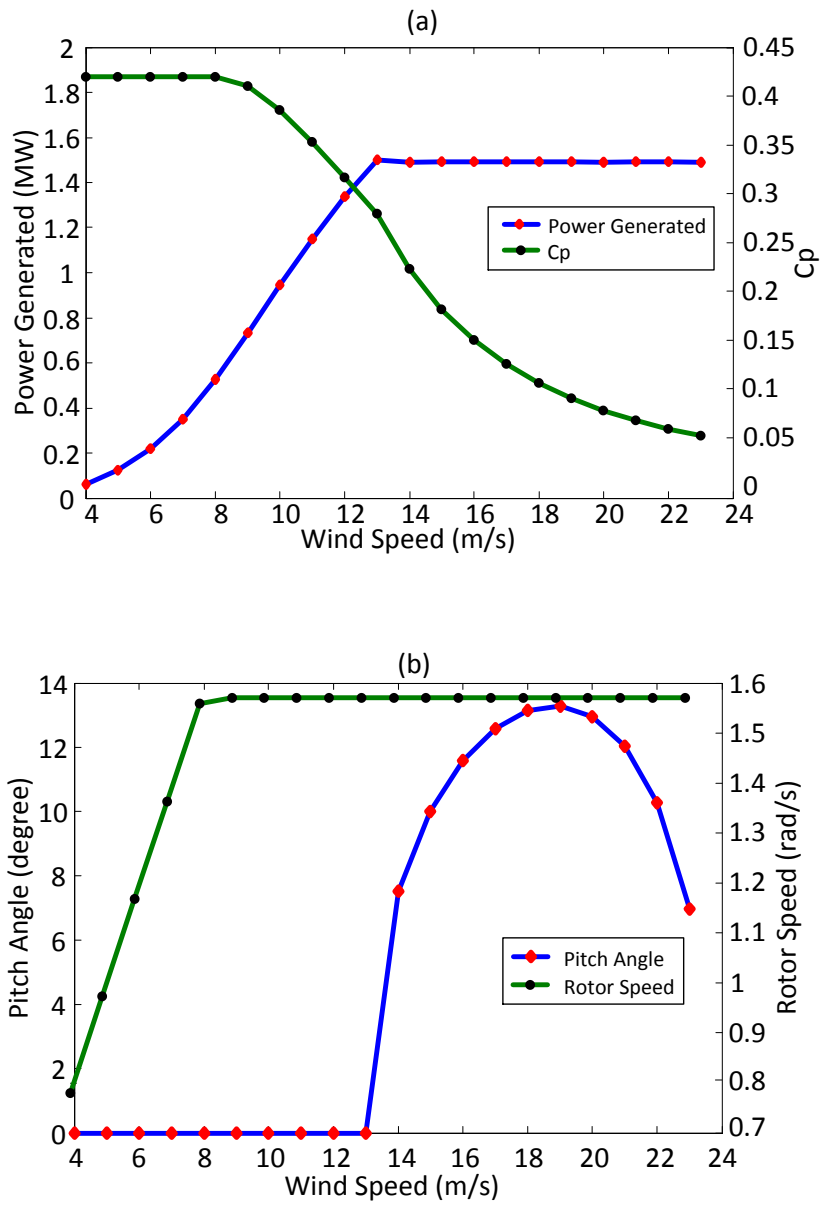


Figure 2.7: Steady-state performance of the designed wind turbine. (a) Power curve and blade performance versus the wind speed; (b) Pitch angle and rotor speed versus wind speed.

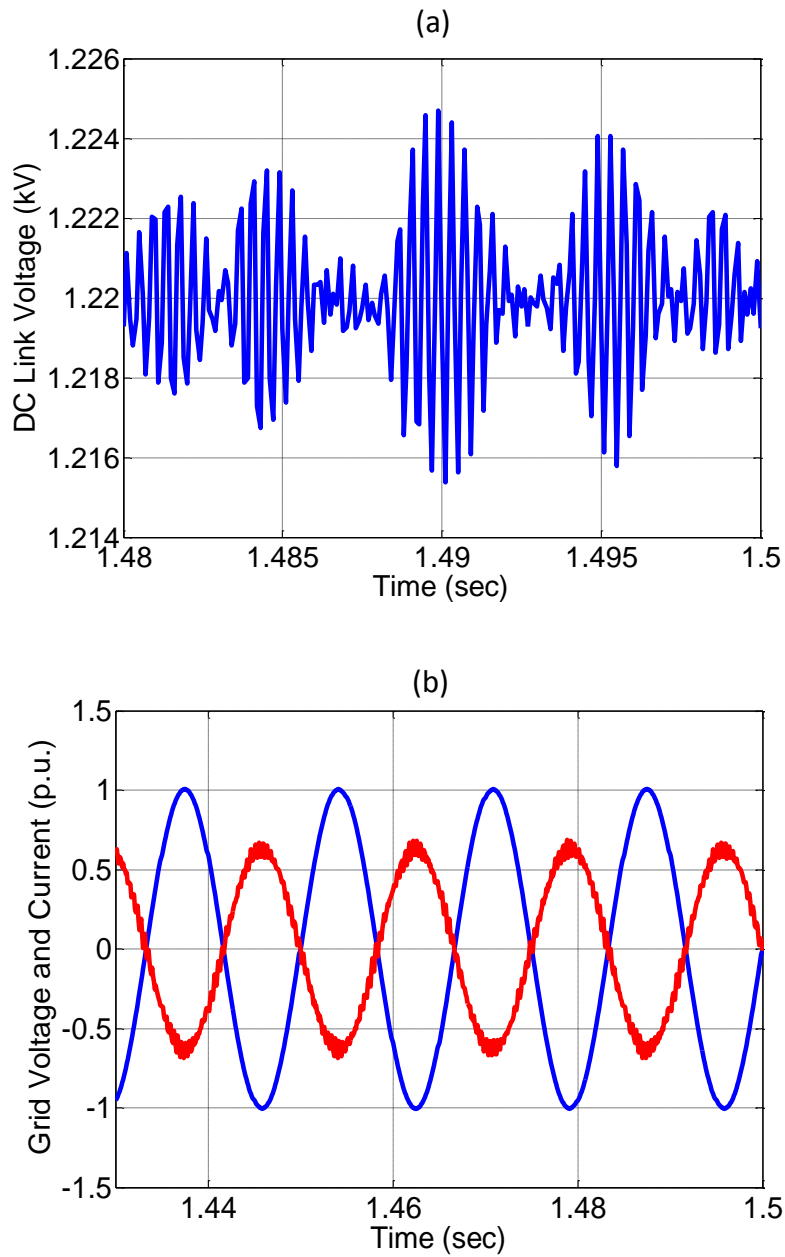


Figure 2.8: Voltages and currents under rated wind speed operation. (a) DC-link voltage; (b) Grid voltage and current of phase A

Table 2.1: Design Requirements and Systems Actual Response

Items	Designed Values	Simulation Results
Active power generated (P_{gen})	1.5 MW	1.4994 MW
Rated angular speed (ω_m)	15 rpm	15.0005 rpm
DC-link voltage (V_{dc})	1220 V	1220.4 V
Maximum DC voltage ripple ($\Delta V_{dc,ref}$)	24.4 V (2%)	9.959 V (0.8%)
Voltage ascending time (t_r)	0.005 s	0.0009 s
Maximum grid current harmonic magnitude(Δi_{ref})	300 A	377.85 A
Maximum machine current harmonic magnitude($\Delta i_{s,ref}$)	100 A	119.38 A

connected inverter. The control variables and parameters for each part have been elaborately derived and computed according to the proposed requirements. In order to test the designed variables, the simulation model of the wind turbine has been built using PSCATM. Data from the simulation demonstrate that the system has featured a promising performance on both steady-state operation and dynamic response. By comparing the requirements and the simulated quantities, the designed parameters have been proven to be valid and practical.

Chapter 3

Model Reduction, Validation and Analysis of Direct-Drive Wind Turbine

To gather long-term wind power data and implement controls, it requires accurate steady-state and dynamic models of wind farms. Due to modeling complexity and computational burden, wind farms are rarely represented with equivalent models of individual wind turbines. Instead, they are represented with equivalent models of multiple turbines of the same type, known as aggregated modeling. Depending on the need of the studies, equivalent models can be full or reduced order. Reduced order models for wind turbines with doubly-fed induction generator technology (Type 3) are relatively well-established and have been proven viable [29–31]. The objective of this section is to propose reduced order models of the aforementioned Type 4 wind turbine and to fill the gap between the fully dynamic model and the steady-state model, providing the possibility of simulating a wind turbine through long-term (monthly or annual) operations under an acceptable CPU runtime while maintaining the response for major dynamic events such as voltage sags, power systems faults, and controlling and regulating operations.

There are three stages of reduction. In the first stage, three-phase volt-

ages and currents of the converters are transformed into DC quantities via the power-invariant $d-q$ transformation, ignoring the converter zero-sequence network. Ideal voltage and current sources driven by reference switching functions from the control systems are implemented as switching sources to form new power circuits in the $d-q$ domain. Hence, the switching characteristics and losses of all power electronic devices can be reduced while controllers and general system dynamics remain intact. Based on the circuits from the first stage, the second stage reduction averages the discrete switching functions with an assumption of infinite switching frequency for power electronic devices. Current harmonics and DC ripples caused by the switching process and over-modulation sub-transient during wind turbine dynamic operations are not included. To further eliminate the power circuit, the third stage reduction is derived by considering a steady-state operation for grid active and PMSM torque currents, and by assuming a perfect regulation of the grid reactive and PMSM magnetizing currents. However, system dynamics in terms of current, voltage, and torque responses during wind speed change and fault conditions are reserved. Simpler controllers for the reduced system are designed without current feedback, yet are capable of maintaining an overall controllability of the wind turbine.

3.1 Possibility of Modeling Reduction Regarding Desired Time Scale

Valid wind turbine modeling includes developing mathematical expressions that behave as actual wind turbines electrically and mechanically during both transient and long-term operation. Although there are various aerodynamic and electrical parameters in a wind turbine system, only a handful of key elements dominate the major response.

3.1.1 Long-Term Operations

The main interest of wind turbines during a normal (without power system events, such as a fault), long-term operation is the active power output while the three-phase terminal voltages and line currents may not need to be observed. Typically, long-term data is recorded by the power monitoring equipment with a sampling resolution in terms of minutes or hours, which is much longer than even the slowest electrical dynamics. Scarce sampled data is insufficient to interpret any dynamical information. For instance, a 10-minute sampling rate can only record the r.m.s. value of three-phase quantities, instead of any 60 Hz information. Therefore, most of the long-term operations can be realized as a pointwise steady-state picture.

To be specific, the power curve of a wind turbine for any type is a major demonstration of steady-state characteristics. Using the wind turbine power curve and the wind speed can produce a relatively credible long-term power output and this kind of modeling can be considered a ‘pure’ steady-

state model. Intrinsic parameters related to the wind turbine power curve are blade aerodynamic performance C_p and total system losses P_{loss} . The system losses P_{loss} will not be included, because it varies under different production levels, and is a minor contribution to the system resistive components. With a proper linearization during the modeling process, the wind turbine can be nominalized to any rated power arbitrarily using aggregation.

3.1.2 Transient Responses

Differing from long-term operation, transient responses are dominated by the system differential equations. Elaborated electrical parameters specify the dynamics in detail. Therefore, the four types of wind turbine will never experience the same transient electrically. The Type 1 and 2 wind turbines reflect dynamics from electromagnetic circuits of an induction machine, while the Type 3 wind turbine features a combined response of the machine stator and the power electronic switching in the rotor circuit. The Type 4 wind turbine is fully controlled by power electronic circuits and their respective controllers; the accuracy of its transient response is primarily determined by the controller design and settings, ignoring the electromagnetic phenomenon from the machine.

The boundary between dynamics and steady-state related to the time scale is shown in Figure 8. As the sampling interval increases, the dynamical information decreases, according to the Nyquist-Shannon sampling theorem. Because a detailed model could only represent its steady-state features if a

larger sampling interval is applied, the modeling complexity can be just enough to cover the fastest dynamics in Figure 3.1. The reduced model proposed in this section is designed to keep the steady-state operation up to 10 minutes, yet can still cover the dynamics down to 1 ms, including all three-phase quantities and their corresponding r.m.s values.

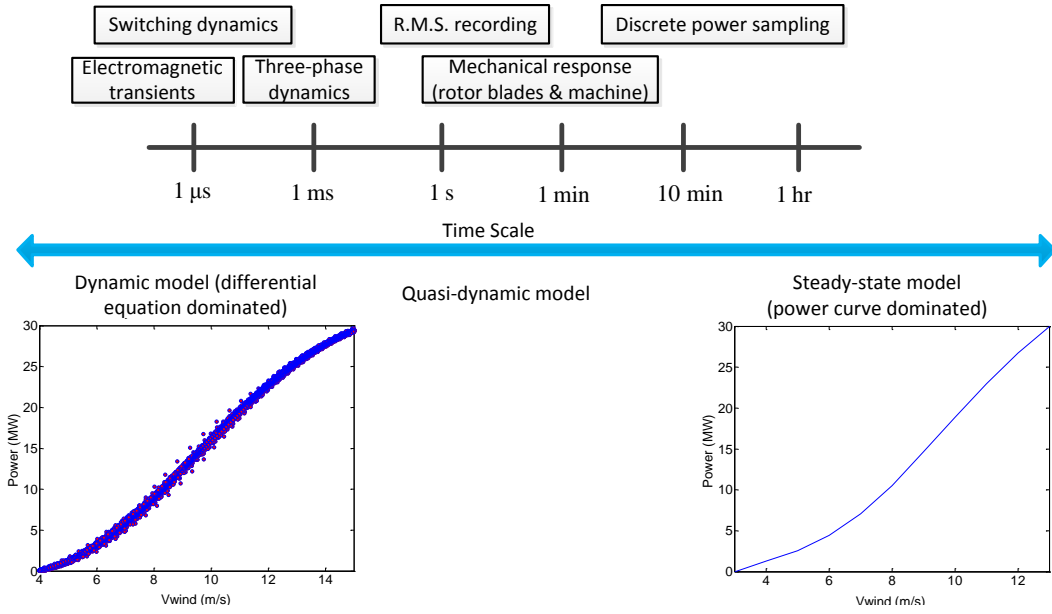


Figure 3.1: Time-scale boundaries between dynamics and steady-state operations in a wind turbine system.

3.2 Switching-Function and Switching-Average Models

To increase the computational efficiency, the complexity of the wind turbine system can be reduced based on analysis and approach for power electronic circuits.

3.2.1 Switching-Function Model

By performing the power-invariant d - q transformation to the power circuit in Figure 2.1, the three-phase converter model can be transformed into a two-phase equivalent. Thus, voltages and currents in the three-phase AC circuit will be replaced by DC quantities. The derivation of the system model can be found in [15] by pre-multiplying the transformation matrix (3.1) to all three-phase quantities in the full model (2.3), (2.7) and (2.12) using matrix multiplication rules. Further, the flux linkage is converted by $\lambda_{sd} = L_d i_{sd} + \sqrt{3/2} \lambda_r$ and $\lambda_{sq} = L_q i_{sq}$.

$$C_{3S/2R} = \sqrt{\frac{2}{3}} \begin{bmatrix} \cos \theta & \cos(\theta - 2\pi/3) & \cos(\theta - 4\pi/3) \\ \sin \theta & \sin(\theta - 2\pi/3) & \sin(\theta - 4\pi/3) \end{bmatrix} \quad (3.1)$$

Power electronic circuits in the full model are replaced by ideal voltage and current sources. These ideal sources are driven by reference voltages and currents weighted by S_d , S_q , S_{sd} , and S_{sq} , shown in Figure 3.2. The corresponding differential equations are as follows:

$$\begin{cases} L_{ac} \frac{di_d}{dt} + \omega L_{ac} i_q = -S_d V_{dc} + e_d \\ L_{ac} \frac{di_q}{dt} - \omega L_{ac} i_d = -S_q V_{dc} + e_q \end{cases} \quad (3.2)$$

$$\begin{cases} S_{md} V_{dc} = R_s i_{sd} + L_{sd} \frac{di_{sd}}{dt} - \omega_e L_{sq} i_{sq} \\ S_{mq} V_{dc} = R_s i_{sq} + L_{sq} \frac{di_{sq}}{dt} + \omega_e L_{sd} i_{sd} + \sqrt{\frac{3}{2}} \omega_e \lambda_r \end{cases} \quad (3.3)$$

$$C \frac{dV_{dc}}{dt} = S_d i_d + S_q i_q - (S_{md} i_{sd} + S_{mq} i_{sq}) \quad (3.4)$$

This approach ignores switching characteristics and losses of the power electronic devices. In Figure 3.2, $\omega_e = P \cdot \omega_m$ is the electrical angular speed of the PMSM in radians. Seen by the grid, the grid-side active current i_q and reactive currents i_d are obtained from their respective circuits and transformed into the abc frame of reference as three-phase quantities i_a , i_b , and i_c , which appeared in the full model. Then, the three-phase currents i_a , i_b , and i_c are injected in to the grid using ideal current sources. The control systems remain the same as the full model illustrated in [32–35], keeping a mostly intact dynamic. The current harmonic components and machine torque fluctuation caused by the switching are the same as those in the full model.

3.2.2 Switching-Average Model

Although the wind turbine system has already been modeled with differential equations, it is still a discrete system, as the components in Figure 3.2 are represented by switching functions. The fast-average approach can be further applied to reduce the switching terms.

Assuming an infinite switching frequency, the switching functions in Figure 3.2 can be averaged by continuous signals, instead of discrete signals, as follows:

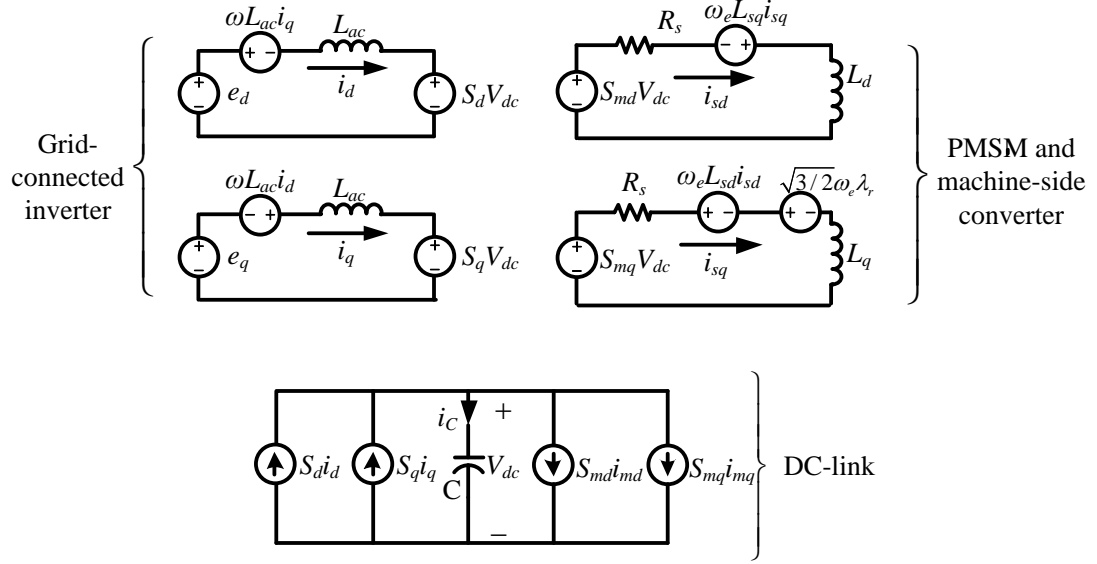


Figure 3.2: Reduced power circuit of the switching-function model. This topology is then used to derive the switching-average model and quasi-dynamic model.

$$\langle S_d \rangle = \frac{\langle v_d \rangle}{V_{dc}}, \langle S_q \rangle = \frac{\langle v_q \rangle}{V_{dc}}, \langle S_{md} \rangle = \frac{\langle v_{md} \rangle}{V_{dc}}, \langle S_{sq} \rangle = \frac{\langle v_{sq} \rangle}{V_{dc}} \quad (3.5)$$

Thus, the averaged system differential equations can be derived by substituting (3.5) into (3.2), (3.3) and (3.4):

$$\begin{cases} L_{ac} \frac{di_d}{dt} + \omega L_{ac} i_q = -\langle v_d \rangle + e_d \\ L_{ac} \frac{di_q}{dt} - \omega L_{ac} i_d = -\langle v_q \rangle + e_q \end{cases} \quad (3.6)$$

$$\begin{cases} \langle v_{sd} \rangle = R_s i_{sd} + L_{sd} \frac{di_{sd}}{dt} - \omega_e L_{sq} i_{sq} \\ \langle v_{sq} \rangle = R_s i_{sq} + L_{sq} \frac{di_{sq}}{dt} + \omega_e L_{sd} i_{sd} + \sqrt{\frac{3}{2}} \omega_e \lambda_r \end{cases} \quad (3.7)$$

$$C \frac{dV_{dc}}{dt} = \left(\frac{\langle v_d \rangle}{V_{dc}} i_d + \frac{\langle v_q \rangle}{V_{dc}} i_q \right) - \left(\frac{\langle v_{sd} \rangle}{V_{dc}} i_{sd} + \frac{\langle v_{sq} \rangle}{V_{dc}} i_{sq} \right) \quad (3.8)$$

where $\langle v_d \rangle$ and $\langle v_q \rangle$, $\langle v_{sd} \rangle$, and $\langle v_{sq} \rangle$ are the averaged voltages of the grid-connected and machine-side converters in the d - q frame, respectively. These voltages can be the output signals from the controllers for the modulation delay has been removed. The current response in the circuits can be used to calculate the grid power injection and the PMSM torque.

Because the simulation software does not have to solve the switching functions, which require much smaller solution intervals depending on the switching frequency, the requirement for the solution time step of a switching-average model will be more flexible. This advantage leads to an even shorter CPU runtime by setting a larger solution time step without compromising accuracy.

3.3 Quasi-Dynamic Model

The switching-function and switching-average models are derived from fundamental power electronic analysis. They are capable of representing electromagnetic transient of the wind turbine. They can, however, be further simplified by assuming a steady-state operation for current variables, and most of the differential equations can be reduced by setting the dynamic terms to zero. During the reduction, certain dynamics, such as current, voltage, and torque response, must be retained and cannot be reduced. Therefore, the third stage

reduced model is quasi-dynamic.

Identifications must be made in the first priority to discriminate essential parts of the wind turbine modeling. The dynamic response of an energy system is represented by its transient, during which the energy stored in different components interact with each other. For a Type 4 wind turbine system, there are three main types of energy: kinetic stored on the rotor blades, electric field energy in the DC capacitor, and the AC electromotive force from the grid. Since the AC electromotive force from the grid is not a component in the wind turbine system, but is a known input quantity, the differential equations for the DC capacitor and mass model of the rotor blades should be reserved and all controllers can be ignored, except for the DC voltage and rotor speed controllers.

Based on the analysis above, the dynamics of the grid active current i_q and PMSM torque current i_{sq} in the wind turbine system will be taken into account, as the energy flowing between multiple systems is responsible only for the delivery of active power. Thus, the following assumptions are made during the development:

- The total energy stored in the DC capacitor and the rotor blades is much larger than that stored in the system inductance (L_d , L_q and L_{ac}) for any time;
- The grid reactive current i_d and the PMSM magnetizing current i_{sd} are assumed to be in a steady-state and will follow the controller well without

any delay or disturbance;

- The DC-link is the linkage for the grid active current i_q and the PMSM torque current i_{sq} , ignoring the voltage fluctuation caused by the grid reactive current i_d and the machine magnetizing current i_{sd} .

3.3.1 Model Derivation

Developed based on the switching-average model, the wind turbine is also considered as current source injections in the abc frame. System unknown variables are the grid active and reactive currents (i_q and i_d in (3.6)). Starting with the grid-connected converter, i_d is a reference given manually, according to the premade assumptions, while i_q can be derived by linearizing and averaging the switching process. Assuming a steady-state active power flow and ignoring the reactive current, (3.6) can be rewritten with $di_q/dt = 0$ as:

$$\begin{cases} \langle v_d \rangle = S_d V_{dc} = e_d - \omega L_{ac} i_q \\ \langle v_q \rangle = S_q V_{dc} = e_q \end{cases} \quad (3.9)$$

In the same way, the averaged PMSM model in (3.7) can be simplified by setting $i_{sd} = 0$ and $di_{sq}/dt = 0$:

$$\begin{cases} \langle v_{sd} \rangle = S_{md} V_{dc} = -P\omega_m L_{sq} i_{sq} \\ \langle v_{sq} \rangle = S_{mq} V_{dc} = R_s i_{sq} + \sqrt{\frac{3}{2}} P\omega_m \lambda_r \end{cases} \quad (3.10)$$

Substituting (3.9) and (3.10) into (3.8) gives:

$$C \frac{dV_{dc}}{dt} = \frac{e_q}{V_{dc}} i_q - \frac{R_s i_{sq}^2}{V_{dc}} - \sqrt{\frac{3}{2}} \frac{P \omega_m \lambda_r}{V_{dc}} i_{sq} \quad (3.11)$$

The torque current i_{sq} in (3.11) is still an unknown and can thus be eliminated by considering the electromagnetic torque equation of the PMSM $T_e = \sqrt{3/2} P \lambda_r i_{sq}$ (P is pole pairs):

$$C \frac{dV_{dc}}{dt} = \frac{e_q}{V_{dc}} i_q - \frac{2R_s T_e^2}{3V_{dc} P^2 \lambda_r^2} - \frac{\omega_m T_e}{V_{dc}} \quad (3.12)$$

Noted that the first equations in both (3.9) and (3.10) are not necessary for the modeling due to the fact that $\langle v_d \rangle$ and $\langle v_{sd} \rangle$ are no longer regulated by the controllers and can be discarded. As mentioned above, the kinetic energy stored in the rotor blades must be considered, so the rotor mass model must remain. Finally, the quasi-dynamic model of the direct-drive wind turbine is as follows:

$$C \frac{dV_{dc}}{dt} = \frac{e_q}{V_{dc}} i_q - \frac{2R_s T_e^2}{3V_{dc} P^2 \lambda_r^2} - \frac{\omega_m T_e}{V_{dc}} \quad (3.13a)$$

$$J \frac{d\omega_m}{dt} = T_e + T_m - B\omega_m \quad (3.13b)$$

The aerodynamics of the rotor blades are formed by linear equations, according to (2.1) and (2.2), and do not require any reduction, yet, the controllers for the wind turbine electrical system must be simplified and modified to fit the derived model. System parameters such as C , J , B , and V_{dc} in (3.13)

are responsible for the transient response instead of the long-term operations. C and V_{dc} have been calculated, while J and B are innate parameters designated to the system in per-unit. They are given the values of $J = 5.0$ p.u. and $B = 0$.

3.3.2 Reduced Controllers

From (3.13a) and (3.13b), feedback-controlled variables can be identified as the DC-link voltage V_{dc} and the rotor speed ω_m . The simplified controller shown in Figure 3.3 is reduced from the full system controller, where $G_{V_{dc}}(s)$ is responsible for balancing V_{dc} in (3.13a).

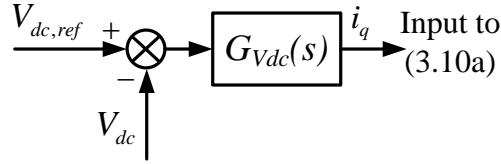


Figure 3.3: Reduced controller for the DC-link voltage. It controls the active power following from the grid to the wind turbine system ignoring the reactive component.

Similarly, the torque current i_{sq} can be generated from the rotor speed controller $G_{\omega_m}(s)$ in Figure 3.4. With a known i_{sq} , the input T_e for the mass model in (3.13b) can be calculated through the torque equation of a non-salient pole PMSM. Thus, both the DC-link voltage and the rotor speed are controlled by their respective closed loops, representing primary dynamics of a Type 4 wind turbine.

Finally, the block diagram of the quasi-dynamic Type 4 wind turbine

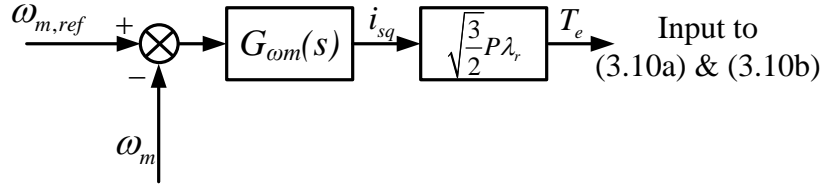


Figure 3.4: Reduced controller for the PMSM. The active current flowing into the machine is converted into electromagnetic torque using the torque equation and energizes the rotor-blades mass model.

model, along with the control systems, is shown in Figure 3.5. The proposed quasi-dynamic model possesses an averaged feature that does not perform the switching. Nevertheless, this approach is much simpler than the full model, as well as other methods in [32–35], as fewer system differential equations and simpler controllers are involved. Due to the ignored switching process, the simulation software is unnecessary to perform the switching that requires a more condensed solution time step in respect to the switching frequency; thus, the model can run under a much larger solution time step without losing accuracy. The sub-transient response will not be represented due to the absence of system inductance. This absence is acceptable, as the ignored inductance of the PMSM and the grid-side inline inductance is small, storing a fast-dissipated energy comparing to that in the capacitor and on the rotor blades, and has limited effects during a transient event. The reactive power of the wind turbine system is idealized and controlled directly at the d - q -to- abc frame transformation without feedback.

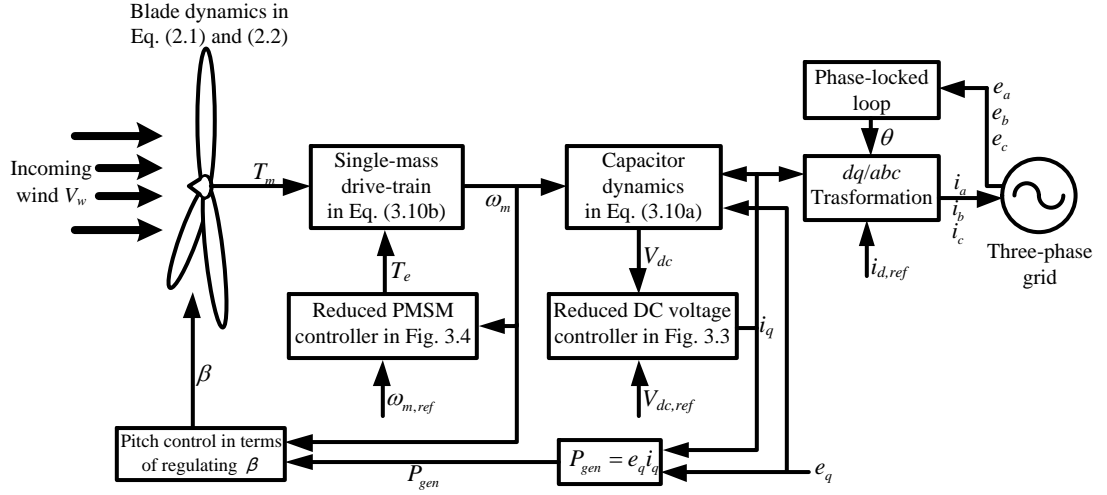


Figure 3.5: Block diagram of the quasi-dynamic Type 4 wind turbine model. With reduced electrical system and non-reduced aerodynamics, it is capable for capturing an accurate steady-state information and major dynamics as well as control events.

3.4 Validation of the Model Reductions

3.4.1 Case 1: Steady-State Operation

During steady-state operation, the reduced models must provide generally the same results as those from the full model. For the switching-function model, the DC voltage ripple and the line current harmonics at switching frequency must be comparable with the full model. The switching-average and quasi-dynamic models must give accurate averaged results with an acceptable error. For the steady-state operation, the wind speed is set to $V_w = 13$ m/s.

Figure 3.6 displays the steady-state DC-link voltage, the grid line current of phase A, and the power output, respectively. The capability of replicating DC voltage ripples and AC current harmonics is shown accurately by the

switching-function model. The switching-average model and quasi-dynamic model work as expected with negligible error. Active power flow is measured by a power meter with a smoothing time constant of 1 ms. Steady-state waveforms are displayed in Figure 3.6(c). Switching losses of non-ideal power electronic devices leads to a slightly lower power output from the full model than those of the reduced models. Power oscillations caused by the switching from the full model and the switching-function model, however, match well with each other, while the switching-average model and the quasi-dynamic model hold a constant power output.

3.4.2 Case 2: Response during a Symmetrical Fault

In this case, a 50% three-phase voltage sag is employed to simulate the wind turbine behavior during a symmetrical fault. The fault occurs at 0.5 s and lasts for 3 cycles. There is no crowbar connected to the DC-link and the wind turbine is working at the rated power output under the constant rated wind speed. The DC-link voltage, the grid line current of phase A, and the power generated are plotted in Figure 3.7(a), (b) and (c), respectively.

Due to the voltage sag and the controller limit settings of the grid-connected converter, the power pumped into the grid decreases, while the power extracted by the rotor blades remains unchanged, resulting in an over-voltage problem on the DC-link, as shown in Figure 3.7. Because of the absence of the crowbar, the surplus energy acquired during the fault must be fed into the grid, even after the fault has been cleared. Therefore, the

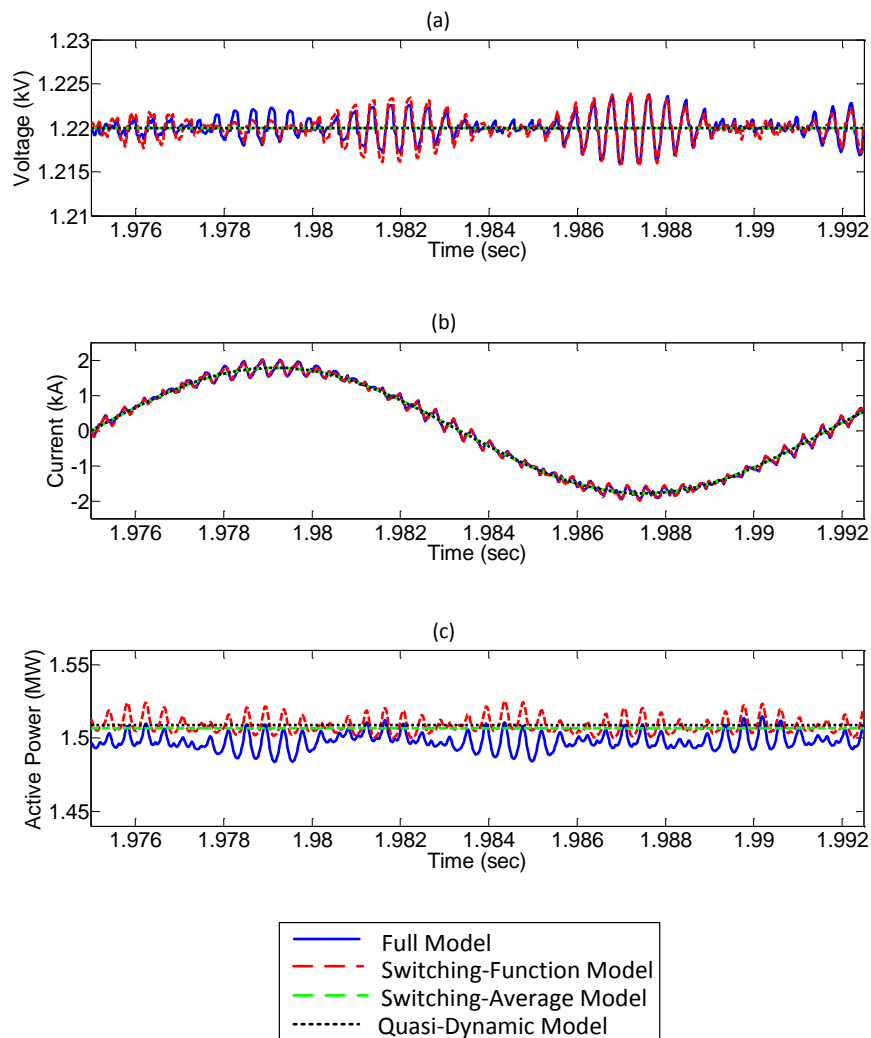


Figure 3.6: Steady-state operation. (a) DC-link voltage. Ripples can be represented by the full and switching-function models but not by the switching-average and quasi-dynamic models; (b) Grid line current of phase A. Current harmonics at switching frequency can be found in full and switching-function models and is the root cause for the DC ripples and power oscillation; (c) Active power generated. The power is recorded by a power meter with a smoothing constant to approach the real-world situation.

line current in Figure 3.7(b) suffers a swell for 5.5 cycles rather than 3 cycles. This phenomenon explains the power variations in Figure 3.7(c). From the comparison, the three reduced models are still valid and can render practical results for a fault analysis.

Features and performances of the reduced models are summarized in Table 3.1. The runtime data is collected with a PC configuration as follows: Intel Core i7-3630QM CPU @ 2.40 GHz, 8.00 GB RAM and 64-bit Windows 7 operating system. The simulation duration is 1 s with a 100 μ s plotting interval based on the steady-state operation in Case 1. The computational efficiency can be noted that for a 1 μ s solution step, the proposed quasi-dynamic model is almost three times faster than the full mode. Availability and adaptability of using a much larger time step is even more desirable compared to other models. At a 100 μ s solution step, it takes only 0.41 s to complete the 1-second simulation, which is faster than the real-time solution, while the full model and switching-function model become extremely inaccurate and not practical for yielding usable information.

Table 3.1: Lifetime Depreciation Assessment of the Fast-Response ESS

Model type	System dynamics	Solution step requirement	CPU runtime	
			1 μ s step	100 μ s step
Full model	Switching	Frequency restrained	26.28 s	Not accurate
Switching-fuction			19.40 s	Not accurate
Switching-average	Averaged	Flexible	17.55 s	0.61 s
Quasi-dynamic			9.98 s	0.41 s

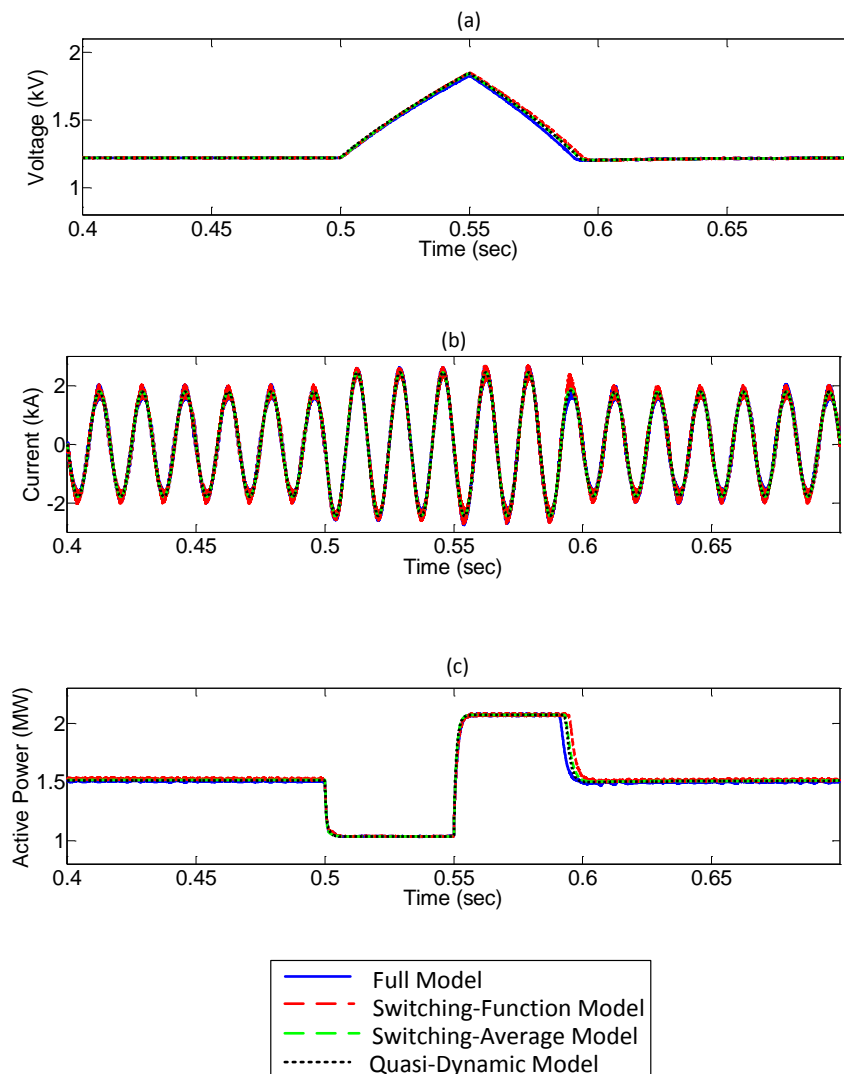


Figure 3.7: Response in a symmetrical fault. (a) DC-link voltage. The over-voltage is due to the power difference between the input (power captured by the rotor blades) and the output (power fed into the grid); (b) Grid line current of phase A. The current swell is caused by ‘pumping’ the excessive power into the grid during and after the fault; (c) Active power generated. This power profile is a typical response of the modeled Type 4 wind turbine, however, it can be modified by different control strategies.

3.4.3 Case 3: Model Validation Using Data from NREL

Although valid and efficient, the reduced models must be validated using real-world wind data. Validating wind turbine models using field data has been performed for in many studies. Modeling and validating Type 1 fixed speed wind turbine have been conducted in [36]. The Type 3 doubly-fed induction generator (DFIG) is currently the prevalent type in the industry. Different models of DFIG have been proven to be valid and applicable under normal operations [37], unbalanced voltage sags [38], and short-circuit faults [29]. In [39], comprehensive analyses and validations for the existing four types of wind turbines are discussed, however, the detailed modeling process regarding mathematical derivations is not rendered. In this test case, long-term real-world wind speed data is only applied to the quasi-dynamic model for validation purposes.

To accomplish the validation, wind resource data measured by NREL at over 30,000 sites in the Western U.S. can be found and is accessible online [1]. Field wind speed datasets of a three-year span (from 2004 to 2006) correspond with power output pre-validated by National Renewable Energy Laboratory (NREL). The field wind speed data for the validation is chosen from site ID 12 located in the West Texas with coordinates of 31.28°N, 104.52°W. The quasi-dynamic model is run for the entire year of 2004 in PSCADTM. This wind speed dataset has a minimum value of 0.18 m/s and maximum value of 26.06 m/s, which can cover the normal operating conditions. Mean and variance of the wind speed over 2004 are 7.85 m/s and 14.36 m/s, respectively.

The best field data resolution available from NREL is of every 10-minute interval, which must be interpolated down to the solution time step. Although PSCADTM automatically employs a linear interpolation algorithm for the external data source; this linear interpolant will introduce a problem: it lacks smoothness and has corners. Once applied, the wind turbine will be actuated by this discontinuous data with sudden changes at the corners, creating unexpected disturbances that may be recorded by the power measuring meter. Because the corners will appear every 10 minutes according to the original data density, the impact of this disturbance will be represented regularly in the simulated power dataset. To seek a better solution, higher degree piecewise polynomials can be applied, filling the existing sampled data with points that create a smoother wind speed profile and remove the sharpness caused by the linear interpolant [40]. A piecewise cubic Hermite interpolant with continuous derivatives has been implemented for this purpose. Since the third derivative of a cubic is a constant, it is possible to show that any piecewise cubic with three continuous derivatives at every data point must be exactly the same cubic [41, 42]. The plotting interval is set to 1 minute, thus the interpolation does not need to recreate the points between plotting samples. Preprocessed in Matlab, the 10-minute sampled data is interpolated down to a 1-minute resolution for the simulation in PSCADTM.

The simulation settings in PSCADTM are the same as the previous case: a 1.5-ms solution step with a 1-minute plotting interval. Real power from NREL database and simulations are plotted together for the month of

January in Figure 3.8. The two curves match each other well, representing a valid quasi-dynamic wind turbine model. The error percentage for the mean and the variance over entire 2004 is 4.18% and 0.404%, respectively.

As claimed before, the proposed quasi-dynamic model should acquire a capability of partial aggregation for wind farm simulations. For this purpose, three quasi-dynamic wind turbines representing a small wind farm are developed similarly. Their 690 V outputs are connected to an infinite source to achieve the same configuration as that of NREL. Power generated is measured at each wind turbine and at the source. Wind speed datasets used to energize the rotor blades are chosen at ID 12 (31.28°N, 104.52°W), ID 39 (31.46°N, 104.61°W), and ID 110 (31.68°N, 104.72°W). The three sites spread from southeast to northwest and are about 20 km away from each other, which can represent a geographically widely distributed wind farm. The rated power of this small wind farm is 90 MW, with a 30 MW power rating for each partially aggregated wind turbine. Data is drawn solely from January 2004 instead of the entire year for visual comparison purposes.

Power from the source is compared with the aggregated power from NREL. The wind power ramping up and down for January 5th to 8th is displayed in Figure 16 (a), while some of the plateau regions from 23rd to 26th are in Figure 3.9(b). The power output from the small wind farm simulated by the quasi-dynamic model meets that from NREL well for the ramping regions, however, minor mismatches around 1 p.u. in the plateau regions are caused by different stalling properties dominated by C_p of the rotor blades.

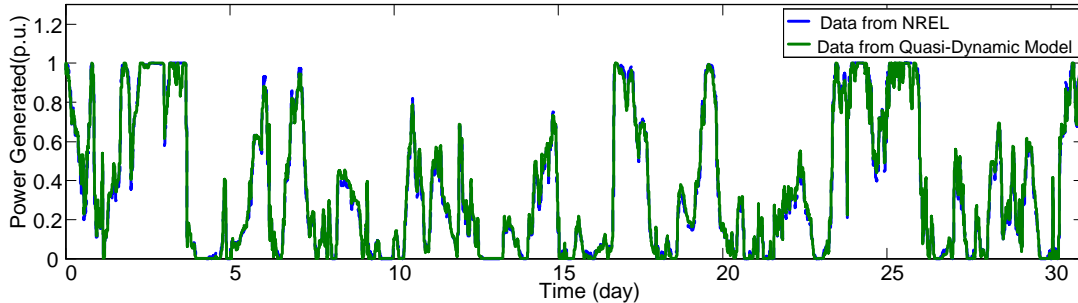


Figure 3.8: Comparison of power released by NREL and power simulated by the quasi-dynamic model. The analysis is executed using the data at location ID 12 in January 2004 in [1].

3.5 Summary

To seek for the possibility of simulating wind farms using individual or partially aggregated wind turbines and to reduce the computational complexity for over long-term operations, model reductions for Type 4 direct-drive wind turbines have been proposed in this section. The reduced models feature simpler configurations and are more time efficient than the full model, while retaining crucial system dynamics. The steady-state and dynamic operations meet the full model well, which speaks for their validity and efficacy. Further, the third stage (quasi-dynamic) model reduction has been validated using real-world wind speed data and compared with the power datasets provided by NREL throughout the year of 2004. Aggregations representing a small widespread wind farm have been proved feasible using the proposed quasi-dynamic model. Data from the simulation matches the NREL power both in time-series waveforms and statistical analysis. Therefore, the reduced

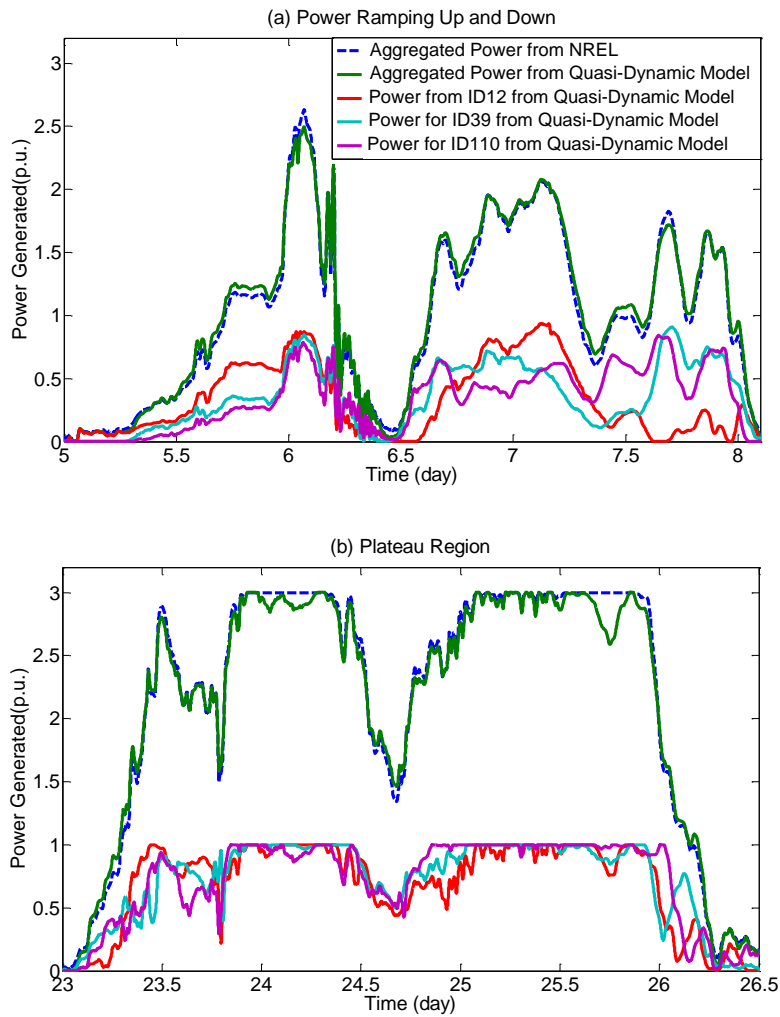


Figure 3.9: Comparison of aggregated power from three wind turbines of ID 12, ID 39 and ID 110. Sub-figure (a) shows the working condition of power ramping up and down in a fluctuated wind speed while sub-figure (b) illustrates the plateau region with a relatively steady state. The base is 30 MW.

wind turbine model is practical for simulating long-term operations dynamically with reduced CPU runtime.

Chapter 4

Quantification of Wind Power Variability

The conditional range metric (CRM) has been proposed to quantify the intra-hour variability of wind power [43]. Using a moving time window of desired length for observing the variability, this algorithm generates lower and upper power-deviation series a_{k,l_j} and b_{k,l_j} from the wind power time-series under analysis. A quantile model and a joint probability density matrix are then employed to calculate the conditional range at production level l_j for a given coverage rate p . Initial applications of the CRM have been proposed and demonstrated in [8, 43, 44]. The CRM is capable of estimating the future wind power variability from the existing data and predicting a probabilistic forecast. System reserves and suitable control strategies can be determined in a purpose of reducing the power variations of wind farms. Impacts of wind power technology (Type 1 to 4 wind turbines) and wind farm size on variability have been analyzed in [44]. This analysis gives reasonable applications on wind farm planning and cooperation level. Coordinating with ESS, the power variations will be more controllable and desirable. Further work can be initiated in sizing and allocating the energy storage components in a system design level. A method of determining ESS capacity using CRM to reduce wind power variability was proposed in [8]. The applications of CRM are not limited to

quantifying wind power variability, but can also be extended to other renewable energy profiles such as photovoltaic or tidal power generation. It might even be applicable for short-term load variation analysis.

Despite the effectiveness of the CRM in quantifying the wind power variability, this method requires a large volume of sampled power data over a long time span. Under scarce or noisy data, the quantile model has been found inadequate. Furthermore, the computational burden of generating the joint probability density matrix could be arduous, as it involves multiplication of two high order matrices.

The objective of this section is to extend the CRM-based method developed in [43] by reformulating the probability models for adaptability and robustness in scarce or noisy data. Rather than employing the quantile model, this work considers gamma distributions [45] [46] for the deviation series at each production level without introducing the joint probability density matrix. The shape and inverse scale parameters α and β of this proposed distribution are estimated using the maximum likelihood estimator (MLE) [47–49]. In order to verify the accuracy of the chosen distribution and its estimated parameters, the Bayesian estimator (BE) is developed as a posterior joint probability model conditioned by the wind power-deviation series. The choice of possible priors is discussed according to the gamma likelihood function. Although multiple priors have been provided in [50], this work implements the non-informative Jeffreys prior due to the lack of information from the data. The complexity of the posterior distribution prohibits the direct calculation

for closed-form solutions of $E(\alpha)$ and $E(\beta)$, therefore, a modified rejection-sampling algorithm is derived to estimate $E(\alpha)$ and $E(\beta)$ by taking the mean value of the paired sample points from the posterior distribution. The match between the two estimation methods indicates valid parameters at each production level. Using data from the National Renewable Energy Laboratory (NREL) and their down-sampled subsets, the proposed CRM is compared with the existing CRM defined in [43]. For the sake of clarity, the proposed CRM for scarce and noisy data applications shall be designated sCRM, while the existing CRM [43] with the quantile model is oCRM.

Section 4.1 summarizes the oCRM concept and its computational method in detail, while Section 4.2 describes the probability model, parameter estimation, and reduction of the joint probability density matrix for the proposed sCRM. The Bayesian data analysis assuming a gamma distribution likelihood function is performed in Section 4.3. Based on the comparisons presented in Section 4.4, sCRM is shown to be more adaptive and accurate than oCRM under sparse wind power sampling record and noisy data in power-deviation series.

4.1 The Conditional Range Metric in Wind Power Variability

4.1.1 Concept of Quantifying Wind Power Variability

Proposed in [43], the fundamental concept of the CRM is to measure the wind power dispersion statistically within a given observation interval.

The varying wind power X can be defined as a range $R = \max X - \min X$. Note that $\max X$ can reach up to the nameplate rated power while $\min X$ can be as small as zero if the wind speed is below the cut-in speed. Therefore, the maximum range of R might be the rated wind power of a wind turbine or wind farm P_{rated} , however, R is unnecessarily at P_{rated} all the time. During a shorter time frame, such as intra- or inter-hours, the range R can be much smaller than P_{rated} . Shown in Figure 4.1, the 24-hour wind power generation has a range of 0.9 p.u., i.e., from 0.1 to 1.0 p.u. If a shorter time window K_i is used to observe the power profile, e.g., approximately from 1:00 p.m. to 4:00 p.m., the power variability represented by R is only about 0.4 p.u. (from 0.19 to 0.59 p.u.).

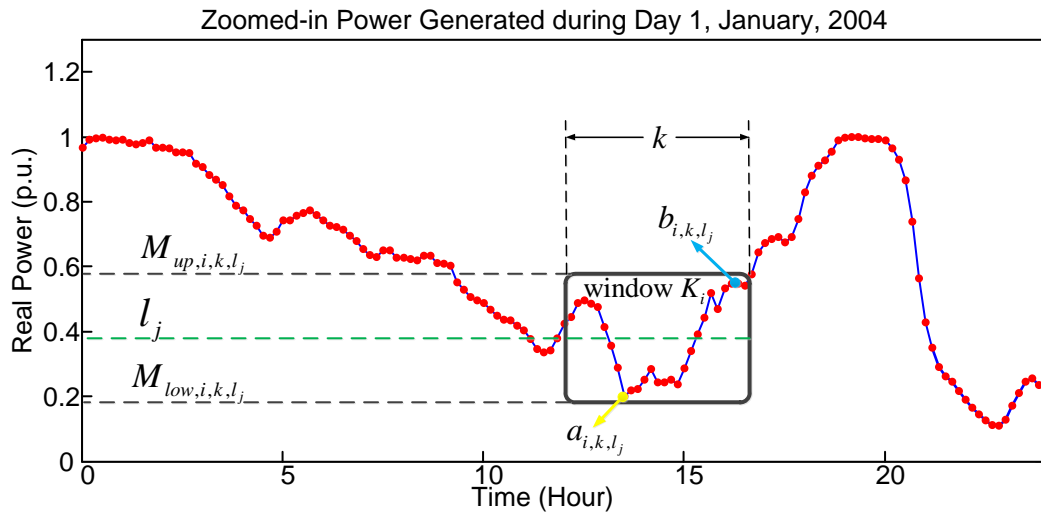


Figure 4.1: Wind power variability related to a time window. Production level l_j and power-deviation series are derived through the moving average of all sampled data points.

4.1.2 Definition of the Conditional Range Metric

Referring to Figure 4.1, the conditional range of the wind power output $x(t)$ during an interval $[t_0, t_{0+k}]$ starting from t_0 with k -long duration is defined as M_k :

$$M_k = M_{up_k} - M_{low_k} \quad (4.1)$$

M_{up_k} and M_{low_k} are the upper and lower bounds within the interval shown in Figure ???. Typically, the wind power output is recorded by monitoring equipment in terms of sampled points. The discrete sampled data is a time series X_n instead of the continuous function of $x(t)$. The subscript n in X_n represents the number of the sampled power data points where $n = 1, 2, \dots, N$. Therefore, the conditional range M_k over a k -long observation interval can be rewritten as:

$$M_{i,k} = M_{up_{i,k}} - M_{low_{i,k}} = \max_{n \in K_i} X_{i,n} - \min_{n \in K_i} X_{i,n} \quad (4.2)$$

where K_i is the instantaneous time window with k -long observation interval on the sampled data $[i, i + k - 1]$ (i is the starting point of K_i and its value is $i = 1, 2, \dots, N - k$). Sliding the time window along the domain of the sampled power data, the paired values $[M_{up_{i,k}}, M_{low_{i,k}}]$ will vary according to $\max X_{i,n}$ and $\min X_{i,n}$ introduced above, resulting in a tighter range of $M_{i,k}$ rather than R . Taking the average over all values of the power series X_n in window K_i , a certain production level l_j can be determined. The subscript j of l_j indicates

the desired resolution, e.g., a 0.1-p.u. resolution can be represented as $l_{0.1}$. A commonly-used j in conditional range plotting is 0.01. Due to the operation $[i, i + k - 1]$ ($i = 1, 2, \dots, N - k$), the moving average process generates a series of l_j with the same resolution as X_n . Thus, the complete CRM considering all the above parameters can be defined as:

$$CRM_{i,k,l_j} = [M_{up_{i,k,l_j}}, M_{low_{i,k,l_j}}] \quad (4.3)$$

The conditional range is the distance between the paired upper and lower bounds:

$$CR_{i,k,l_j} = M_{up_{i,k,l_j}} - M_{low_{i,k,l_j}} \quad (4.4)$$

CRM_{i,k,l_j} and CR_{i,k,l_j} serve as a measure of wind power variability over a given observation interval for the starting point i , the length of the interval k , and the production level l_j . Using this method, the window K_i in Figure 4.1 can be evaluated as $CRM = [0.19, 0.59]$ p.u. and $CR = 0.4$ p.u. with $i = 13$ hr, $k = 3$ hr, and $l_j = 0.39$ p.u.

4.1.3 Computational Methodology of CRM and CR

The definition of CRM in (4.3) and (4.4) gives a coverage rate of 100% because $M_{up_{i,k,l_j}}$ and $M_{low_{i,k,l_j}}$ are chosen as the maximum and minimum values within the time window K_i . The research problem, consequently, can be formulated as: finding a pair of $[M_{up_{i,k,l_j}}, M_{low_{i,k,l_j}}]$ for a desired coverage rate

p other than 100% at a particular production level l_j . The mathematical expression of the aforementioned problem is to satisfy the following probability inequality:

$$P \left(\left\{ \inf_{n \in K_i} X_n \geq M_{low_k, l_j, p} \right\} \cap \left\{ \sup_{n \in K_i} X_n \leq M_{up_k, l_j, p} \right\} \middle| \bar{X}_n = l_j \right) \geq p \quad (4.5)$$

where the new variable \bar{X}_n is the averaged wind power for all sampled points within K_i .

Although the CRM has been described mathematically in (4.5), it is unsolvable due to the lack of information for the variables. To extract the necessary information from the existing data, raw wind power data must be processed and a suitable probability model must be developed. For this purpose, power-deviation series are introduced as follows:

$$a_{i,k} = \bar{X}_{i,n} - \min X_{i,n} \quad n \in K_i \quad (4.6)$$

$$b_{i,k} = \max X_{i,n} - \bar{X}_{i,n} \quad n \in K_i \quad (4.7)$$

The two series specified in (4.6) and (4.7) are coincident with their corresponding production level l_j , generating a unique pair of a_{i,k,l_j} and b_{i,k,l_j} for every K_i . (4.5) can then be converted into the following expression using (4.6) and (4.7):

$$P \left(M_{low_{k,l_j,p}} \leq l_j - a_{k,l_j} \right) = P \left(M_{up_{k,l_j,p}} \geq b_{k,l_j} + l_j \right) = p \quad (4.8)$$

By redefining the problem in (4.8), the determination for $M_{up_{k,l_j,p}}$ and $M_{low_{k,l_j,p}}$ is simply to solve the probability equation. Since the coverage rate p is known, a probability model must be built to determine $M_{up_{k,l_j,p}}$ and $M_{low_{k,l_j,p}}$ satisfying (4.8) at a given production level l_j . Rank quantile models are implemented for the deviation series a_{k,l_j} and b_{k,l_j} with a resolution of $1/q$. The rank quantiles $Q_{a_{k,l_j}}(r/q)$ and $Q_{b_{k,l_j}}(r/q)$ are the r th q -quantile of a_{k,l_j} and b_{k,l_j} , respectively, where $r = 1, 2, \dots, q$. If the elements in the deviation series a_{k,l_j} and b_{k,l_j} are condensed enough, the quantile resolution q will separate them into q disjoint sets Sa_{k,l_j} and Sb_{k,l_j} . The joint probability density matrix can be calculated from:

$$V_{k,l_j}(i, j) = P \left[\{a \in Sa_{k,l_j}\} \cap \{b \in Sb_{k,l_j}\} \right] \quad (4.9)$$

Hence, the CRM defined in (4.3) can be restated as follows:

$$\begin{aligned} CRM_{k,l_j,p} &= \left[M_{up_{k,l_j,p}}, M_{low_{k,l_j,p}} \right] \\ &= \left[l_j - Q_{a_{k,l_j}}(\tau_p), l_j + Q_{b_{k,l_j}}(\tau_p) \right] \end{aligned} \quad (4.10)$$

where τ_p is computed from the joint probability density matrix V_{k,l_j} . τ_p is given as follows:

$$\tau_p = \inf \left\{ \sum_{i=1}^{\tau_p} \sum_{j=1}^{\tau_p} V_{k,l_j}(i, j) \geq p \right\} \quad (4.11)$$

4.2 Conditional Range Metric for Scarce and Noise Data

Definitions and computational methodology of the oCRM have been introduced in Section 4.1. The performance of the oCRM is desirable when the volume of the wind power data is large. It is still possible, however, to implement a more substantial probability model, rather than the rank quantile, to improve the algorithm adaptability under sparse data and to avoid calculating the joint probability density matrix V_{k,l_j} defined in (4.9).

4.2.1 Probability Model of Deviation Series

The metric $M_{up_{k,l_j,p}}$ and $M_{low_{k,l_j,p}}$ is modeled as the rank quantile calculated from the joint probability density matrix V_{k,l_j} . Although the quantile estimation does not introduce any bias of fitting the non-informative data into a certain distribution that might cause the mismatch between the probability model and the data, the quantile estimation does have its innate drawbacks:

- The rank quantile is a probability in terms of rank order. It requires large sampled data to achieve the desired accuracy. The quantile will be inaccurate if the data points are scarce but the quantile resolution q is high;

- Data points will become redundant if the required resolution of probability q is lower than the total data points. Thus, the quantile model is optimized only if the q is equal to the total data points;
- Because the quantile model consists of discrete data points without any continuous function, statistical analyses such as modeling of prior and posterior distributions, regression, and Bayesian data analysis are not available; and
- Bad data points may significantly affect the accuracy. Abnormal values caused by the unusual wind power change in the deviation series a_{k,l_j} and b_{k,l_j} will lead to the failure of calculating a credible conditional range in terms of spikes and irregular points in the plot when the coverage percentage p is high. A conditional range with a 95% coverage rate is considered high.

Based on the above aspects, the probability model of the oCRM can be improved by adopting a suitable probability distribution that will cover the general histogram of the deviation series a_{k,l_j} and b_{k,l_j} . There is a trade-off between being objective in choosing a probability model and being accurate and more adaptive under all data conditions. This concern can be interpreted as that the probability model must maintain its general accuracy, even though the total number of the deviation series sets over the entire production level l_j and the elements in each set will vary according to the expected resolution of l_j . A typical 0.01-p.u. resolution of l_j is sufficient to deliver a credible reference

for most analytical cases. Intuitively, a more condensed l_j can render more precise steps, creating a smoother curve for the conditional range plotting. With the refined resolution of l_j , more deviation series sets should be generated by (4.6) and (4.7), which will reduce the available data points in each set, further impairing the performance of the probability model. Therefore, the distribution proposed for the probability model must be adaptive and without bias for the data distributed among the vast number of the deviation series sets. Additionally, other requirements for the desired probability distribution are summarized as follows:

- The random variables in the chosen distribution must have a range from zero to infinity;
- The distribution must cover most of the existing data for each deviation series set at every production level and even possible data appearing in the future; and
- The shape of the probability density function should match the histogram of the data.

To satisfy the above requirements, discrete distributions such as binomial or Poisson distributions should never be adopted because they perform worse than the quantile probability estimator. The commonly-used Gaussian distribution fails to match both the shape and the range of the data. A beta distribution holds a similar shape, yet cannot fit in the first requirement. Finally, the choice is settled with chi-squared distribution and gamma

distribution. Both distributions meet the data histogram and have random variables ranging from zero to infinity. In fact, the chi-squared distribution is a special case of the gamma distribution with zero included in the variables. Considering an ideal condition of the power deviation series, zero is unlikely to appear in the deviation series. Moreover, the gamma distribution possesses a simpler expression of the probability density function compared to that of the chi-squared distribution, and it has relatively mature parameter estimation methods, making it the best choice for the study in this work. Hence, a two-parameter $Gamma(\alpha, \beta)$ distribution [45] [46] is chosen to satisfy the above constraints:

$$a_{k,l_j} \sim Gamma\left(\alpha_{a_{k,l_j}}, \beta_{a_{k,l_j}}\right) \quad (4.12)$$

$$b_{k,l_j} \sim Gamma\left(\alpha_{b_{k,l_j}}, \beta_{b_{k,l_j}}\right) \quad (4.13)$$

The probability density function of the two-parameter $Gamma(\alpha, \beta)$ distribution is defined as follows:

$$p(Y_m|\alpha, \beta) = \frac{\beta^\alpha}{\Gamma(\alpha)} Y_m^{\alpha-1} e^{-\beta Y_m} \quad (m = 1, 2, \dots, n_{l_j}, \alpha, \beta > 0) \quad (4.14)$$

where Y_m denotes the elements from the deviations series. α and β are the shape and inverse scale parameters, respectively. n_{l_j} is the total data volume at a certain production level. Γ is the gamma function shown below:

$$\Gamma(\theta) = \int_0^{\infty} x^{\theta-1} e^{-x} dx \quad (4.15)$$

4.2.2 Parameter Estimation for the Probability Model

By estimating the shape parameter α and the inverse scale parameter β for each production level l_j appropriately, the discrete quantile model for the oCRM can be improved by fitting the data into the continuous gamma distribution. Approaches of determining α and β have been discussed in [47–53]. In this section, Maximum likelihood estimators(MLE) are employed for this purpose. Due to the difficulties of identifying bad points in the deviation series a_{k,l_j} and b_{k,l_j} , the MLE can minimize the impact of single or even several bad points by finding the maximum value of the likelihood function across the entire dataset. The inaccuracy caused by these minor bad points will be ‘diluted’ by the large amount of good data points. Note that the prerequisite of MLE is to ensure samples are independent. In power time-series, samples are weakly correlated instead of strictly independent; however, the likelihood function is formulated for the deviation series rather than the original time-series. Due to the problem formulated in (4.5), data independence could be established by taking the maximum and minimum operations of the interval K_i in Figure 4.1. The likelihood function for the MLE is specified as a joint probability density function of all observations conditioned by α and β :

$$\begin{aligned}
L(\alpha, \beta | Y_1, Y_2 \cdots Y_{n_j}) &= p(Y_1, Y_2, \dots, Y_{n_j} | \alpha, \beta) \\
&= \prod_{m=1}^{n_j} p(Y_m | \alpha_{k,l_j}, \beta_{l_j}) \quad (4.16)
\end{aligned}$$

Now, the problem is simplified as:

Given the data of Y_1, Y_2, \dots, Y_{n_j}

Determine α and β

such that the value of the likelihood function L will be maximized:

$$\left\{ (\hat{\alpha}_{MLE}, \hat{\beta}_{MLE}) \right\} \subseteq \left\{ \arg \max L(\alpha_{k,l_j}, \beta_{k,l_j} | Y_1, \dots, Y_{n_j}) \right\} \quad (4.17)$$

The estimated values of α and β can then be derived by solving the following equations:

$$\begin{cases} \frac{\partial}{\partial \alpha} \ln L(\alpha, \beta) = 0, & \frac{\partial^2}{\partial \alpha^2} \ln L(\alpha, \beta) < 0 \\ \frac{\partial}{\partial \beta} \ln L(\alpha, \beta) = 0, & \frac{\partial^2}{\partial \beta^2} \ln L(\alpha, \beta) < 0 \end{cases} \quad (4.18)$$

At a certain production level, the two pairs of α and β for the sets a_{k,l_j} and b_{k,l_j} are not identical. Thus, the total number of α and β pairs are determined by the quantity of probability models required according to the resolution of l_j . In this work, the 0.01 p.u resolution will lead to 200 different gamma distributions.

Mathematically, the explicit closed-form solution of (4.18) does not exist, therefore, approaches proposed in [54] can be applied to calculate α and β . This approach is also referred as Brent's method. It is a root-finding algorithm that uses a Lagrangian interpolating polynomial of degree two. Theoretically, it will always converge as long as the value is contained in a given range. The method has been programmed as ready-to-use code in [55]. Under an ideal condition, there will not be any zeroes in the deviation series defined in (4.6) and (4.7). Yet, due to the data density, zeroes may sometimes appear at $l_j = 0$ p.u. and $l_j = 1.0$ p.u. If zero elements occur, the maximum likelihood estimation will face the dilemma of a zero value for the likelihood function L . Moment estimator (ME) is responsible for this particular case as follows [56]:

$$\hat{\alpha}_{ME} = \left(\frac{\bar{Y}}{s}\right)^2, \hat{\beta}_{ME} = \frac{\bar{Y}}{s^2} \quad (4.19)$$

where s is the standard deviation of the data.

In order to test the proposed probability model, field datasets are drawn from the same source as those used in Section 3.4.3. This time, only the power datasets are drawn, discarding the wind speed data. As mentioned before, the best field data resolution available from NREL is of 10-minute intervals, which is considered scarce to perform the wind power variability with $k < 10$ min. Thus, the interpolated data with 1-minute resolution performed in Section 3.4.3 are applied. Although it is controversial to interpolate the raw data due to the possibility that this operation might generate flawed information

between the initial points, higher order piecewise polynomials can be employed to maintain the general continuity of the wind power profile while filling the existing sampled data with interpolants to create more points available for the conditional range calculation.

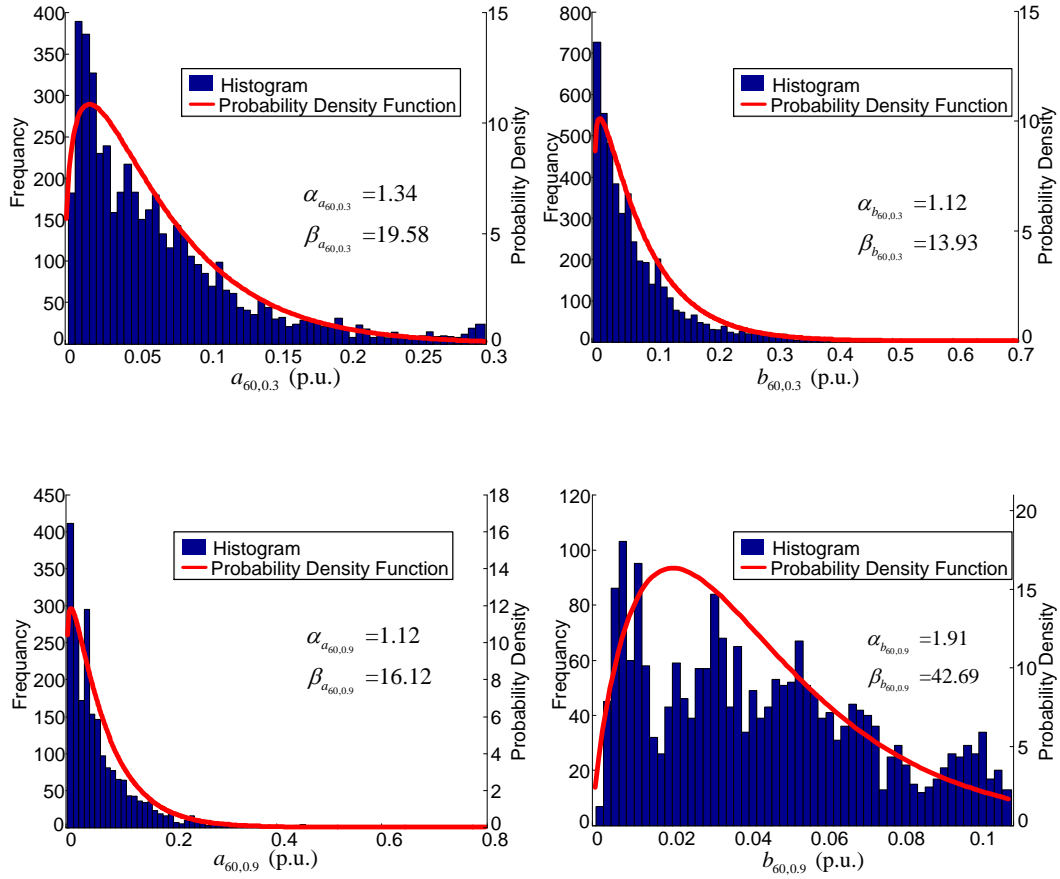


Figure 4.2: Illustration of fitting the deviation series into gamma distributions. They are calculated with $k = 60$ min while the resolution for l_j is 0.01 p.u. The data is chosen from a_{60} and b_{60} with $l_j = 0.3$ p.u. and $l_j = 0.9$ p.u.

Figure 4.2 displays the histograms of the deviation series and their corresponding probability density functions at two production levels, 0.3 p.u.

and 0.9 p.u., respectively. Most data can be fitted into the gamma distribution well, and the MLE renders a pair of parameters α and β , which minimizes the impact of minor irregular values. In Figure 4.2, some points from the upper deviation series $b_{60,0.9}$ fall out of the distribution. This fact is caused by more control events, such as pitch or stalling controls, which occur when the power is close to 1 p.u. Therefore, instead of representing the nature of wind power variability, the power time-series is brought about by different power control strategies employed by the wind turbine. The comprehensive probability density model through the entire production level is displayed as a three-dimensional map in Figure 4.3. It can be seen that there are spikes at $l_j = 0$ p.u. and $l_j = 1.0$ p.u., primarily caused by wind power varying in a much smaller range when the wind turbine is working around the cut-in wind speed and at or above the rated wind speed.

4.2.3 Reduction on the Joint Probability Density Matrix

Governed by (4.9), the joint probability density matrix is responsible for calculating the rank quantile by ensuring that the summation from a certain amount of elements in V_{k,l_j} is equal to the desired coverage rate p . The joint probability density matrix V_{k,l_j} in oCRM is derived by multiplying two matrices denoting the q disjoint sets Sa_{k,l_j} and Sb_{k,l_j} in every production level, therefore, the dimension of V_{k,l_j} is q by q . The computational burden for calculating V_{k,l_j} will be excessive if the desired resolutions of l_j and q are high. Due to the matrix multiplication of calculating V_{k,l_j} , zeroes will present in the

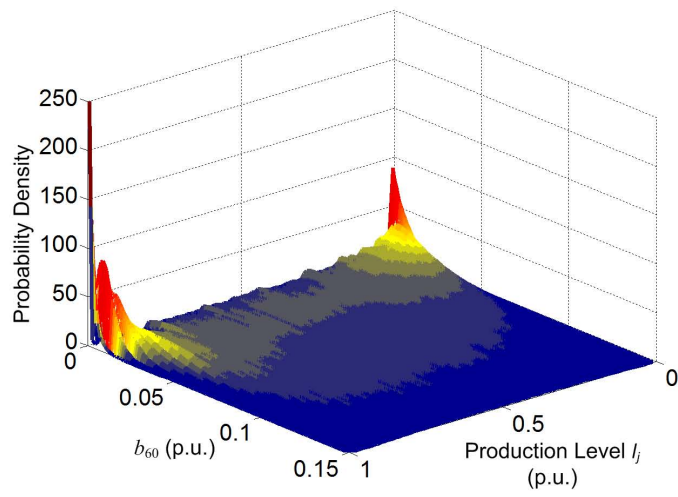
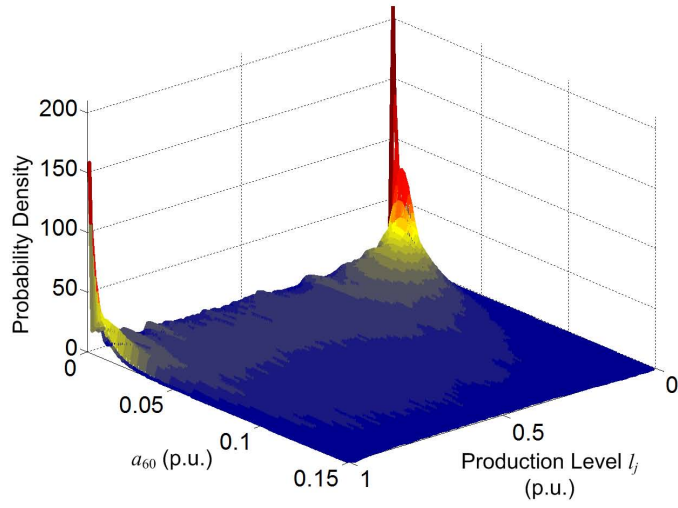


Figure 4.3: Probability density model using gamma distribution approach through the entire production level l_j with a resolution of 0.01 p.u. The length of the analyzed observation interval is $k = 60$ min.

matrix. Thus, the coverage rate p for $M_{up_{k,l_j,p}}$ and $M_{low_{k,l_j,p}}$ must be identical, which indicates i must be equal to j in (4.11). In other words, because of the existing zeroes, it is impossible for V_{k,l_j} to find an asymmetrical coverage rate, such as $p = 0.3$ for $M_{up_{k,l_j,0.3}}$ and $p = 0.9$ for $M_{low_{k,l_j,0.9}}$, at any production level.

For the above reasons, a reduction on the joint probability density matrix V_{k,l_j} will be considered. Instead of reticulating the probability density into a matrix form, it would be better to use the aforementioned gamma distribution model of the power deviation series. One concern for this method might involve the independence issue for the maximum and minimum values in a time window K_i . Since the conditional range aims for an empirical power deviation, the operations of taking the maximum and minimum values in a particular window can be considered independent. Shown in Figure 4.1 as the time window K_i moves point-wise along the time-series power data, each production level l_j is coincident with two deviation points belonging to the deviation series a_{k,l_j} and b_{k,l_j} . Sorted by l_j , both a_{k,l_j} and b_{k,l_j} can be grouped into 100 subsets in respect to a 0.01-p.u. resolution. The probability model in each subset has been introduced as the likelihood function of a gamma distribution. Thus, the desired conditional range for coverage rate p can be derived using the inverse cumulative distribution functions for a particular production level, shown as follows:

$$\begin{aligned}
g_{a_k,l_j,p} &= F^{-1} \left(p_{low} | \alpha_{a_k,l_j}, \beta_{a_k,l_j} \right) = \left\{ g_{a_k,l_j,p} : F \left(g_{a_k,l_j,p} | \alpha_{a_k,l_j}, \beta_{a_k,l_j} \right) = p_{low} \right\} \\
g_{b_k,l_j,p} &= F^{-1} \left(p_{up} | \alpha_{b_k,l_j}, \beta_{b_k,l_j} \right) = \left\{ g_{b_k,l_j,p} : F \left(g_{b_k,l_j,p} | \alpha_{b_k,l_j}, \beta_{b_k,l_j} \right) = p_{up} \right\}
\end{aligned} \tag{4.20}$$

where the probability p_{low} and p_{up} might not necessarily be equal. To estimate a symmetrical probability range, it is set to $p_{low} = p_{up} = p$. F is the cumulative distribution function defined as:

$$p = F(g|\alpha, \beta) = \frac{\beta^\alpha}{\Gamma(\alpha)} \int_0^g t^{\alpha-1} e^{-\beta t} dt \tag{4.21}$$

Applying the NREL wind power data to (4.20), the cumulative distribution can be realized as the coverage rate regarding the lower range $g_{a_k,l_j,p}$ and upper range $g_{b_k,l_j,p}$. Figure 4.4 shows the mesh of $g_{a_{60}}$ and $g_{b_{60}}$.

By replacing $Q_{a_k,l_j}(\tau_p)$ and $Q_{b_k,l_j}(\tau_p)$ with $g_{a_k,l_j,p}$ and $g_{b_k,l_j,p}$ in (4.10), the CRM with new probability model is expressed as follows:

$$CRM_{k,l_j,p} = \left[l_j - g_{a_k,l_j,p}, l_j + g_{b_k,l_j,p} \right] \tag{4.22}$$

while the corresponding conditional range in (4.4) is transformed as: $CR_{k,l_j,p} = g_{b_k,l_j,p} + g_{a_k,l_j,p}$. The CRM constrained by (4.22) is referred as sCRM for its improved probability model.

Figure 4.5 illustrates the portfolio of CRM_{60} with $k = 60$ min, representing the wind power variability within an intra-hour observation duration.

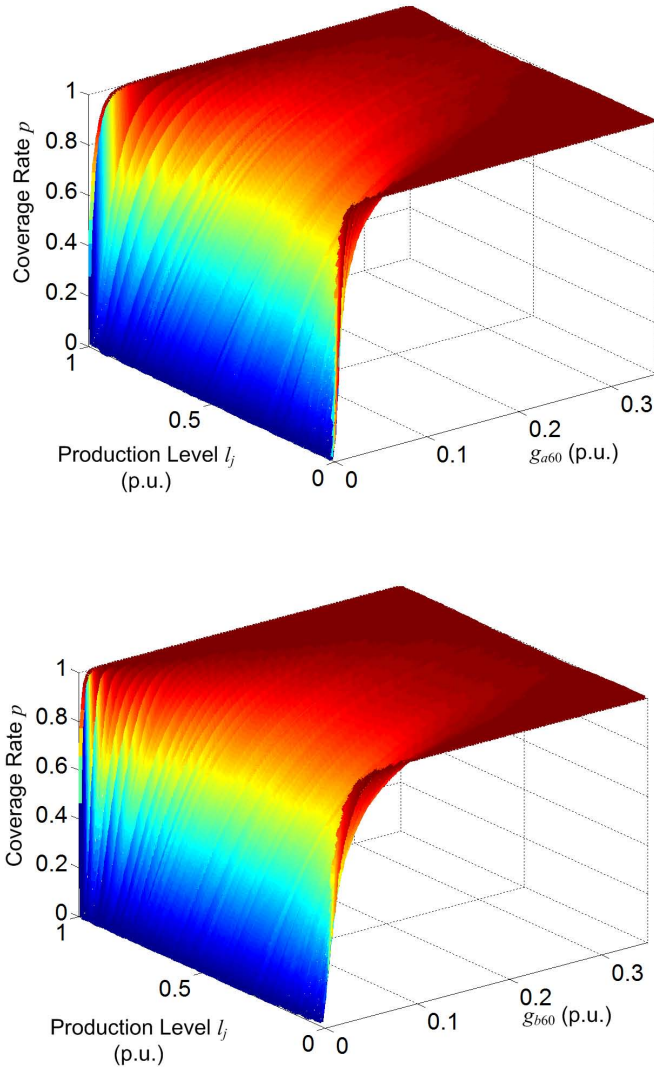


Figure 4.4: Three dimensional display of the upper and lower deviation through the entire coverage rate p and production level l_j . The length of the observation interval is $k = 60$ min.

The upper bound M_{up60} and the lower bound M_{low60} are in red and blue, respectively. The desired conditional range readings are the distances from the

upper red to the lower blue. If the mesh in Figure 4.5 is laminated by the p axis, each piece will be showing a 2-D conditional range metric across all production levels under a certain coverage rate; while the slices from l_j will denote how the range follows different coverage rates on a given production level. The two-dimensional figures regarding a given coverage rate or production level are also presented in Figure 4.5.

4.3 Bayesian Inference for the Probability Model

In order to confirm that the gamma distribution model and its estimated parameters are suitable for the existing data (power-deviation series), the Bayesian estimator (BE) is applied using Bayesian inference.

The Bayesian inference is the process of developing a probability model for a set of data and summarizing the parameters of this model in terms of a posterior probability distribution [57] [58]. For the purpose of this work, the Bayesian inference considers the estimated parameters as a joint distribution conditioned by the data in which the power-deviation datasets are included in the likelihood function and a proper prior is chosen to follow Bayes' rule:

$$p(\alpha, \beta | Y_m) \propto p(Y_m | \alpha, \beta) p(\alpha, \beta) \quad m = 1, 2, \dots, n_{l_j} \quad (4.23)$$

The expectations $E(\alpha)$ and $E(\beta)$ in the posterior joint distribution can speak for their estimated value of α and β . If the parameters derived from the Bayesian inference meet the results from MLE well, they are considered to be

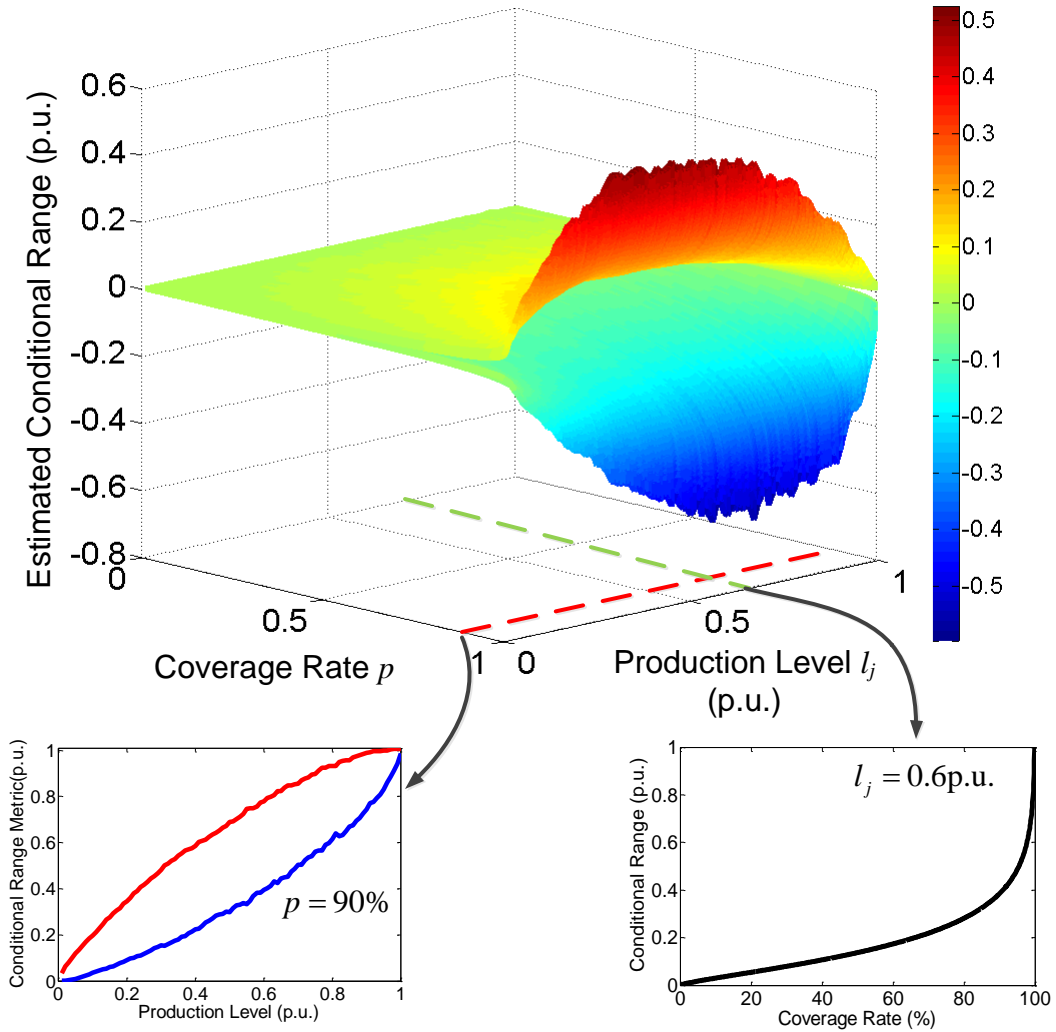


Figure 4.5: Conditional range estimation through the entire domain of production level l_j and coverage rate p with an observation interval $k = 60$ min. The red mesh is M_{up60} calculated from g_{b60} while the blue mesh represents M_{low60} derived from g_{a60} .

proper for the power-deviation datasets and the gamma distribution is proved to be suitable.

4.3.1 Determination of the Prior

As the initial step, a prior must be chosen to perform the Bayesian inference. The different choices for priors can be arguable and, sometimes, might be more subjective rather than objective because the empirical knowledge and peripheral information from the datasets might not be available. In [51], a prior of $1/\beta$ is proposed and successfully derives the posterior distribution based on simulated data. However, it is an improper prior, because it cannot be normalized and its integral over the range of β is infinity. Various priors for advancing BE of the gamma distribution are discussed in [59] without providing further detailed evidence of selecting an appropriate form under different circumstances. Because the power-deviation series a_{k,l_j} and b_{k,l_j} are processed datasets from the discrete wind power series, there is no more referential information for determining the prior. Thus, a non-informative prior should be considered as the same situation in [60]. Generally, one of the most prevalent non-informative priors is the conjugate prior. The conjugate prior is capable of developing detailed hierarchical probability models, which have a better representation of modeling the deviation series. Although simple and common, the conjugate prior will introduce hyper-parameters as known values for $p(\alpha, \beta)$. For the case with both α and β unknown, the conjugate prior of $p(\alpha, \beta)$ is [58]:

$$p(\alpha, \beta) \propto \frac{p^{\alpha-1} e^{-\beta q}}{\Gamma(\alpha)^r \beta^{-\alpha s}}$$

where p , q , r , and s are predetermined hyper-parameters. The lack of information prohibits the guess of these hyper-parameters. For some cases, giving arbitrary numbers to these hyper-parameters will not affect the estimator when the likelihood function with tremendous data volume dominates the posterior distribution. An erroneous posterior distribution might occur if the data cannot overwhelm the impacts from hyper-parameters; therefore, the conjugate prior is not preferable for the concerns addressed in here.

Without introducing additional unknown values, the Jeffreys prior can be employed. It is a well-known weak prior proposed by Jeffreys in 1961 to tackle situations with little information about the parameters. With both unknown α and β , the Fisher information matrix for the Jeffreys prior is described as follows:

$$I(\alpha, \beta) = -E \left[\frac{\partial^2 \ln P(Y_m | \alpha, \beta)}{\partial \alpha \partial \beta} \right]_{2 \times 2} = \begin{bmatrix} PG(1, \alpha) & -1/\beta \\ -1/\beta & \alpha/\beta^2 \end{bmatrix} \quad (4.24)$$

where $PG(1, x) = \sum_{i=0}^{\infty} (x+i)^{-2}$ is the polygamma function. The Jeffreys prior is derived from its definition [61]:

$$p(\alpha, \beta) \propto \sqrt{|I(\alpha, \beta)|} = \frac{\sqrt{\alpha PG(1, \alpha) - 1}}{\beta} \quad (4.25)$$

Since the Jeffreys prior does not introduce extra variables or unknowns, the posterior joint distribution conditioned by the data will contain only α and β

as variables, and this leverage facilitates the estimation of posterior expectations for these two parameters. The derived Jeffreys prior is a non-normalized distribution in which the integral over α and β is a finite constant rather than 1. The prior need not be normalized if (4.23) is applied, because the normalized constant will be recalculated after the posterior distribution has been derived.

4.3.2 Posterior Analysis

Substituting the prior (4.25) and likelihood function (4.16) into (4.23), the non-normalized posterior distribution from the Bayesian inference is performed as:

$$p\left(\alpha, \beta | Y_1, Y_2, \dots, Y_{n_j}\right) \propto \sqrt{\alpha PG(1, \alpha) - 1} \cdot \frac{\beta^{n\alpha-1}}{\Gamma(\alpha)^n} \prod_{m=1}^{n_j} Y_m^{\alpha-1} \cdot e^{-\beta \sum_{m=1}^{n_j} Y_m} \quad (4.26)$$

It is obvious that the posterior distribution does not belong to any standard distribution family; thus, it is impossible to calculate the expectations from the knowledge of standard distributions. The complexity of (4.26) also leads to a dead end of using the definition to find $E(\alpha)$ and $E(\beta)$ as well as the normalized constant. The Bayesian estimators for $E(\alpha)$ and $E(\beta)$ cannot be completed in a direct manner and other approaches must be considered.

Instead of computing $E(\alpha)$ and $E(\beta)$ analytically, paired sample points can be drawn from the posterior joint distribution by sampling algorithms. If

the sample size is large enough, the mean value of these paired sample points will converge to the true value of $E(\alpha)$ and $E(\beta)$. Due to the unknown normalized constant in (4.26), it is preferable to apply rejection sampling rather than other common sampling methods such as Gibbs or importance sampling methods. Rejection sampling is accessible to sample independently from a distribution that needs to be specified only up to a constant integration, i.e. the sampling procedure can be conducted with $q(x)$ instead of $p(x)$, where $q(x) = c \cdot p(x)$ for an unknown value of c . This method is effective even when the value of c does not have a closed form, which is similar to the normalized constant in (4.26) [62–64].

To perform the rejection sampling, an envelope function $q_{en}(x)$ must be defined such that $q_{en}(x) \geq q(x)$ for all x in the domain of $p(x)$. In other words, $q_{en}(x)$ can be a constant c_{en} satisfying $c_{en} \geq \sup_x \{q(x)\}$. The following steps can then be taken in a loop until the desired sample size has been reached:

- Step 1. Generate a random variable x_{sample} from the domain of $p(x)$;
- Step 2. Independently generate y_{sample} from the uniform distribution $U \sim (0, c_{en})$;
and
- Step 3. If $y_{sample} \leq q(x_{sample})$, accept x_{sample} as a valid sample point; otherwise, reject x_{sample} and go back to Step 1.

Though simple, the algorithm of the rejection sampling must be modified for the application in this case. Because the posterior distribution is a joint distribution of α and β , $q(x)$ becomes a bivariate function $q(\alpha, \beta)$:

$$q(\alpha, \beta) = \sqrt{\alpha PG(1, \alpha) - 1} \cdot \frac{\beta^{n\alpha-1}}{\Gamma(\alpha)^n} \prod_{m=1}^{n_{l_j}} Y_m^{\alpha-1} \cdot e^{-\beta \sum_{m=1}^{n_{l_j}} Y_m} \quad (4.27)$$

The envelope constant c_{en} then turns into a plane A_{en} on the same coordinates of $q(\alpha, \beta)$.

It should be noted that the total volume of the data points m in a_{k,l_j} and b_{k,l_j} will range from several hundred up to more than ten thousand at different production levels, leading to an extremely high upper bound A_{en} of (4.27), sometimes even larger than 2^{12000} . This indicates that neither A_{en} nor $q(\alpha_{sample}, \beta_{sample})$ can be generated by any simulation software. Thus, the rejection sampling must only be done in logarithmic terms. Hence (4.27) becomes:

$$\begin{aligned} \ln \{q(\alpha, \beta)\} &= \frac{1}{2} \ln(\alpha PG(1, \alpha) - 1) + (n\alpha - 1) \ln(\beta) \\ &\quad - n \ln(\Gamma(\alpha)) + (\alpha - 1) \sum_{m=1}^{n_{l_j}} \ln(Y_m) - \beta \sum_{m=1}^{n_{l_j}} Y_m \end{aligned} \quad (4.28)$$

Working with (4.28), the modified rejection sampling algorithm is summarized in Steps 4 to 7 as follows:

Step 4. Generate a bivariate paired sample $(\alpha_{sample}, \beta_{sample})$ from the domain

$$D \subseteq \{\alpha > 0, \beta > 0\};$$

Step 5. Independently generate u_{sample} from the uniform distribution $U \sim (0, 1)$;

Step 6. Define the envelop function as $\ln(A_{en}) = \ln(u_{sample}) + \sup_x \{\ln [q(\alpha, \beta)]\}$;

and

Step 7. If $\ln(A_{en}) \leq \ln [q(\alpha_{sample}, \beta_{sample})]$, accept both α_{sample} and β_{sample} as paired sample $(\alpha_{sample}, \beta_{sample})$; otherwise, reject $(\alpha_{sample}, \beta_{sample})$ and go back to Step 4.

Using the modified rejection sampling, 10^5 paired sample points are drawn at each production level. The mean values of these paired sample points reflect the values from BE for parameters α and β . Comparisons of estimated α and β by MLE and BE are shown in Figure 4.6. To shorten the run time of sampling and for a better visual inspection, the resolution of the production level is set to 0.1 p.u. instead of 0.01 p.u. in the previous analysis. Due to the reduced resolution, it would be better to make comparisons at the vertices of the solid line. The match from the two methods illustrates the validity of parameter estimation for the probability model in (4.12) and (4.13).

Relative estimation errors are listed in Table 4.1 for an observation interval of $k = 60$ min. The overall errors are minute throughout the production level; however, larger errors can be found from $l_j = 0.7$ p.u. to $l_j = 0.9$ p.u. The increase of the relative error is generally caused by fewer data points in Y_m . The standard deviations of the errors for a_{60} are $\sigma_\alpha = 0.2136 \times 10^{-3}$ p.u. and $\sigma_\beta = 3.5654 \times 10^{-3}$ p.u., while $\sigma_\alpha = 0.4384 \times 10^{-3}$ p.u. and $\sigma_\beta = 16.5604 \times 10^{-3}$ p.u. are for b_{60} . The larger dispersion of the parameters estimated from the upper deviation series b_{60} is caused by the power control events when the pro-

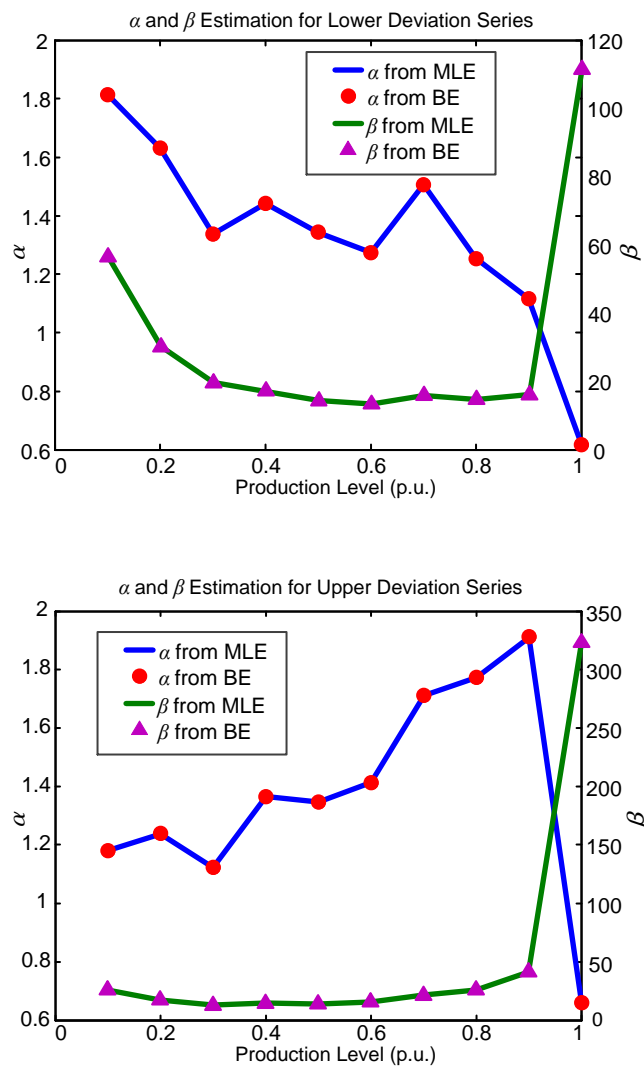


Figure 4.6: Comparison of α and β estimation results from MLE and BE, the left vertical axis is the value of α while the right vertical axis denotes the value of β . The resolution of the production level is increased to 0.1 p.u. for a better visual inspection. The observation interval is still $k = 60$ min.

duction level is towards to 1 p.u., which attributes to the data shown in the fourth sub-figure of Figure 4.2.

Table 4.1: Relative Estimation Errors Between MLE and BE [%₀₀]

l_j [p.u.]	$\alpha_{a_{60}}$	$\beta_{a_{60}}$	$\alpha_{b_{60}}$	$\beta_{b_{60}}$
0.1	0.0786	0.0383	0.0808	0.127
0.2	0.163	0.0849	0.124	0.0977
0.3	0.194	0.131	0.155	0.197
0.4	0.248	0.314	0.235	0.261
0.5	0.289	0.293	0.320	0.341
0.6	0.352	0.410	0.369	0.291
0.7	0.580	0.579	0.593	0.596
0.8	0.525	0.582	0.506	0.494
0.9	0.423	0.463	0.462	0.405
1.0	0.0405	0.0263	0.0622	0.0591

4.4 Performance of the sCRM under Scarce and Noisy Data

Computational methodologies and probability models of oCRM and sCRM are compared and shown as a flow chart in Figure 4.7. The green blocks are the improved components from sCRM, while the reduced and replaced elements from the oCRM branch are marked in orange and red, respectively.

With an accurate probability model and proper estimated parameters, the sCRM is expected to have a robust adaptability for the field data, especially if the data points are sparse. For some cases, the data might be fractional, e.g., the power time-series is only recorded for a few months with an extremely low sampling rate. Under these situations, the oCRM cannot

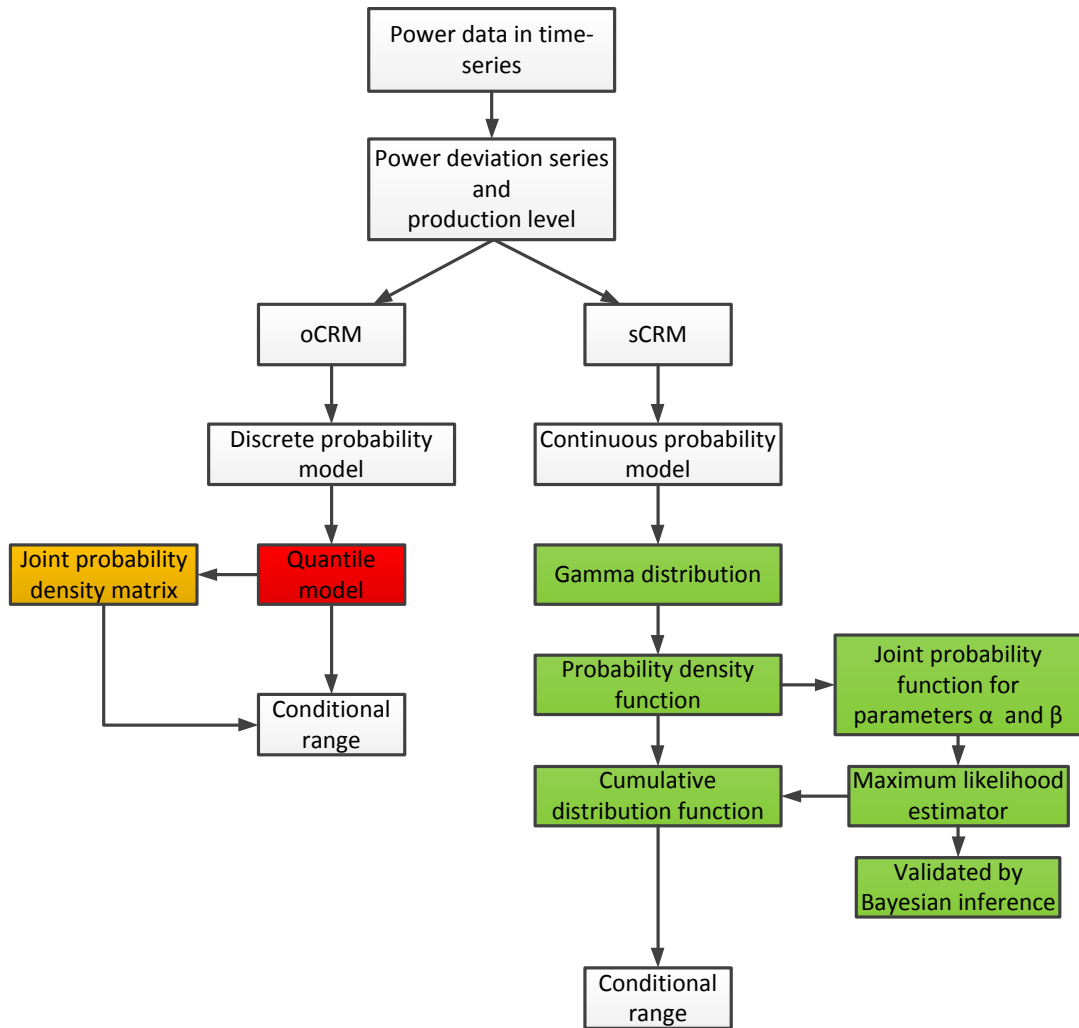


Figure 4.7: Comparisons of computational methodologies between oCRM and sCRM. oCRM uses a discrete quantile model, while sCRM employs the continuous gamma distribution as its probability model.

generate a smooth estimation via the quantile probability model. Due to the scarcity of the data, abnormal or bad data points will impact the accuracy of the quantile model significantly, for the oCRM will take every data point into

account to calculate the conditional range, resulting in a larger error if bad data points are laying in the desired coverage rate. Wind power data ranging from January 2004 to March 2004 is extracted from the interpolated NREL dataset. The data is then down-sampled to a resolution of 10 min, 20 min, and 30 min, respectively. Applying the down-sampled data, the conditional range estimation is performed with a coverage rate of $p = 90\%$, an observation interval $k = 60$ min, and a 0.01 p.u. production level resolution. The conditional ranges estimated from oCRM and sCRM for the initial data and down-sampled data are illustrated in Figure 4.8 and Figure 4.9. As the data point density decreases, the oCRM loses accuracy and the plots drastically become fuzzy. The estimated range may even become unusable for data point resolution greater than 20 min. Under the sparse sampled data, the conditional ranges estimated from both oCRM and sCRM are narrower than under the initial data. This can be explained that because of the longer sampling interval, the total points within k -long time are fewer, causing the incapability of catching wind power variability between the two contiguous sampled data points.

Not only does it behave superiorly under the scarce sampled data, the adaptability of the sCRM can be reflected when the coverage rate p is high. Even with a condensed power dataset, the estimation for a larger coverage rate depends on the percentage of the bad data in the power-deviation series. For instance, with 2% bad points in the total dataset, the coverage rate can only be estimated lower than 98% by the oCRM. Because of the employed gamma

oCRM Estimation:

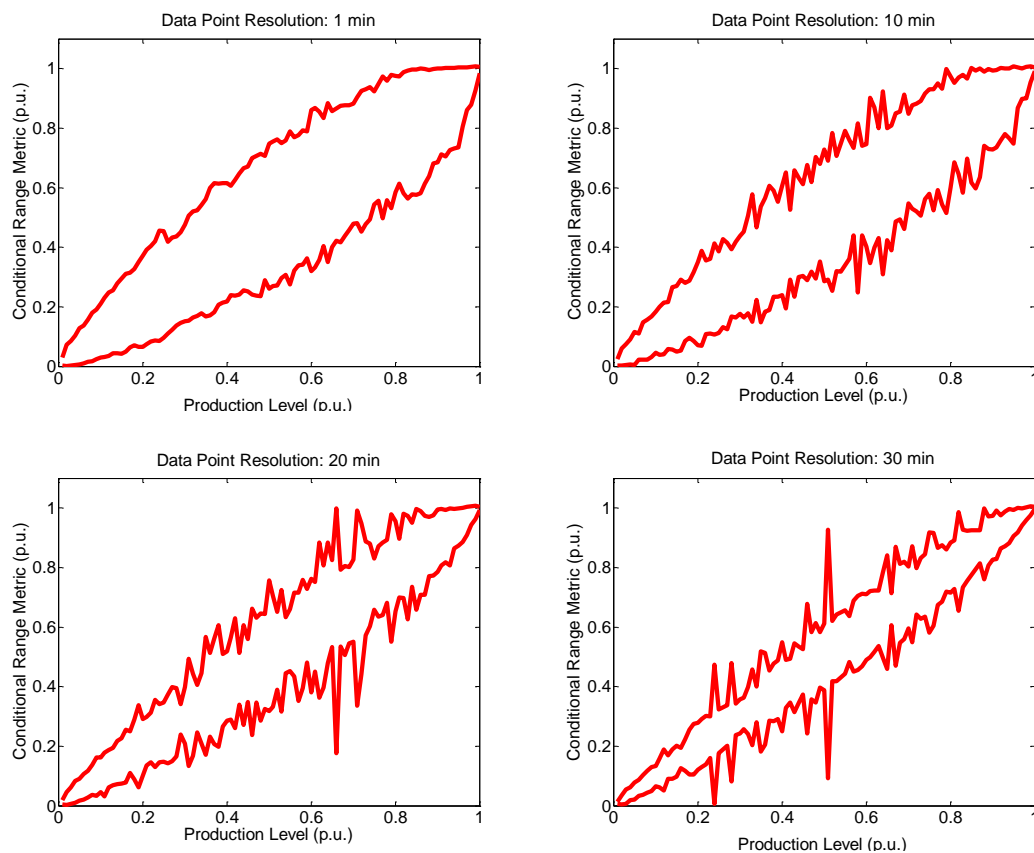


Figure 4.8: The conditional range is plotted from 1-minute data resolution to 30 min data resolution for both oCRM. The coverage rate p , observation interval k , and the production level resolution are $p = 90\%$, $k = 60$ min and 0.01 p.u., respectively.

distribution in the sCRM, this problem can be solved by minimizing the effect of these 2% bad points in the likelihood function. During the parameter estimation, the bias caused by the bad points will be flooded by correct data. Shown in Figure 4.10, the performance of oCRM and sCRM under 2% noise

sCRM Estimation

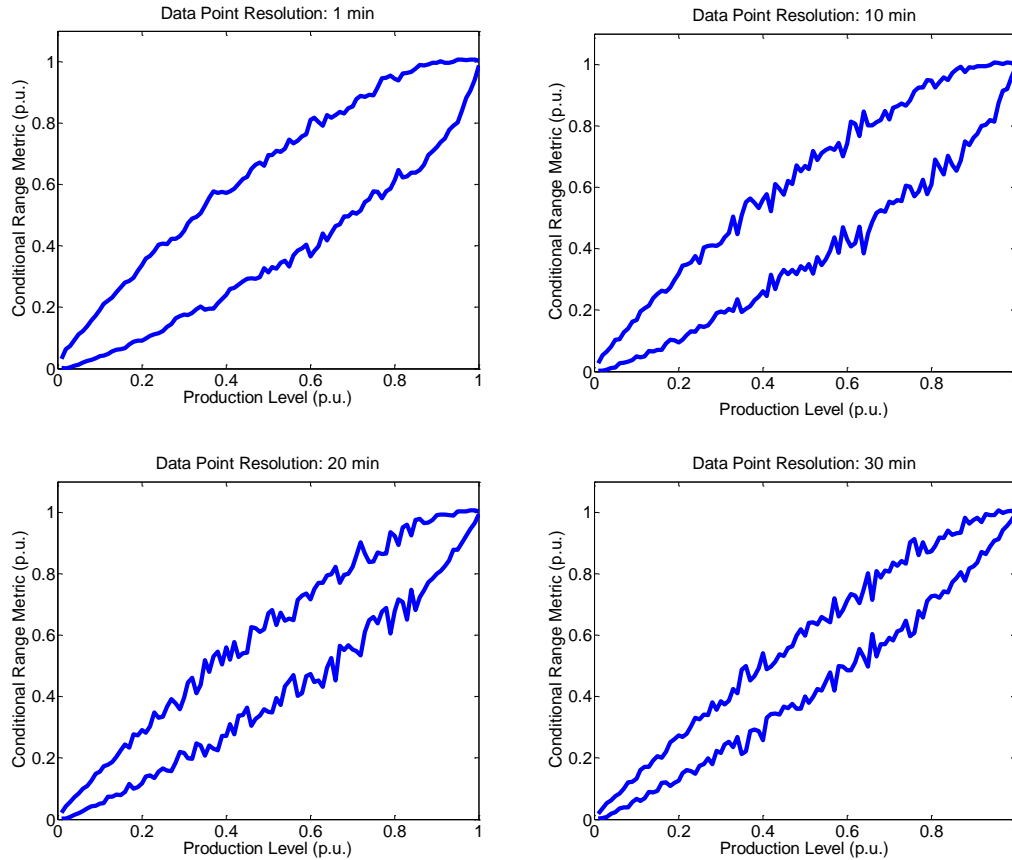


Figure 4.9: The conditional range is plotted from 1-minute data resolution to 30 min data resolution for both sCRM. The coverage rate p , observation interval k , and the production level resolution are $p = 90\%$, $k = 60$ min and 0.01 p.u., respectively.

points are compared. Bad data are generated as random values from a uniform distribution ranging from zero up to the maximum value in the upper or lower deviation series. These points are then interpolated into random positions, which are also sampled from a uniform distribution from zero to the size of

the data throughout the entire series to replace the original values, resulting in a 4% replacement in the total volume at each production level. With a 98% coverage rate, it is obvious that the conditional range estimation in (4.4) from oCRM has been completely impaired. Although the sCRM is affected, it is merely a constant offset, which can be easily fixed by a correction factor CF .

The calculation of CF is accomplished by taking the mean value of the gaps between conditional range estimations from the normal and noisy data across the production level from 0 p.u. to 1 p.u. Further, the relationship for CF and the noise data percentage is researched and depicted in Figure 4.11 regarding the coverage rates above 90%.

A lookup table can be established to compensate the impact of noise points for actual applications. If the accuracy requirement is not rigorous, this correction factor can be considered linear in respect to the percentage of the noise points as follows:

$$CF = LC \cdot Pct \quad (4.29)$$

where Pct is the percentage of the noise points in the upper or lower deviation series. LC is the linear coefficient realized as the averaged slope of the lines in Figure 4.11. For example, LC is approximately equal to $LC = 0.0423$ under a coverage rate of $p = 98\%$. More values of LC at different coverage rates are available in Table 4.2.

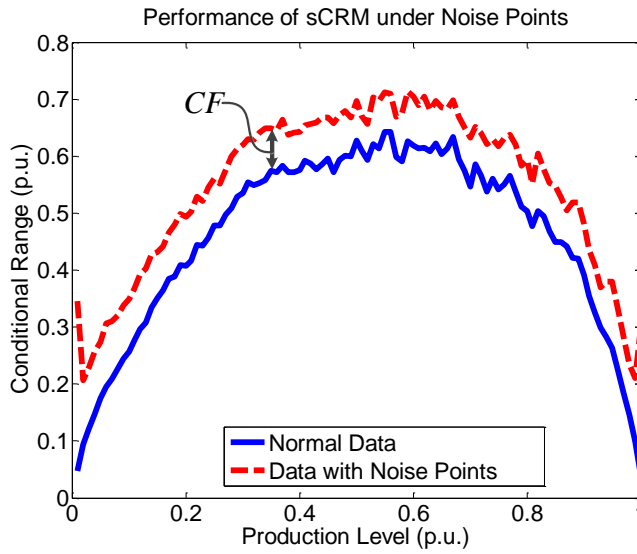
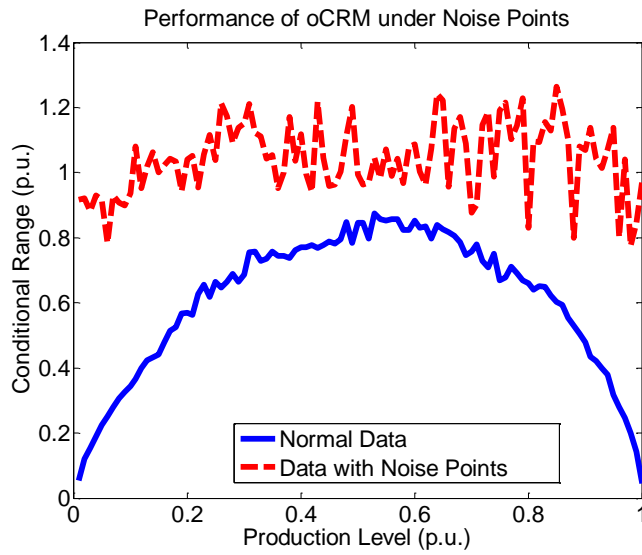


Figure 4.10: Conditional range comparison of oCRM and sCRM under 2% noise points in the upper and lower deviation series with a coverage rate of 98% and an observation interval $k = 60$ min.

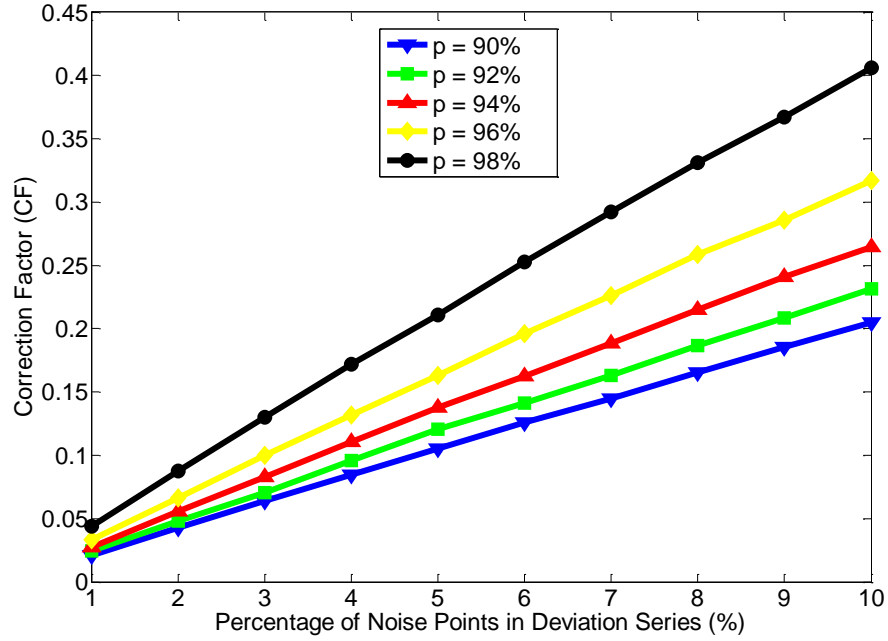


Figure 4.11: Correction factor under different percentages of noise points with coverage rates $p = 90\%$, 92% , 94% , 96% , 98% .

Coverage rate p	90%	92%	94%	96%	98%
LC	0.0209	0.0236	0.0272	0.0326	0.0423

4.5 Summary

The CRM is effective for quantifying the wind power variability during an intra-hour time span. However, the probability model can be improved and the joint probability matrix can be reduced to improve the adaptability and computational efficiency of this methodology. By employing gamma distributions, the probability model for the power-deviation series has been redesigned

with parameters estimated by MLE. Proved by Bayesian inference, the gamma distribution and parameter estimations are valid for the data. Comparisons by performing the oCRM and sCRM on down-sampled power data and noise points in deviation series denote a better performance.

Chapter 5

Evaluation of Quasi-Dynamic Wind Turbine Model and sCRM

Variable generation sources, wind power in particular, require new approaches in system planning and operation practices. Proper solutions shall be proposed to help ameliorate the impacts and imbalances of wind power variations imposed on the power grid. The development of reduced-order wind turbine models and methods of quantifying intra-hour power variability have been largely completed. The importance of simulating wind farms using individual wind turbine models has been illustrated in Chapter 3. Long-term simulations can be performed using quasi-dynamic model to generate wind power time-series from the wind speed dataset introduced in [1]. One desired purpose is to better understand the characteristics of wind farms in order to properly propose the control and power dispatch schemes. Quantified by the sCRM introduced in Chapter 4, the variability of the simulated power can be studied. Based on the results and analysis in this chapter, detailed design for reducing wind power variability will be proposed in Chapter 6.

In addition, the simulated power from multiple wind turbines is generalized into generation scenarios using an unsupervised machine learning algo-

rithm. In respect to the correlation, 10,000 data points are clustered into 10, 50, and 100 scenarios with their respective discrete probabilities.

5.1 Introduction and Literature Study

As an initial trial and study basis, the wind farm will be simulated together with a generation source for variability mitigation. Starting with a single wind turbine, 0.35-p.u. and 0.65-p.u. power sources are attached to the AC side of the quasi-dynamic model, respectively. Using an averaged power profile from historical data, the power source would counteract the power variations by adjusting its generation to meet the imbalances caused by the varying wind speed. A power generation baseline will be set, therefore, the power source will treat the wind turbine as a load and increase its output when the wind power is below the baseline, while decreasing the output when the wind power is larger than the baseline. To simulate the wind farm in a long-term operation scenarios for data collection, efforts have been attempted in literature. The modeling applied for such purposes falls into three categories: data-based simulation, differential-equation-based simulation and hybrid simulation.

- Data-based simulation relies on the computation of time-series data without considering the interaction between components in an energy system. Performing the data analysis can be time-efficient to derive and evaluate certain designs with the least system information. To be specific, the time-series data-based simulation are frequently employed for sizing

energy storage system or energy sources due to the difficulties and inaccuracies of modeling such systems. Design optimization can also be approached by resorting to methods of processing time-series. By minimizing a cost function defined to describe the error between the desired value and current value, optimal parameters of an electrical system are able to be determined. Designs and power management schemes can be efficiently evaluated by data processing up to years, which is statistically preferable. Reference [65] and [66] have presented such methods of sizing energy storage systems (ESS) for thermal power systems and micro-grids, respectively. The ESS is also sized for regenerative braking in electric railway system with time-series fashion in [67]. Other similar research regarding implementation of renewable energy sources is proposed in [68–72]

- Emphasizing dynamics and accuracy, differential-equation-based simulations implement models in reduced order to improve the computational efficiency. Therefore, the simulated duration can be from dozens of seconds up to hours. Such modeling typically includes the torque-speed features of the generator, electro-mechanical transient and current-voltage response of the grid [73–77]. Controller design, power flow regulation and system fault analysis are accessible from this perspective. In [73–75], dynamic power management regarding cooperation between wind power and ESSs has been described. Literature [76] and [77] propose dynamical modeling and integration of super-capacitor ESS into the wind farm

system for demand regulations.

- To compromise the pros and cons between data-based simulations and differential-equation-based simulations, the hybrid simulation assumes that some parts of the model are in a time-series form with minimum amount of differential equation. For example, the control signal can be pre-calculated or pre-evaluated into scenarios and used as known inputs or mapping functions, while other system components are represented by reduced order differential equations. Those simulation realizations have been implemented in [78–82].

In this chapter, simulations are performed based on the hybrid simulation concept. The system is developed from the quasi-dynamic wind turbine model, yet, power control and regulation schemes are not calculated in real-time. Rather, they are implemented using the historical power data and have already been computed off-line. These power control and regulation commands for the reserved generation source will be stored in a text file and read by PSCADTM.

5.2 Wind Turbine Level Simulation

On a single wind turbine level, wind power variability will be assessed by running reduced-order models using long-term wind speed time-series. The diagram with a wind turbine and a generation source is illustrated in Figure 5.1. Appearing in the yellow block in Figure 5.1, wind speed datasets are

obtained from ID 12 (31.28°N, 104.52°W) in the NREL database [1] that is the same source of wind speed data used for the validation process in Section 4.4. Paralleled with the wind turbine, an generation source is connected at the point of interconnection (POI), supporting active power to compensate wind power fluctuation.

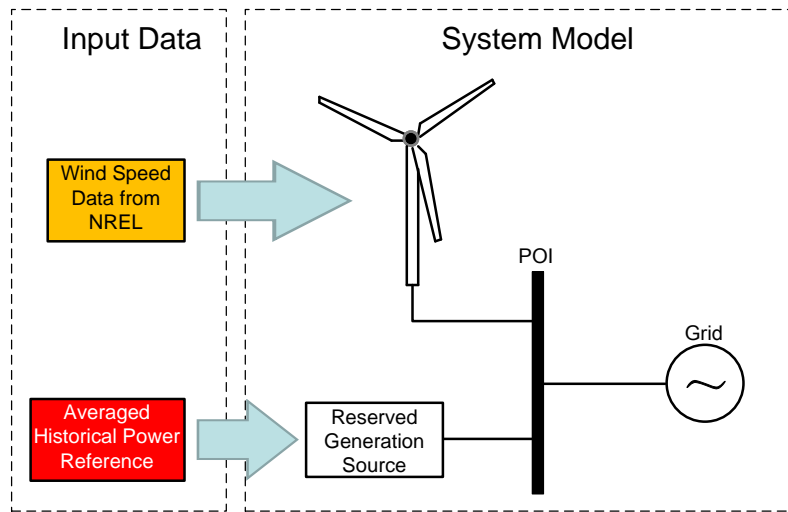


Figure 5.1: Reducing and managing wind power variability on a wind turbine level

The research for the generation source commences with characterizing its interactions with the wind turbine in reducing power variations. Power ratings of 0.35 p.u. and 0.65 p.u. are chosen as initial trials, assuming an unlimited energy capacity. After the data from monthly operations has been collected, the required operational capacity can be estimated using the amount of total throughput energy provided by the source. This idea is further developed into a method for sizing energy storage systems in Chapter 6. Probabilistic coverage can, thus, be developed to quantify the power dispatch behaviors

regarding the effectiveness of power variability reduction. Controls, at this stage, can use the hourly averaged historical power data in the past. Averaged power from the past 1 hour, 3 hours, 6 hours, 9 hours, and 12 hours is realized as production levels, directing the generation source to cooperate with the quasi-dynamic model accordingly.

To compare the power variability in a more straightforward representation rather than to discriminate between the CRM graphs, the conditional range over all production levels needs to be averaged for its statistic expectation such that the comparison will be performed between simple numbers, which denote power variations. From the historical data, the probability of appearance w_{l_j} can summarize the conditional range $CR_{k,l_j,p}$. w_{l_j} is calculated by taking the probability summation of where the output power lies in the desired production level:

$$w_{l_j} = \sum P(X_n \in l_j). \quad (5.1)$$

The averaged conditional range $CR_{avg,k,p}$ is, thereby, derived as the expectation of $CR_{k,l_j,p}$ over the entire domain of l_j as follows:

$$CR_{avg,k,p} = \sum_{l_j=0}^1 w_{l_j} \cdot CR_{k,l_j,p}. \quad (5.2)$$

Quantified by the averaged conditional range, the 0.35-p.u. and 0.65-p.u. generation sources are simulated by the quasi-dynamic wind turbine model using wind speed dataset from January 2004. Five monthly power

output data regarding the aforementioned averaging length from the wind power and the generation source is generated, whose variability is listed in Table 5.1 with a coverage rate of $p = 95\%$ and observation interval $k = 60$ min.

Table 5.1: Averaged CR from a 95% Coverage Rate

Averaged CR without Generation Source		
0.1999 p.u.		
Averaged CR with Generation Source		
	0.35-p.u. Source	0.65-p.u. Source
1-hour Averaged Reference	0.1664 p.u.	0.1647 p.u.
3-hour Averaged Reference	0.1317 p.u.	0.1215 p.u.
6-hour Averaged Reference	0.1280 p.u.	0.0969 p.u.
9-hour Averaged Reference	0.1335 p.u.	0.0931 p.u.
12-hour Averaged Reference	0.1360 p.u.	0.0918 p.u.

The conditional range metric (CRM) through the entire production level is displayed in Figure 5.2 for both 0.35-p.u. and 0.65-p.u. sources. The narrower CRM denotes an more effective statistical reduction on intra-hour power variations.

Impacts from different control references in terms of various averaged hours are summarized in Figure 5.3. Below a certain threshold, extending the length of the averaged hours can reduce CR. The variability, however, will increase in a prolonged averaging length, even with an ideal assumption on power ramping time. The increased variability using longer length of averaged

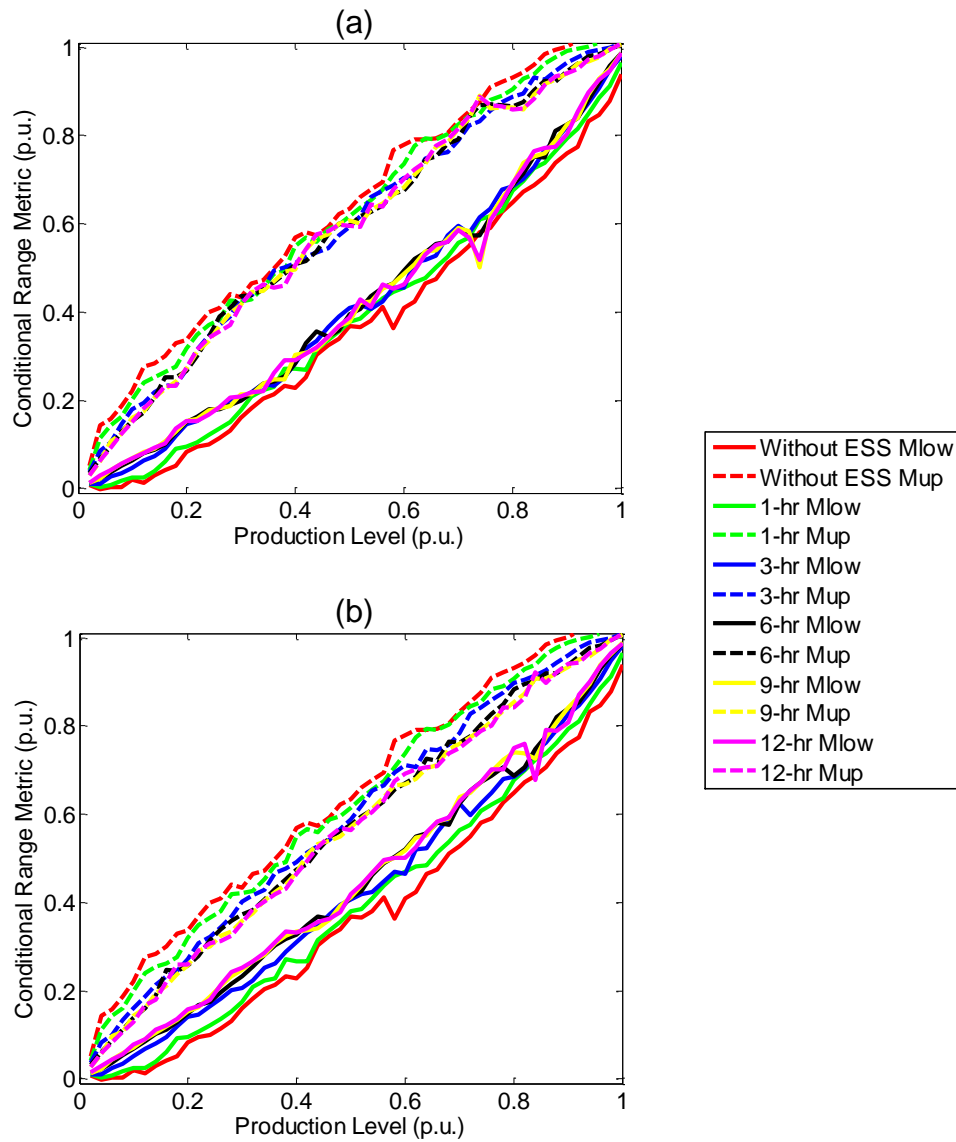


Figure 5.2: Conditional range metric estimations using 0.35-p.u. and 0.65-p.u. generation sources with $p = 95\%$ and $k = 60$ min

hours is caused by the incapability of following short-term wind power variations, other words, the power demand from the dispatch scheme is beyond

the maximum power support from the generation source. The 0.35-p.u. generation source reaches its best result by averaging the power time-series in the past 6 hours, while the 0.65-p.u. generation source will not be optimized until the past 12-hour data has been applied. Note that the reduction of power variations is nonlinear to the length of averaged hours and becomes less effective when it is towards the best results. Generation sources with a fast response, such as power-electronics based interfaces, can apply a shorter length of averaged hours for tracking and compensating short-term wind power variations, which appear to fluctuate in a more random and drastic pattern. The details on controlling short-term imbalances and providing long-term power support will be analyzed in Chapter 6.

By considering ideal generation sources, power variability reductions related to source power ratings are revealed. In the real-world, it is impractical, however, to integrate large capacity generation sources that specifically cooperate with the wind farm for mitigating variability. The wear-and-tear problems on conventional generation sources do not allow a fast-response power adjustment under a high power changing rate. Because the generation source can be considered as an ESS with an infinite energy capacity, its cooperation with the wind farm can be analyzed for determining the ESS energy capacities. Methods for sizing the ESS will be investigated via power dispatch patterns acquired from simulation. Researching and analyzing the output power from the generation source can seek for a reasonable method to quantify the source utilization via probabilistic distributions and statistical approaches.

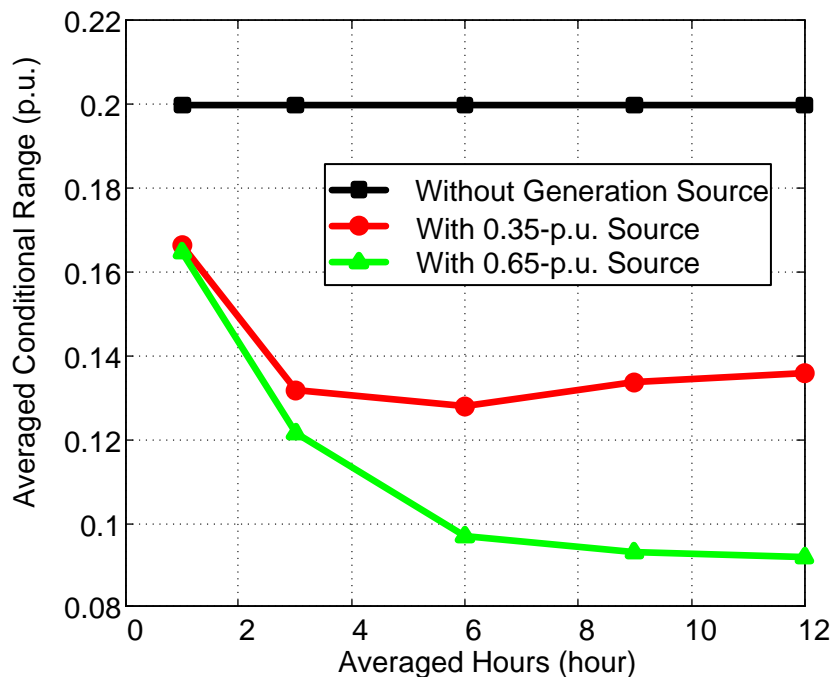


Figure 5.3: Averaged conditional range in respect to generation source rating and length of averaged hours with $p = 95\%$ and $k = 60$ min

Further, in terms of response time, different types of ESSs will interact with the wind power in different manners. For instance, a hydro-based interface with response time in minutes is less effective for compensating violent power fluctuations in short-term, yet, it can contribute as a more steady energy supply during long-term operations. The generation response time regarding various technologies can be characterized to optimize the power variability management. For example, it is possible to implement a combined energy system with different technologies, taking both advantages of mitigating short-term imbalances and providing sustained power to meet the load

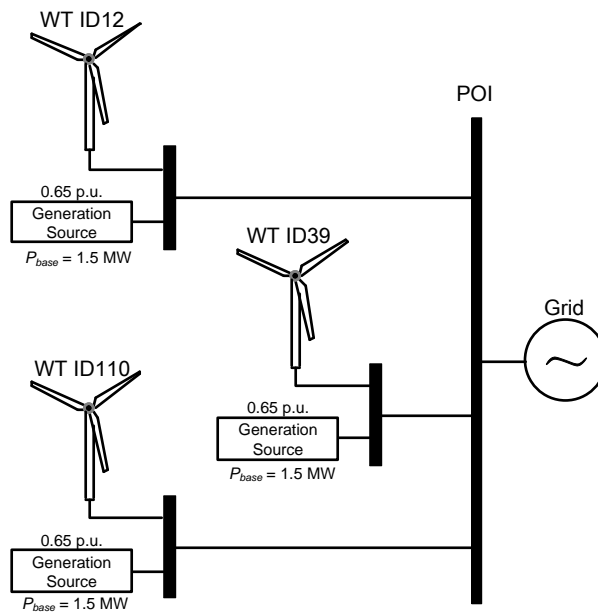
demand.

5.3 Wind Farm Level Simulation

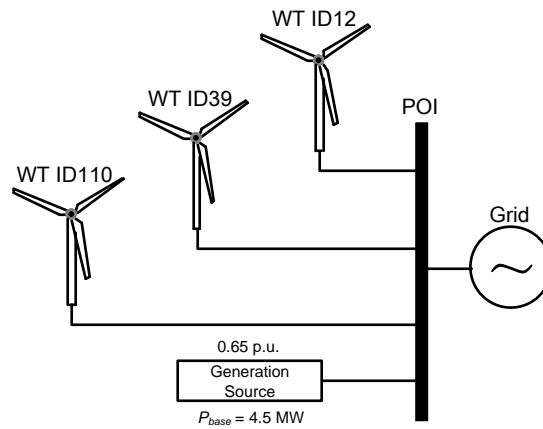
5.3.1 Simulation of Small Wind Farms and Reserved Generation Sources

To evaluate the operational characteristics of a wind farm, simulations are performed to reduce wind power variability using two system layouts illustrated in Figure 5.4: distributed energy source and centralized energy source. A small wind farm is set up using three individual quasi-dynamic wind turbines to study the cooperative controls for operating the 0.65-p.u. generations source. In Figure 5.4, the total power ratings for two configurations are the same. For the distributed configuration, small generation sources such as micro-turbine or fuel cells that can be spread over the wind farm, coordinating with the wind turbines based on their respective power profiles, while the centralized ESS targets for cooperating with wind farms using a control reference from the aggregated power output, ignoring individual wind turbine behaviors. Wind speed dataset during January 2004 are drawn from [1] at ID 12 (31.28°N, 104.52°W), ID 39 (31.46°N, 104.61°W) and ID 110 (31.68°N, 104.72°W). These three locations are 15.5 miles apart (from south to north), representing a regional-spreaded geographical dispersion.

According to stochastic process, as the wind farms grow larger, the power variation should exhibit a smoother profile via aggregation. This has been validated by running the wind farm without the generation source in



(a) Distributed Generation



(b) Centralized Generation

Figure 5.4: Two configurations for operating generation sources. The total power ratings are the same for both layouts.

Figure 5.4. Power time-series for each wind turbine and the wind farm are analyzed by the averaged conditional range, derived from $p = 95\%$ and $k = 60$ min in Table 5.2. The conditional range through the entire production level has been plotted in Figure 5.5. By aggregating the power from three wind turbines, the averaged CR has been reduced by roughly 26.7%. If the locations of the three wind turbines are farther from each other, the power variability of the wind farm could be even lower. This is because the wind speeds between different locations are less correlated in a widespread area, leading to a randomness on turbine-side output. Although the absolute power variations of a wind farm is larger than single wind turbines, the variability in per-unit experiences a decreased value reflected both in Table 5.2 and Figure 5.5. In Figure 5.5, not only is the per-unitized conditional range magnitude of the wind farm smaller than that of single wind turbines, but also the curve is smoother.

Table 5.2: Averaged CR from Simulated Wind Farm without Reserved Generation Source

	Averaged CR
Wind Farm	0.1502 p.u.
Wind Turbine ID 12	0.1960 p.u.
Wind Turbine ID 39	0.1930 p.u.
Wind Turbine ID 110	0.1933 p.u.

Simulated in PSCADTM environment, the generation data from the two source layouts is performed into CRMs in Figure 5.6. With the averaged

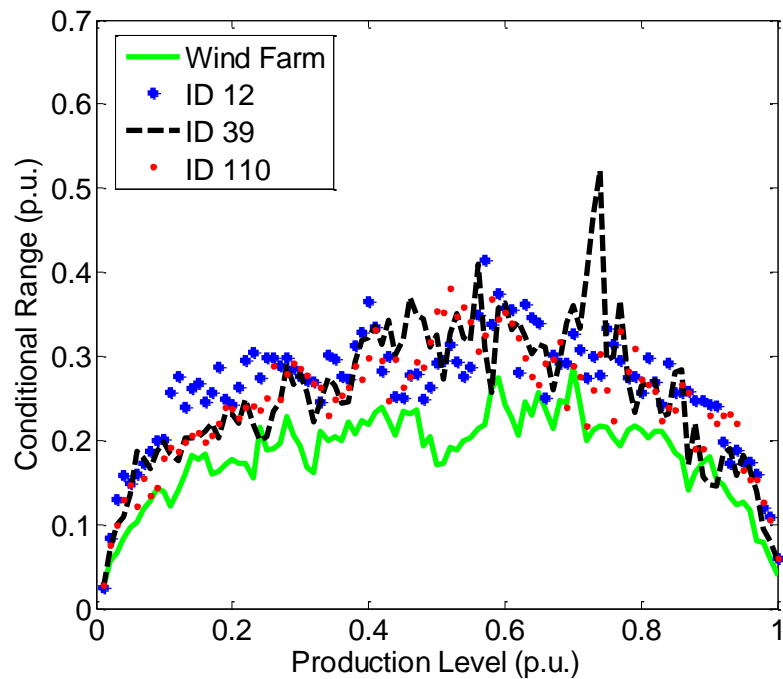


Figure 5.5: Conditional range estimation for single wind turbines and wind farm with $p = 95\%$ and $k = 60$ min.

conditional range summarized in Table 5.3, the centralized generation source appears to have a better control of the power variability. This explains the less power variation from a wind farm than that from a single wind turbine as analyzed in Table 5.2, which gives a smoother control reference to the generation source. If the implemented source possesses a slower respond time, the advantage of employing a centralized generation source such as hydro power station is even more preferable.

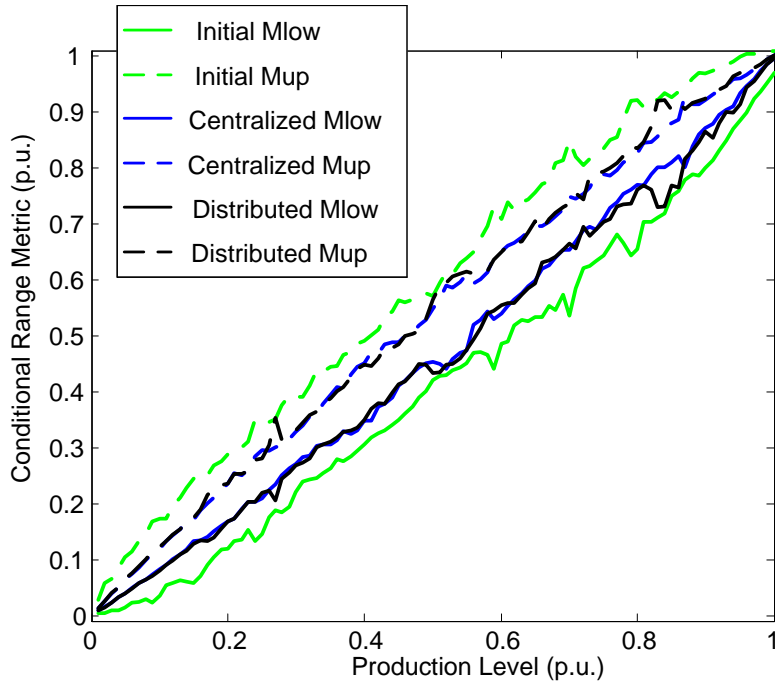


Figure 5.6: Conditional range using distributed and centralized generation sources with $p = 95\%$ and $k = 60$ min.

Table 5.3: Averaged CR from Distributed and Centralized Generation Sources

	Averaged CR
Without Generation Source	0.1502 p.u.
Distributed Layout	0.0747 p.u.
Centralized Layout	0.0720 p.u.

5.3.2 Analysis of Correlation

For wind farm analysis, a statistical measurement is sample correlation coefficient which describes the correlation between two series $X(k)$ and $Y(k)$ [83].

$$\rho_{X,Y} = \frac{\sum_k (X(k) - \bar{X})(Y(k) - \bar{Y})}{\sqrt{\sum_k (X(k) - \bar{X})^2 \sum_k (Y(k) - \bar{Y})^2}} \quad (5.3)$$

where \bar{X} and \bar{Y} denote the sample mean values in series $X(k)$ and $Y(k)$. The positive and negative correlated data will feature correlation coefficients 1 and -1, respectively. A zero value corresponds to two completely independent datasets. The correlation analysis is used to determine power generation independence between different locations.

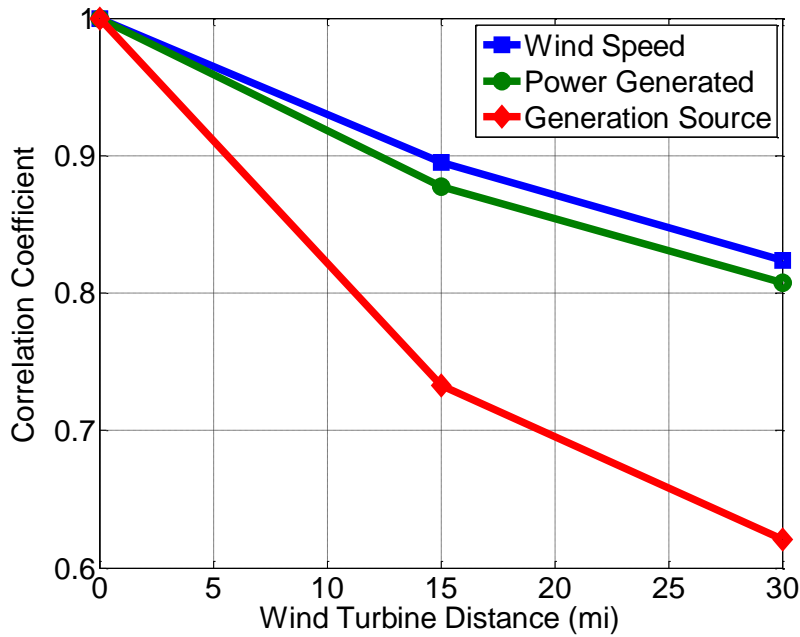


Figure 5.7: Correlation coefficients calculated from wind speed, power generated by quasi-dynamic model and reserved generation source

Using the simulation data acquired from the distributed generation source configuration in Figure 5.4 (a), wind speed, raw wind power and gener-

ation sources can be further analyzed by correlation coefficient defined in (5.3). Demonstrated in Figure 5.7, the correlation reduces as the distance increases due to the geographical discrepancies of the wind power source. Taking the wind turbine ID 12 as the origin, the wind speed correlation decreases almost linearly regarding the distance from ID 12 to ID 39 and ID 110. The correlation of power follows the trends of the wind speed, but, decreases slightly faster due to the dynamical response to wind speed changes. The correlation of different generation sources plummets compared to those of wind speed and power time-series. This is because the power dispatch of the reserved generation is determined by the averaged power from historical generation data, which breaks the correlation between adjacent wind sources by averaging. The decrease of correlation in generation sources also explains the better results from distributed layout due to the fact that the sources can work more independently.

Correlation matrix denoting the relevance between each two wind turbines are shown in Figure 5.8 for ID 12, ID 39 and ID 110. Compared to Figure 5.7, the detailed correlation coefficients are provided in numerical expressions.

Taking advantages of the correlated information, wind power generation can be generalized by taking generation data from all individual wind turbines to formulate generation scenarios [84, 85] in later sections.

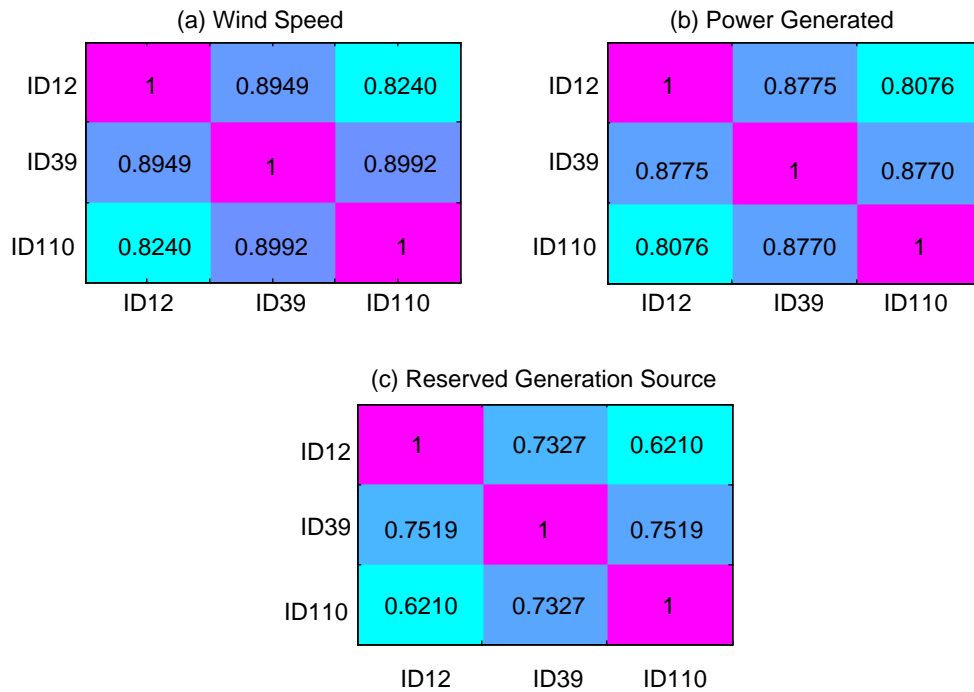


Figure 5.8: Correlation matrix among ID 12, ID 39 and ID 110

5.4 Scenario Generation of Wind Farms

To generalize generation scenarios of correlated wind turbines, unsupervised machine learning algorithms can be applied for clustering and dimensional reduction of the wind power data. Using the sampled power data, power uncertainty prediction can be derived by power density in a time-series fashion [86]. Discrete power data can also represent the wind power output in scenarios. Applying discrete distributions to those scenarios, wind farm behaviors can be predicted by the probability of falling into a specific generation level. Because of the vast volume of sampled time-series data, reductions are desirable to simplify the output patterns of wind farms [87–92]. In [87], sce-

nario reductions are performed on a single aggregated wind farm to combine the power-versus-time curves from 1000 scenarios down to 10 scenarios. Similarly, 3000 power profiles in a day-length frame have been represented by 3 generalized cases in [88]. Scenario-based models can be implemented to solve power management problems as well as sizing energy storage systems [89, 90]. These models are also applicable on power ramp event forecasting [91] and transmission expansion planning [92].

In order to develop generalized generation scenarios for correlated wind turbines in a regional wind farm, a unsupervised machine learning algorithm is employed to reduce the original 10,000 data samples down to 10, 50, and 100 scenarios by clustering the correlated sample points. The probability of the generation scenarios can, thus, be calculated from discrete probability distributions. An illustration of clustering 2000 generation samples from two wind turbines with geographical proximity is displayed in Figure 5.9. The raw power data is grouped by a K -means algorithm to identify underlying cluster patterns. Other clustering methods in [93] are, likewise, accessible. Shown by the orange bar chart, the five cluster centroids represent five correlated power output scenarios with respective probabilities from P_1 to P_5 .

In addition, using the generalized generation scenarios, the data dimension can be compressed by applying principal component analysis. For example, because the power samples in Figure 5.9 are correlated between wind turbine #1 and #2, the 2-D data can be projected onto a 1-D domain depending on their relevance. Strongly correlated data will perform better during

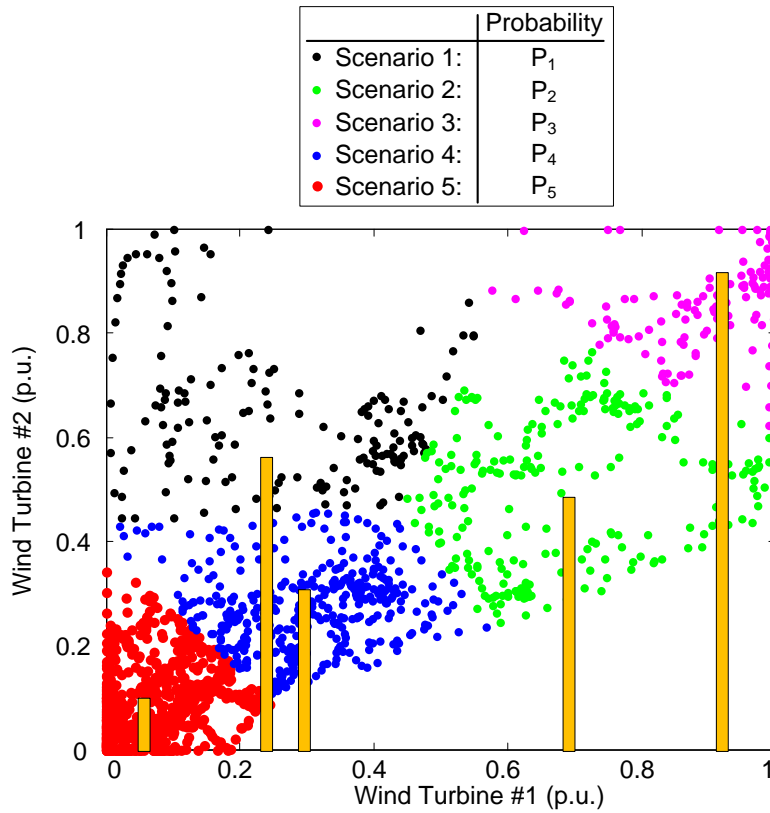


Figure 5.9: Illustration of clustering generation scenarios for two wind turbines. The original 2000 scenarios are generalized into 5 basic patterns.

dimensional reduction of data features. Thus, the regional wind farm can be represented by power data in a lower dimension with occurrence probabilities.

5.4.1 Unsupervised Machine Learning for Clustering Wind Power Generation Data

Unsupervised machine learning involves in finding hidden structures among unlabeled data. Because of the unlabeled attribute, there is no error terms in evaluating a potential solution, which differs from the supervised

learning. The optimized solution, accordingly, will be obtained by minimizing its cost function regarding all data points. In this work, the unlabeled power time-series from correlated wind turbines are processed by unsupervised learning methods to detect potential generalized patterns as generation scenarios.

5.4.1.1 *K*-Means Clustering Algorithm

K-means clustering, proposed by MacQueen in 1967 [94], is a method commonly used to automatically partition a dataset into *K* groups. It is, by far, the most popular and widely used algorithm in clustering raw data, such as social network grouping, computer vision pattern recognition, or business market segmentation, etc [95]. *K*-means method employs *K* prototypes which serves as centroids of the data clusters for characterizing the raw data. Then, each data point x_i in the dataset x_1, x_2, \dots, x_n is assigned to the nearest centroid. Consequently, the input data can be clustered into *K* disjoint subsets for generalization. The optimization objective is to minimize the cost function defined by Euclidean distance between each data point x_i and its corresponding cluster centroid μ_k [96–98]:

$$J(\mu_1, \mu_2, \dots, \mu_K) = \sum_{k=1}^K \sum_{i \in C_k} \|x_i - \mu_k\|^2 \quad (5.4)$$

where C_k is the cluster that x_i belongs to. The process of finding the clusters is to iterate through all data points, assigning them to the closest centroid to form new clusters, and finally updating the cluster centroid by averaging all members in the new clusters. The iteration will stop until the cost function

converge to its minimal value. The following pseudo-code summarizes the operations in each iteration.

Repeat { for i from 1 to n :

Find the closest centroid μ_k for data point x_i
and assign x_i to its respective cluster C_k by
setting the index array of each data $idx(i) = k$.

for k from 1 to K :

Average all elements in C_k using the index
array idx to locate the data points and update
the new centroid μ_k to the mean value calcul-
ated above.

Calculate the cost function $J(\mu_1, \dots, \mu_k)$ and
compare its value with the last iteration for
convergency. }

The graphic illustration of K -means clustering is displayed in Figure 5.10 after seven iterations. The centroids have moved from their initial values to the cluster center, therefore, the data samples can be correctly grouped to their corresponding cluster from the final updated centroids.

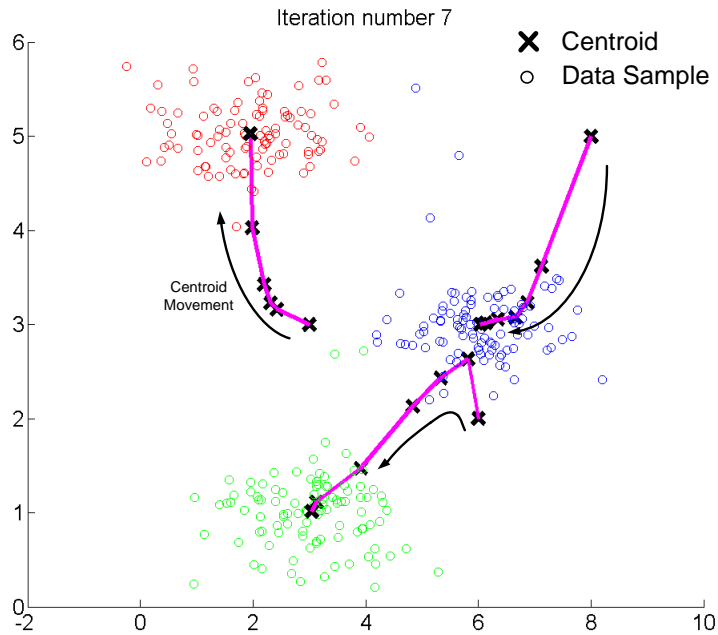


Figure 5.10: An example of clustering data using K -means algorithm.

5.4.1.2 Random Initialization of K -Means Algorithm

Theoretically, the initialization of centroids should not impact the optimization solution using iteration. Yet, due to complicated data dispersion, some centroids can fall into local optima rather than the global minimum. Studies focusing on improving the algorithm to avoid the local optima have been conducted in [99, 100]. In this work, a simple random initialization is applied. Data samples are selected randomly from the raw dataset and assigned as the initial values for the centroids. Then, the K -means method can be executed multiple times with different randomized centroids to find the clustering solution which possesses the smallest value of $J(\mu_1, \dots, \mu_K)$. The random initialization is computationally expensive if the dataset is large. But,

it is adaptive and robust for most study cases and performs statistically even better when the number of clusters are excessive compared to the total data volume.

5.4.2 Principal Component Analysis

To further generalize the generation scenarios by combining correlated wind turbine outputs, principal component analysis (PCA) is implemented to reduce the dimension of featured data [101–103]. PCA is an analytical procedure that uses an orthogonal transformation in which the reduced features will be projected onto the remained features. This method is widely employed by image and audio compression algorithms. In this study, features are defined as different wind turbines whereas the data is power generated in time-series. Figure 5.11 shows a dimensional reduction of wind power data using PCA. By projecting the 2-D data (blue samples) onto a 1-D domain (red samples), the generation scenarios can be reduced by 50%. It should be noted that PCA is only valid for correlated datasets. Its performance will deteriorate if the two data sources are independent or weakly correlated.

The calculation of PCA starts with formulating a covariance matrix from the dataset x_1, x_2, \dots, x_n with m features. Since x_1, x_2, \dots, x_n are derived from power time-series, its features represent m correlated wind turbines in a regional wind farm. The covariance matrix is defined as:

$$M_{m \times m} = \frac{1}{n} \sum_{i=1}^m (x^{(i)})(x^{(i)})^T \quad (5.5)$$

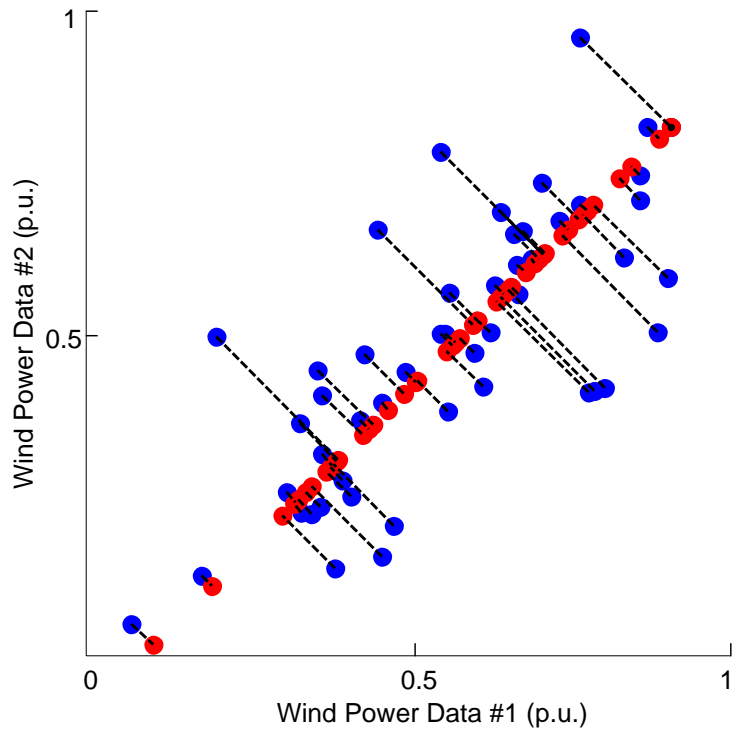


Figure 5.11: Projecting 2-D wind power data onto a 1-D domain. The two data sources must be correlated.

Because the feature and correlation information are included in covariance matrix, singular value decomposition of M performs orthogonal transformation among features:

$$U_{m \times m} \Sigma V^* = \text{svd}(M) \tag{5.6}$$

The column vectors in matrix U denote projected features and thereby can be used for dimensional reduction. If the generation data is desired to be in R dimension, a reduction matrix U_{reduce} is formed by taking the first

R columns from U . Finally, the following equation computes the generation scenarios in a reduced dimension:

$$z_{R \times 1}^{(i)} = U_{reduce}^T x^{(i)} \quad (5.7)$$

Depending on the level of correlation between sampled power data, the final dimension R should be properly selected to avoid excessive data compression [104]. Therefore, a measurement is defined as retained variance to describe how much information of the data has been left:

$$Var_{retained} = \frac{\sum_{i=1}^n \|x^{(i)} - z^{(i)}\|^2}{\sum_{i=1}^n \|x^{(i)}\|^2} \quad (5.8)$$

Due to the computational complexity of (5.8), an alternative method for calculating retained variance is to sum up elements in the diagonal matrix Σ from singular value decomposition in (5.6). The following equation is thus developed to characterize the data compression:

$$Var_{retained} = 1 - \frac{\sum_{i=1}^R s_{ii}}{\sum_{i=1}^m s_{ii}}, \quad s_{ii} \in \Sigma \quad (5.9)$$

5.4.3 Generalizing Wind Power Generation Scenarios

To evaluate the proposed method for generation scenario generalization, wind power datasets are loaded from simulations in Section 5.3 at ID

12, ID 39 and ID 110. The simulation results in 1-minute resolution are down sampled to a 10-minute density to increase the total length of analyzed data for 10,000 sampled points. This operation will not cause variations in correlation due to the time-series properties. The 3-D power samples are shown in Figure 5.12. These data will, later, be clustered into 10, 50, and 100 scenarios by K -means algorithms. There are total 10,000 generation samples as initial scenarios, therefore, each data sample represents an occurrence probability of 0.01%.

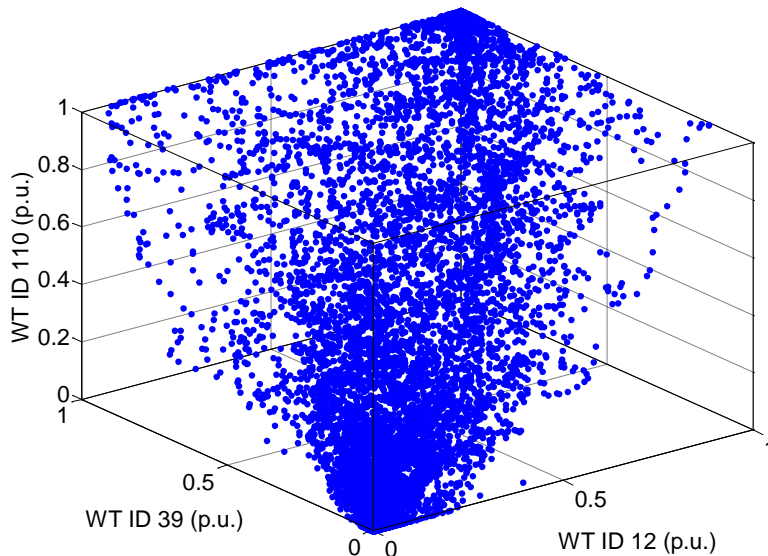


Figure 5.12: Wind power data samples to be generalized.

As mentioned in Section 5.4.1.1, clustering wind power generation scenarios is only valid when the power from individual wind turbines has correlation. It is not representative to generalize independent wind power generation data due to the unordered power output pattern. Completely independent and

random distributed wind power data will disperse evenly in the linear space and cannot be grouped uniquely by clustering algorithms. A smaller correlation coefficient will induce a larger cost calculated by (5.4), thereby, resulting in weakly clustered scenarios. In this case, the solution might not be unique even using randomized initializations for centroids. Because the power from wind turbine ID 12, ID 39 and ID 110 is highly correlated according to Figure 5.8, it is viable to generalize their power generation scenarios using clustering algorithms.

Figure 5.13 demonstrates the generalized wind power generations for 10, 50, and 100 scenarios with their respective discrete probability distribution from data occurrence. The minimum costs computed by (5.4) are displayed in Table 5.4. The 10-scenario generalization suffers from a high bias for the learning samples, which means the model does not represent the enough variance of the data. More scenarios can minimize the cost, however, they will fail to generalize wind farm generation due to over-fitting of the data. For example, although it obtains the minimum cost of 50.93, the 100-scenario generalization ends up with only 97 valid clusters including one cluster at point (0, 0, 0) and another two empty clusters. The shrinkage in valid clusters shows that the maximum possible scenarios for this dataset are no more than 100. In this case, increasing the cluster volume K cannot further reduce the cost and will not perform a better data fitting.

Using PCA, the generation scenarios in 3-D can be reduced down to 1-D, representing the regional wind farm by single wind turbine. In this study,

Table 5.4: Minimum Cost, Valid Clusters and Retained Variance for Generalized Scenarios

Scenarios	Minimum Cost	Valid Clusters	Retained Variance
10	258.65	10	97.5%
50	80.51	50	75.4%
100	50.93	97	75.9%

the power from WT ID 39 and WT ID 110 is projected onto WT ID 12 for illustration. The retained variances for different number of scenarios are also listed in Table 5.4. The 10-scenario generalization acquires a retained variance of 97.5%, indicating that the total generation information stored in the 3-D data remains up to 97.5%. This is because after clustering, most of the correlation between scenarios has been maintained. Serving as generalized generation cases of the wind farm, the power output and probability of the 10-scenario generalization are shown in Table 5.5. This power output stands for the power from WT ID 12 while taking the operational information from other two wind turbines into account. The comparisons of projected power using PCA and actual power from aggregation are shown in Figure 5.14. Due to the size of the test wind farms is small, power from PCA matches the actual power well. Inconsistence will occur as the wind farm grows larger in which wind turbines are not closely correlated. Differing from simple power aggregation, dimensional reduction by PCA is found convenient for studies which take power from one wind turbine while still needing to consider correlated interactions from other wind turbines.

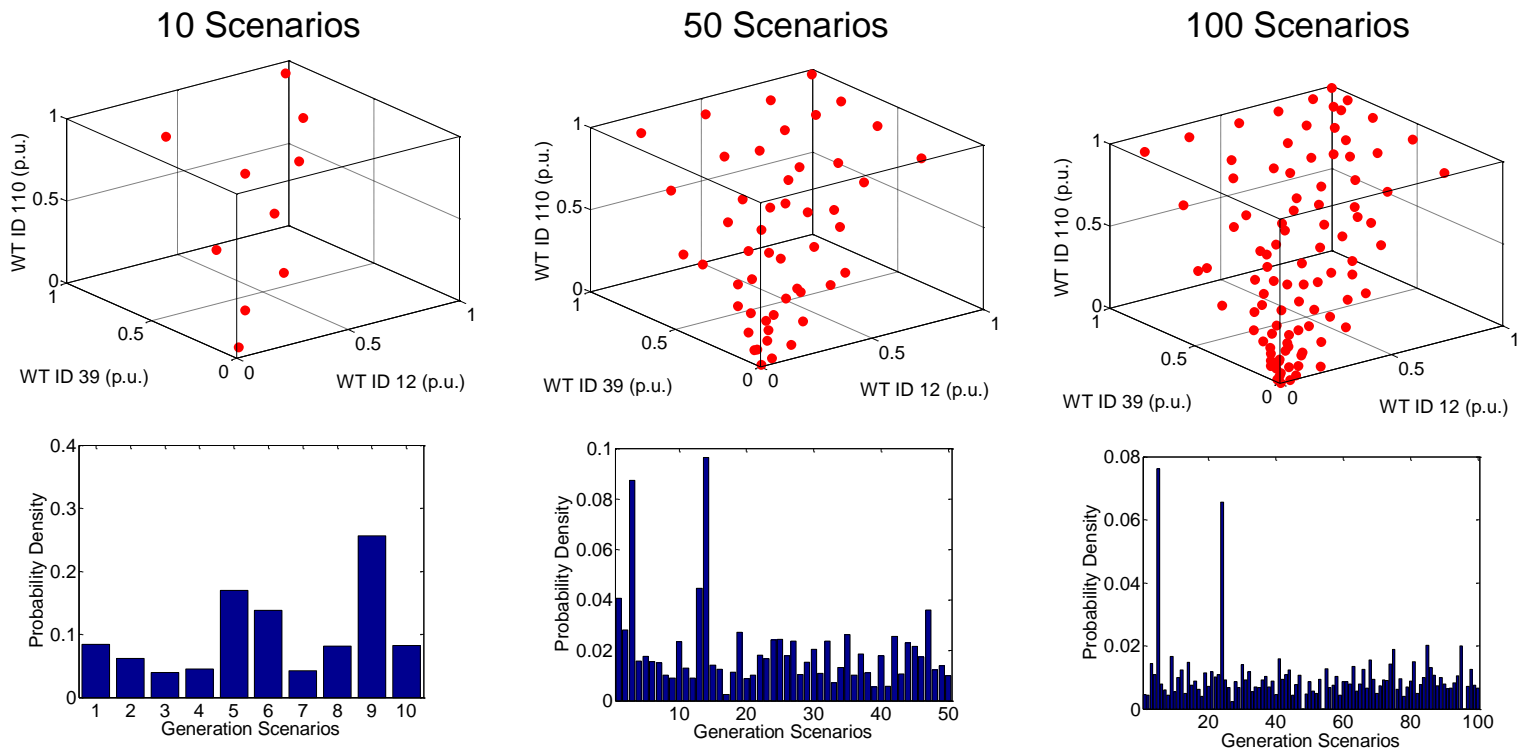


Figure 5.13: Generalizing wind power generation into 10, 50, and 100 scenarios with their respective occurrence probability.

Table 5.5: 10-Scenario Power Outputs and Corresponding Probabilities after Performing PCA

# of Scenarios	Power Output (p.u.)*	Probability
1	0.978	8.41%
2	2.137	6.15%
3	2.044	3.92%
4	2.327	4.50%
5	0.479	16.96%
6	2.885	13.78%
7	1.570	4.22%
8	0.951	8.18%
9	0.113	25.62%
10	1.525	8.26%

*: The base power 1 p.u. stands for a single wind turbine

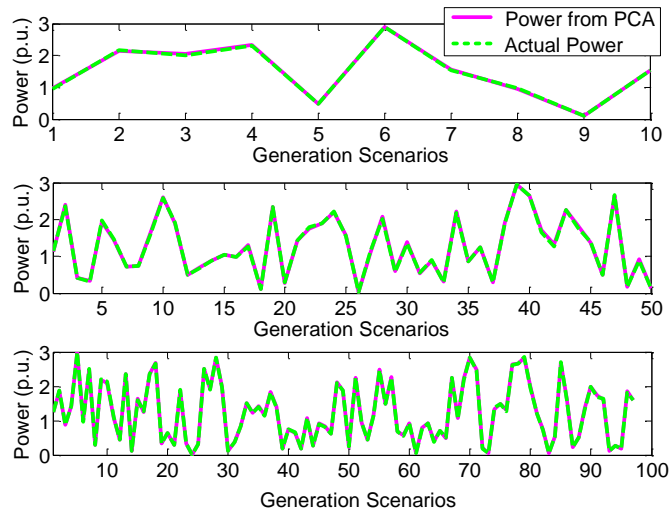


Figure 5.14: Comparison of reduced power dimension from PCA and actual power from aggregations.

5.5 Summary

In this section, the quasi-dynamic model has been evaluated by NREL wind speed data on both wind turbine and wind farm levels. Simulated power data is processed by CRM for variability analysis. To compensate the power variations, an ideal reserved generation source cooperates with the wind power to study the effectiveness. Further, power correlation among individual wind turbines has been investigated. By considering power time-series from individual wind turbines as data features, a K -means clustering method has been applied to summarize the raw power data into 10, 50, and 100 generation scenarios. Discrete distribution density can be calculated by fitting the data points into these scenario clusters. To further perform scenario compression, a PCA method projects the power from WT ID 39 and WT ID 110 onto WT ID 12. Therefore the 3-D generation scenarios have been reduced to a 1-D, probability-based power output to represent the behavior of the three wind turbines as a whole. In addition to dimensional reduction, retained variance of the raw data has been analyzed by summing up the elements in the diagonal matrix from PCA. The results show that a maximum of 97.5% of the data variance are remained during compressing the data from 3-D to 1-D.

Chapter 6

Sizing and Coordinating Fast- and Slow-Response Energy Storage Systems to Mitigate Wind Power Variations

Despite the merits of integrating renewable energy into the grid, power variability and uncertainty from wind power plants have grown into major issues for system operators. The increasing wind power penetration in the electric power grid heightens the applications of energy storage systems (ESS) to mitigate power variability. In West Texas, the Notrees Wind and Battery Storage Project has deployed a 36 MW/24 MWh ESS to respond to grid conditions from a nearby 153 MW wind farm interconnected with the Electric Reliability Council of Texas (ERCOT) power system [105]. A method of sizing the ESS to reduce wind power imbalances is demonstrated in [106] by minimizing deviation of actual wind power generation from its hourly average. In [4] and [107], the ESS is implemented to manage general energy imbalances among multiple power sources including the wind power. Similar designs through different control and operational methods could also be found in [108–112].

Unfortunately, ESSs that feature a fast response, such as battery- or super-capacitor-based ESSs with power electronic interfaces, are low on cost-

efficiency due to their initial infrastructure and capital expenses. These ESSs, also, are limited by their energy capacity to provide long-term power support. In addition, the ordinary battery-based fast-response ESSs suffer from lifetime depreciation affected by charge and discharge cycles from control strategies and power dispatch schemes [113–116]. For example, frequent power regulations with deep charge and discharge will cause the battery-based ESS service period to prematurely expire. Fortunately, to ameliorate the aforementioned issues, a slow-response ESS, such as a pump-hydro or compressed-air ESS, can be employed and coordinate with the fast-response ESS such that the total size of the fast- and slow-response ESSs will not be larger than using the fast-response ESS alone. The wear-and-tear problem of conventional generators used in such slow-response pump-hydro or compressed-air ESSs can also be improved [117, 118].

The objective of this section is to present a methodology for determining the fast-response ESS unit's power and energy ratings based on the sCRM [19] so that its operation can be coordinated with an existing slow-response ESS. Coordinating the fast- and slow-response ESSs is expected to reduce the variability of hourly wind power generation and maximize the life span of the fast-response unit. The methodology is demonstrated and applied to a 38-MW wind farm equipped with an 18-MW slow-response pump-hydro or compressed-air ESS that features a ramp rate of 600 kW/min.

Probabilistic-based sizing and computing methods are proposed. These methods are developed from the conditional range metric (CRM) described in

section 4. To control the ESSs, desired power profiles are determined from the persistence forecast [108,119] and power step-change (PSC) forecast. Next, two ESS configurations and power dispatch schemes for coordinating the fast- and slow-response ESSs are proposed. By simulating ESS operations on a 38-MW wind farm, applicability of the proposed methods is demonstrated. Two years of actual wind power time-series data is available for this work. Year 1 data is used to calculate ESS designed parameters, whereas Year 2 data validates the effectiveness and performance of ESS operations. Results from the coordinated power and energy dispatch schemes are evaluated in terms of the averaged conditional range (CR). Assessed by a rainflow-counting algorithm [106,120], lifetime depreciations of the fast-response ESS are compared among various ESS layouts and control strategies.

This chapter is arranged as follows: Section 6.1 presents preparatory wind power data and evaluation rubrics. Section 6.2 introduces a generic ESS model that includes both the fast- and slow-response ESSs. This section also presents the calculation of desired power profiles from forecasts for ESS control. In Section 6.3, optimal ESS sizing is detailed. ESS coordination and control methods for power dispatch are summarized in Section 6.4 . Finally, in Section 6.5, various control schemes are compared in terms of ESS operational independence, the effectiveness of power variability reduction, and fast-response ESS lifetime depreciation.

6.1 Wind Power Data and ESS Lifetime Evaluation

This section presents wind power source data and an algorithm to quantify the ESS's lifetime. Instead of using power data evaluated by NREL, real-world data from ERCOT is applied.

6.1.1 Wind Power Time Series

The analysis draws from two years of field-measured wind power data with 1-minute resolution from a 38-MW wind farm system. The generation data has maximum power at 37.95 MW and 38.04 MW in Year 1 and 2, respectively.

Although the data points have been reliably recorded, pre-processing them can eliminate spikes and interpolate missing points by linear interpolations. Additionally, negative power from the auxiliary equipment appears in the dataset when the wind speed is below cut-in level. The negative power has a peak absolute value of 510 kW, which weighs only 1.3% of the rated nameplate capacity. Because it does not represent any power variability caused by the wind energy, these negative points have been replaced by zeroes.

Wind power data in Year 1 is used to determine ESS ratings and control parameters, while the simulations use Year 2 data to evaluate the design's adaptability.

6.1.2 Battery Lifetime Assessment of the Fast-Response ESS

To evaluate the control and power dispatch schemes, it is necessary to understand the battery's lifetime consumption. As was addressed in [113] and [114], the charge/discharge cycles of chemical-based batteries, such as NaS or lead-acid types, can be significantly affected by the depth of discharge (DOD). In this work, the DOD is represented by the battery state of charge (SOC) modeled within the ESS:

$$DOD(t) = 1 - SOC(t) = 1 - \frac{E_{fast}(t)}{E_{fast,rated}}. \quad (6.1)$$

Although multiple battery lifetime models have been investigated thoroughly in [115], the explicit life cycle versus DOD expression is not provided. Using the data points from the manufacturer and extrapolation with detailed parameters, Gee *et al* have formulated a polynomial model for battery cycles in [116], which evaluates the effect of small charge/discharge cycles. This battery cycle model is adopted and its parameters are partially modified considering a NaS battery performance as follows:

$$\begin{aligned} C_{DOD} = & a \cdot DOD^{-4} + b \cdot DOD^{-3} + c \cdot DOD^{-2} + d \\ & \cdot DOD^{-1} + e \quad \text{where } a = -1.35 \times 10^{-12}, b = 1.5 \\ & \times 10^{-7}, c = -1.51 \times 10^{-3}, d = 1580.5, e = -115. \end{aligned} \quad (6.2)$$

The lifetime cycles of the battery in (6.2) is shown in Figure 6.1. The ESS lifetime depreciation will be computed based on this characteristics.

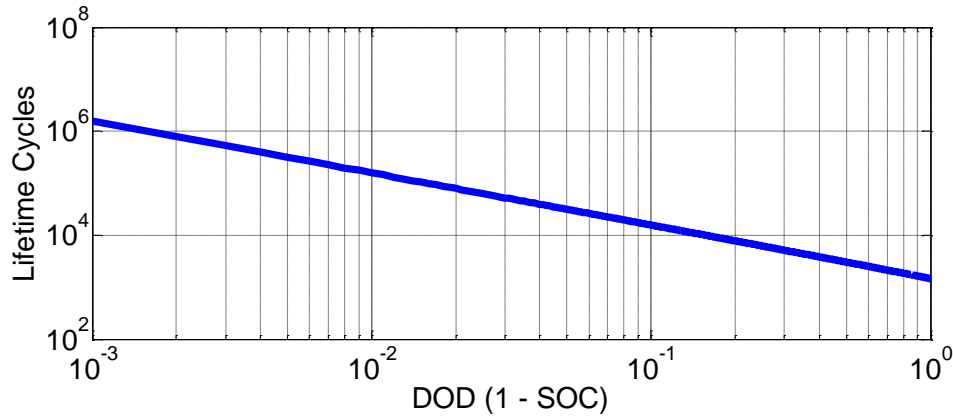


Figure 6.1: Battery lifetime cycle versus DOD in logarithmic domain. This curve is derived by linear extrapolating the data from manufacturer.

The battery-based ESS, in fact, is frequently charged and discharged in incomplete cycles, e.g. from $SOC = 0.8$ to $SOC = 0.5$, creating more complicated cases for accessing its lifetime consumption. A rainflow-counting algorithm developed in [120] for counting metal fatigue cycles can be employed to calculate incomplete charge/discharge cycles. Ke *et al* have successfully utilized this method to assess the lifetime of an ESS when it is used to compensate for power imbalances of variable generation sources [106]. Figure 6.2 demonstrates an example of the rainflow algorithm counting incomplete cycles with SOC time series used as the input. The SOC time series in Figure 6.2(a) is converted into independent ranges and displayed in Figure 6.2(b). The lifetime depreciation of the ESS can thus be derived by those ranges.

The lifetime consumed during an incomplete cycle is computed by converting it into two complete cycles illustrated as follows [106]:

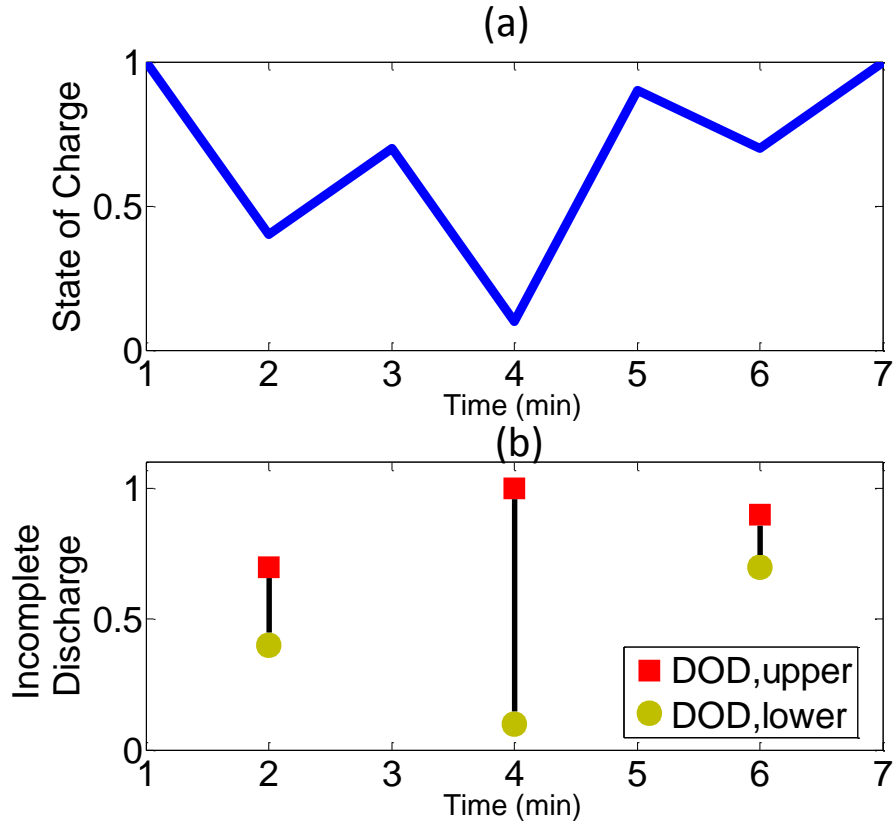


Figure 6.2: An example of counting incomplete ESS charge/discharge cycles in a complex working condition using the rainflow algorithm: (a) Input SOC time-series data; (b) Incomplete cycles counted by rainflow algorithm.

$$\begin{aligned}
 L_{depre}^{Incomplete} &= L_{depre,lower}^{Complete} - L_{depre,upper}^{Complete} \\
 &= 1/C_{DOD,lower} - 1/C_{DOD,upper}.
 \end{aligned}
 \tag{6.3}$$

Finally, the total battery ESS lifetime depreciation is the summation of all cycles, including incomplete and complete cycles, using the following equation:

$$L_{depre}^{Total} = \sum L_{depre}^{Incomplete} + \sum L_{depre}^{Complete}. \quad (6.4)$$

6.2 Generic ESS Modeling and Power Forecasts

In this section, the fast- and slow-response ESSs are modeled based on the time-series data. The desired power profile, namely the forecasted hourly wind power, is determined.

6.2.1 A Generic ESS Model

Modeling an ESS involves in the consideration of response time. Mechanical ESS with larger energy storage capacities, such as pumped hydro and compressed air ESSs, react slower compared to power-electronics-based battery and super-capacitor ESSs. Because the variability mitigation target is the wind power time series with a 1-minute resolution, power dispatch strategies are realized as steady-state analyses [121, 122]. Using the power data from a 38-MW wind farm, a generic ESS model can be generalized in time-series fashion by the energy conversion P_{total} and E_{ess} :

$$P_{total}(t) = P_{ess}(t) + P_{wind}(t), \quad (6.5)$$

$$E_{ess}(t) = \begin{cases} E_{ess,rated} & (\text{if } SOC = 1) \\ \sum_{i=0}^t \eta \cdot t_{ramp}^{-1} \cdot P_{ess}(i) + E_{ess,rated} \cdot SOC(0) & (\text{if } 0 < SOC < 1) \\ 0 & (\text{if } SOC = 0). \end{cases} \quad (6.6)$$

With the above model, fast- and slow-response ESSs for this work can be performed by specifying a changing rate limiter to P_{ess} . The battery-based fast-response ESS therefore acquires a response time down to 1 minute, identical to that of the data resolution. In contrast, the power changing rate of the slow-response ESS is limited in terms of a ramp time t_{ramp} which indicates the time needed to from $P_{ess} = 0$ to $P_{ess} = 1$ p.u. A typical value of t_{ramp} is $t_{ramp,slow} = 30$ min. One-way energy conversion efficiencies for both ESSs are considered, i.e., $\eta_{fast} = 0.85$ and $\eta_{slow} = 0.7$.

6.2.2 Wind Power Forecast

To size the ESS and design power dispatch schemes, a desired power profile is required as the input reference of the system. Following several other studies, there are two major sources for this input power reference: using the load demand [3, 123, 124] or using the forecasted wind power [4, 108]. From a system operating and reliability perspective, introducing load demand to determine the power dispatch is preferable. However, because the load demand is not correlated with the wind power generation, significant energy deficiency/surplus may occur frequently. Using load demand approach as the desired power profile, thus, is not suitable for operating the ESS due to its

finite amount of energy availability. In this study, the ESS application aims for mitigating power variability quantified by the CRM when the load demand is not an assumed prerequisite. Accordingly, forecasted power profiles are applied.

6.2.2.1 Persistence forecast

To ease wind power uncertainties imposed on the grid power flow, persistence forecasts can be implemented. Referring to the definition in [119], the persistence forecast assumes future wind power production will remain the same as the last measured value. By averaging the last N measured wind production values, the persistence predictor can be written as:

$$\hat{P}(t + k_{predict}|t) = \sum_{i=0}^{N-1} P_{total}(t - i) / N. \quad (6.7)$$

Three scenarios [108] for the persistence forecast are ‘T×2’, ‘T×1’, and ‘T×0’, listed from the worst case to the best. Their prediction horizons are $k_{predict} = \{T, 0, -T\}$. In order to minimize the impact of forecast errors on ESS sizing and control deployments, the best-case prediction T×0 is implemented regarding power fluctuations only within T . Due to the moving average, the persistence forecast generates a smoothed power profile with a reduced short-term variability.

6.2.2.2 Power step-change (PSC) forecastt

For wind farm owners who need to announce their committed generation levels to the market in advance, the PSC forecast is more applicable than the persistence forecast. The persistence forecast can hence be modified: Instead of creating a smoothed power profile, power can be predicted in terms of hourly step changes. The reference power is sectionalized into T -long intervals within which the desired power is constant. Forecasted wind power from persistence and PSC methods with the prediction $T \times 0$ is illustrated in Figure 6.3. In order to reduce hourly wind power variations for the aim of this section, the prediction period here must be at least 60 min. In Figure 6.3, $T = 120$ min is plotted for illustrative purpose.

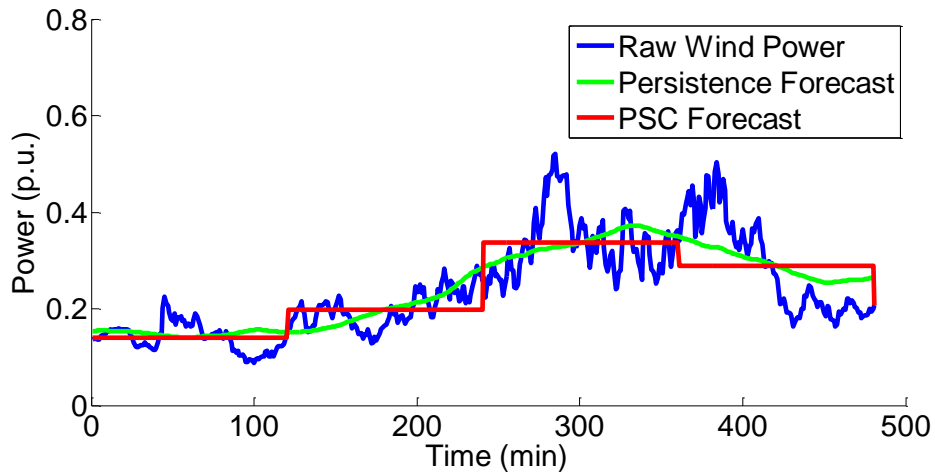


Figure 6.3: Demonstration of persistence forecast and PSC forecast with a prediction period of $T = 120$ min.

Quantified by the CRM, intra-hour variability from the raw wind power, persistence-forecasted power, and PSC-forecasted power during Year 1 are

displayed in Figure 6.4. The quantification considers a $p = 90\%$ coverage rate and a 1-hour observation interval. The diagonal curves represent the maximum and minimum power production outputs. The grey scale portions are the conditional ranges, namely the potential power varying range with respect to p and k . The coverage rate p and observation interval length k indicate that within k -long duration, the wind power will vary between maximum and minimum outputs 90% of the time. Note that, although the PSC forecast portrays less variations within each step, the sudden change between steps will, in fact, increase the short-term variability. This sudden change induces serrations in the CRM diagram in Figure 6.4. A lower coverage rate p can minimize the serrations by excluding the sudden change between consecutive steps in the gamma probability model.

6.3 Sizing the ESSs

Using the CRM, wind power variability can be accurately quantified. The sizing for ESS power and energy capacity ratings can also be determined by this method.

6.3.1 Sizing the Power Capacity Ratings P_{ess}

Aiming for mitigating intra-hour power variations, the ESS power rating can be determined by hourly variability analysis of the raw wind power data in Year 1. The desired variability reduction is quantified by $k = 60$ min and $p \geq 90\%$. The ESS must be sized so that p is no smaller than 90%. Since

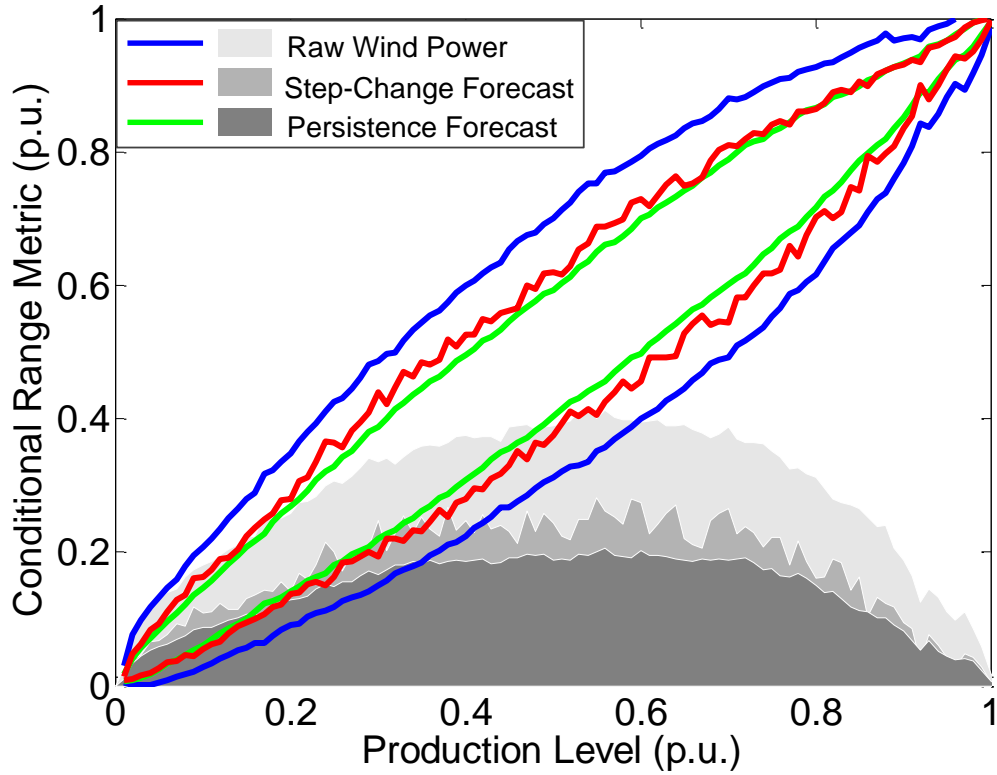


Figure 6.4: Quantified wind power variability from the raw wind power, persistence-forecasted power, and PSC-forecasted power. A larger CRM can be found from PSC method due to its sudden power change between consecutive steps.

the CR in Figure 6.4 represents the power variations within k -long duration, its peak value can be used as the ESS power rating P_{ess} . However, applying the CR peak value will significantly oversize the ESS, due to the opportunity of working at the maximum point is fractional. Therefore, it is more realistic to assume a power output by an averaged CR value across all production levels. Using equations (5.1) and (5.2), the averaged conditional range can be computed accordingly.

The fast-response ESS needs to cover the rapid power variations within the ramping time of the slow-response ESS, $P_{ess,fast}$ is computed from $k = 30$ min. Figure 6.5 demonstrates the CR and w_{l_j} for $p = 90\%$. The averaged CR is computed by summing the product values of CR and w_{l_j} at each production level l_j . In this design, the fast-response ESS power rating is $P_{ess,fast} = 0.163$ p.u. With a different coverage rate p , the power ratings can vary widely. Table 6.1 lists the power ratings under various coverage rate p . It should be noted that the 10% uncovered power by assigning $p = 90\%$ does not necessarily mean a loss of control. Rather, they are the regions with power demands partially supplied by the ESS.

Table 6.1: Power Ratings of the Fast-Response ESS (p.u.)*

p	99%	97%	95%	93%	91%	89%
$P_{ess,fast}$	0.258	0.214	0.193	0.178	0.167	0.158

*: The base power for 1 p.u. is $P_{base} = 38$ MW

6.3.2 Sizing the Energy Capacity Ratings E_{ess}

Similar to P_{ess} , the energy capacity rating E_{ess} is also determined probabilistically in terms of an expected coverage for potential energy deficiency/surplus. Unlike the coverage in P_{ess} , uncovered energy is located in the regions without any controllability.

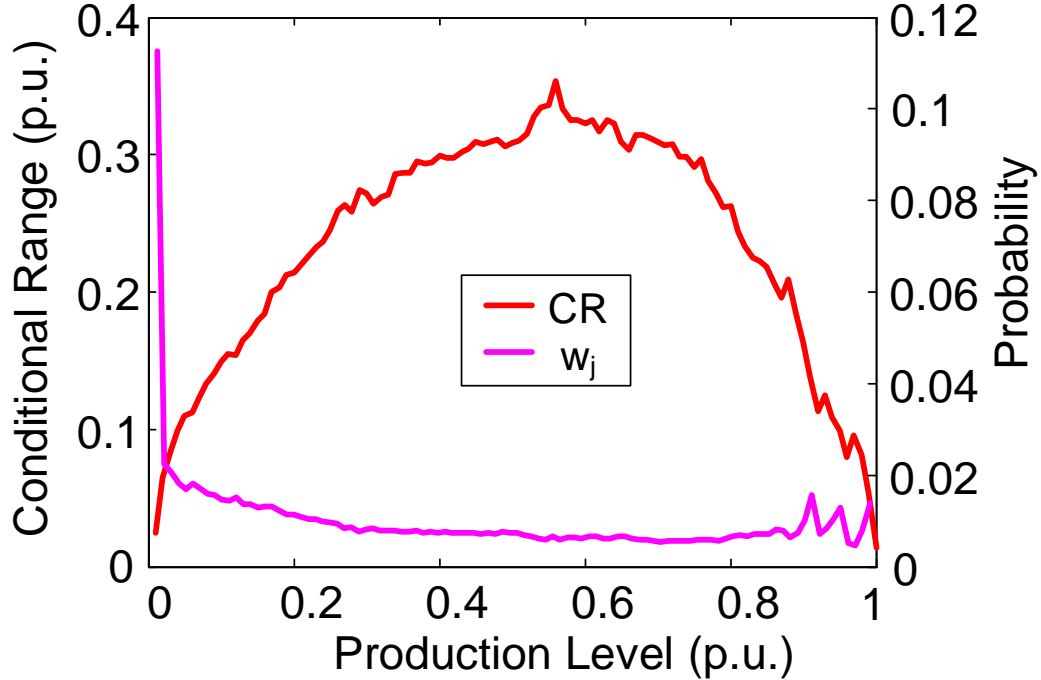


Figure 6.5: Sizing power ratings of the fast-response ESS using CR and w_j . The ESS size is determined by the expectation of CR for $k = 30$ min and $p = 90\%$.

6.3.2.1 Determining Energy Capacity of the Slow-Response ESS

The slow-response ESS is utilized to continuously control energy deficiency/surplus and its energy capacity for persistence and PSC forecasts is the same. This is due to both forecasts reduce power variability by averaging power production across a forecasted period. Considering a maximum power deficiency, the slow-response ESS must be capable of supplying uninterrupted power within k -long time ($k = 60$ min in this case). This uninterrupted power assumption is even preferable if the fast-response ESS needs to charge from or

discharge to the slow-response ESS to extend its lifetime and to more flexibly handle short-term power variability.

Applying the averaged CR in (5.2), energy capacity $E_{ess,slow}$ of the slow-response ESS can be determined. Due to the energy conversion efficiency η considered during the generic ESS modeling, the expression for computing $E_{ess,slow}$ is as follows:

$$E_{ess,slow} = CR_{avg,k,p} \cdot k / \eta_{slow}. \quad (6.8)$$

Table 6.2 articulates the energy capacity ratings of the slow-response ESS regarding various coverage rate p .

Table 6.2: Energy Capacity Ratings of the Slow-Response ESS (p.u.h)*

p	99%	97%	95%	93%	91%	89%
$E_{ess,slow}$	0.520	0.436	0.396	0.368	0.347	0.329

*: The base energy capacity for 1 p.u.h is $E_{base} = 38$ MWh

6.3.2.2 Determining Energy Capacity of the Fast-Response ESS

The fast-response ESS is not necessarily sized by assuming a continuous power supply within $t_{ramp,slow}$ -long duration. Since it can partially rely on the slow-response ESS within $t_{ramp,slow}$ and is designed to compensate for intra-hour power variations with higher power-changing rates, its energy ratings for the persistence and PSC forecasts are not calibrated as they are for the slow-response ESS.

To properly size the fast-response ESS, energy throughput needs to be represented for the entire year regarding a specific power reference. Because the design implements Year 1 data as a ‘pool’, errorless forecasts can be achieved via both forecast methods. Deficiency and surplus energy between forecasted wind power and raw power time series can be integrated to form an energy throughput series. Then, a probability density function is developed to fit the data from the energy throughput series in the same fashion as fitting the power deviation series into the gamma distribution during CRM development. Although applying a distribution to the data can be subjective rather than objective, increasing the sample size can minimize the hypothesis error. A normal distribution with additional margin taken into account is suitable to serve this purpose.

To perform a normal fit for the energy throughput data, a cut-off value must be set: Values smaller than 10^{-5} p.u.h are substituted by zeros in the probabilistic modeling. It is because the idealized ESS will charge/discharge even if the power deficiency/surplus is negligible. This assumption is practical as most ESSs in the real world will not respond to such small demand. Calculating the confidence interval of the normal distribution with respect to a specific coverage requirement allows the energy capacity of the fast-response ESS to be determined. Due to the two-way power flow, the energy capacity $E_{ess,fast}$ is represented by the entire span of the confidence interval. Table 6.3 partially enumerates the sizing results with persistence and PSC prediction methods. To maintain a constant power output from the PSC forecast,

a noticeable energy capacity increase must be resolved. Note that the consideration about the energy conversion efficiency consideration, $\eta_{fast} = 0.85$, has already been integrated into the calculation.

Table 6.3: Energy Capacity Ratings of the Fast-Response ESS (p.u.h)

p	99%	97%	95%	93%	91%	89%
Persistence	0.0903	0.0761	0.0687	0.0635	0.0594	0.0560
PSC	0.158	0.133	0.120	0.111	0.104	0.0979

Figure 6.6 depicts an illustration of how a fast-response ESS fails to support energy deficiency or absorb surplus energy. The power regulated by the fast-response ESS suffers a sudden change (marked by black ovals in Figure 6.6) when the ESS is fully charged ($SOC = 1$) or discharged ($SOC = 0$). This sudden change, along with the high power-changing rate, accounts for an increase in the intra-hour power variability quantified by the CRM analysis.

6.4 Control Methods and Power Dispatch Schemes

Control methods and power dispatch schemes are used to reduce wind power variability with minimal ESS lifetime depreciation. Two ESS configurations and control strategies are proposed, which create multiple power dispatch schemes under various scenarios and applications.

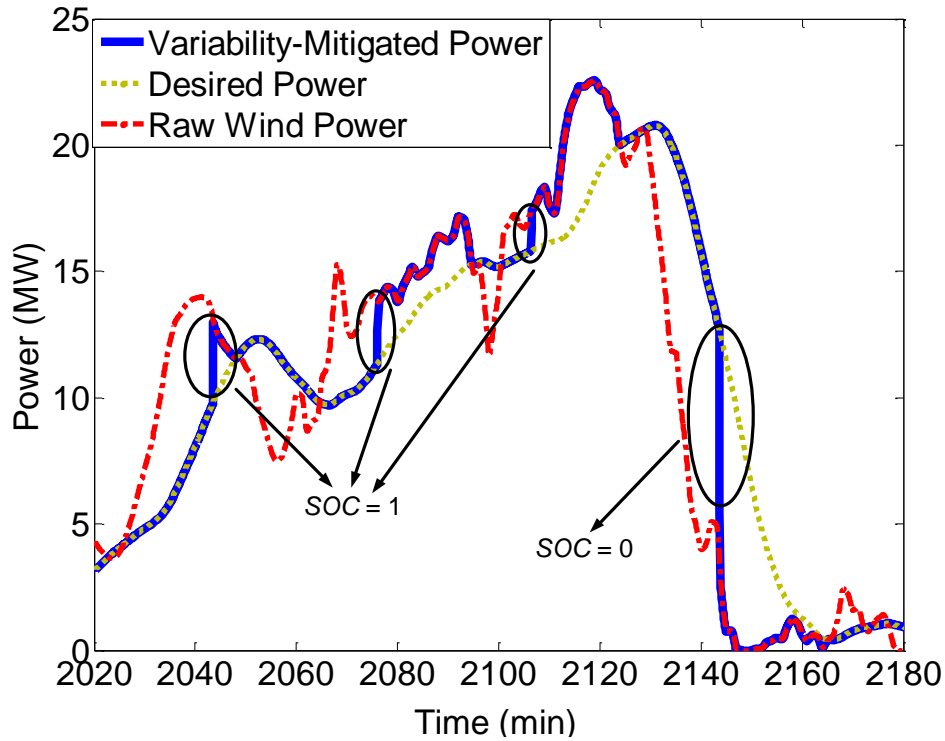


Figure 6.6: Incapability of the fast-response ESS in supporting energy deficiency or absorbing the surplus. This incapability will increase the variability in terms a high rate power change.

6.4.1 System Configurations

6.4.1.1 Series Regulation

Illustrated by the flowchart in Figure 6.7, the raw wind power is preliminarily regulated by the slow-response ESS. Due to the sluggishness of the slow-response ESS, the fast-response ESS will continue compensating for the remaining demand afterwards.

The series regulation layout can maximize the ESS utilization, i.e. using the slow-response ESS to manage long-term power deficiency/surplus while

mitigating the fast-changing wind power variability through the fast-response ESS. The ESS controls are not independent because the fast-response ESS must be controlled with the power output information from the slow-response ESS. Thus, the fast-response ESS should be installed geographically downstream from the slow-response ESS. Alternatively, real-time communication between the two ESSs is required if they are placed together or if the fast-response ESS is installed upstream.

6.4.1.2 Parallel Regulation

Emphasizing controlling independence, Figure 6.8 introduces a parallel power regulation configuration by compensating for the power demand independently between the fast- and slow-response ESSs. To avoid repetitive flowcharts, the same components representing ESSs are replaced by colored blocks in Figure 6.8.

The duties of the two types of ESSs can be allocated by different control rubrics. In Figure 6.8, a rate separator serves as a duty allocator, determining which ESS should operate. This system setup allows the fast- and slow-response ESSs to operate independently according to their corresponding duties without any geographical constraints or operational data from each other. But there are trade-offs for this independence flexibility: The lack of cooperation will induce over or under adjustment from certain power deficiency/surplus. Moreover, the duty allocator cannot ensure a balanced power throughput during charge and discharge, which can lead to a complete charge

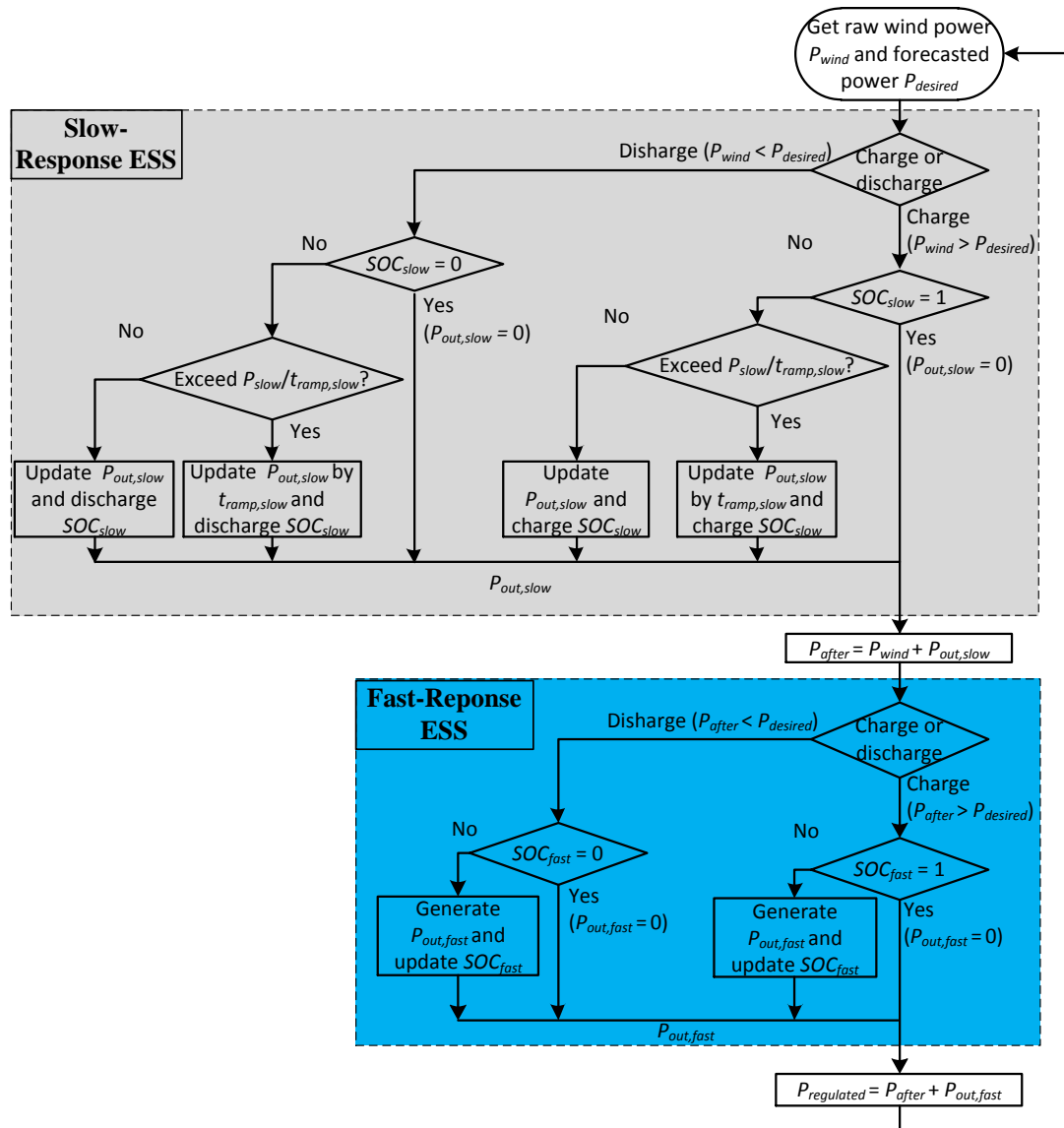


Figure 6.7: Series power regulation layout with the slow-response ESS at the upstream.

($SOC = 1$) or discharge ($SOC = 0$) of the ESSs.

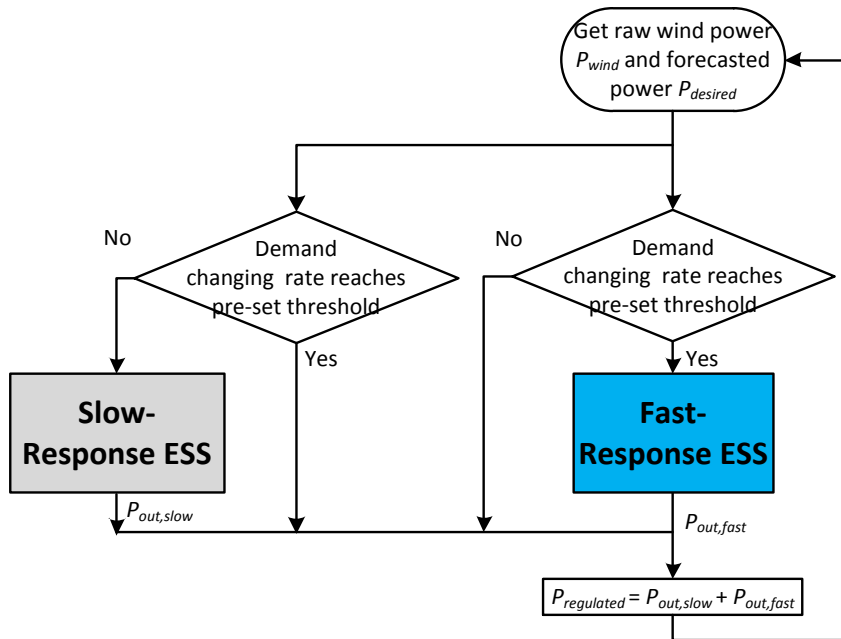


Figure 6.8: Parallel power regulation layout with a rate separator.

6.4.2 ESS Control Methods

In addition to the ESS configurations, two ESS control methods are proposed. The control methods can cooperate with any ESS layout, resulting in various combinations for different

6.4.2.1 SOC Band Control (BC)

Regulating SOC in a desired hysteresis, SOC band control has been adopted by battery management systems in hybrid vehicles. This method is also applicable for the purpose in this study. Reference [117] and [118] have applied BC to coordinate a flying wheel ESS with a conventional generator to gain extra system flexibility.

To implement the BC method, the slow-response ESS must be able to coordinate with the fast-response ESS, charging or discharging the fast-response ESS to its required range. Therefore, a state of charge hysteresis $SOC_C = [C_1, C_2]$ and a discharge hysteresis $SOC_D = [D_1, D_2]$ are defined according to $C_1 < C_2 < D_1 < D_2$. The fast-response ESS is expected to operate with SOC between C_2 and D_1 . If the SOC drops below C_1 , it will be charged by the slow-response ESS or the surplus wind energy back to C_2 ; if the SOC exceeds D_2 , the surplus energy will be absorbed by the slow-response ESS or the grid. The SOC regulation can increase the ESS availability and power variability reduction effectiveness, but will induce extra lifetime depreciations to the fast-response ESS due to the additional charge/discharge cycles.

In order to find the optimal range for SOC_C and SOC_D , a Monte Carlo iteration is approached using the wind power data in Year 1. The values of SOC_C and SOC_D for persistence and PSC forecasts are displayed in Table 6.4.

Table 6.4: Optimal Ranges for SOC_C and SOC_D

	SOC_C	SOC_D
Persistence Forecast	[0.2, 0.45]	[0.55, 0.9]
PSC Forecast	[0.05, 0.2]	[0.8, 0.85]

6.4.2.2 Fuzzy Control (FC)

Instead of explicitly controlling the fast-response ESS, its power output can be regulated by a fuzzy logic controller to allocate the charge/discharge

duty.

Input variables of the FC include power demand from the forecast methods and the present SOC of the fast-response ESS. The SOC input has three triangular membership functions: Charged, Moderate, and Discharged, while the power demand has five trapezoidal membership functions: Large Deficiency/Surplus, Small Deficiency/Surplus, and Balanced. The FC output with five membership functions is similar to the power demand definition, which delivers a charge/discharge reference integrated into the fast-response ESS block in Figure 6.7 and Figure 6.8. The output surface of the membership functions is shown in Figure 6.9.

Compared to BC, FC does not require the slow-response ESS to actively exchange energy with the fast-response ESS. Rather, the fast-response ESS is self-regulated by its own reference from the surface in Figure 6.9.

6.5 Result Evaluation and Analysis

The two system configurations and two ESS control methods introduced in Section V can result in six different combinations, including the basic power demand control (DC). In DC, the fast-response ESS is regulated linearly by the power demand between the forecasted power and the present wind power. Considering the real-world scenarios, operational independence respect to these combinations are investigated and listed in Table 6.5. If the ESSs can be controlled independently without communicating the operational information between each other, the control method is considered indepen-

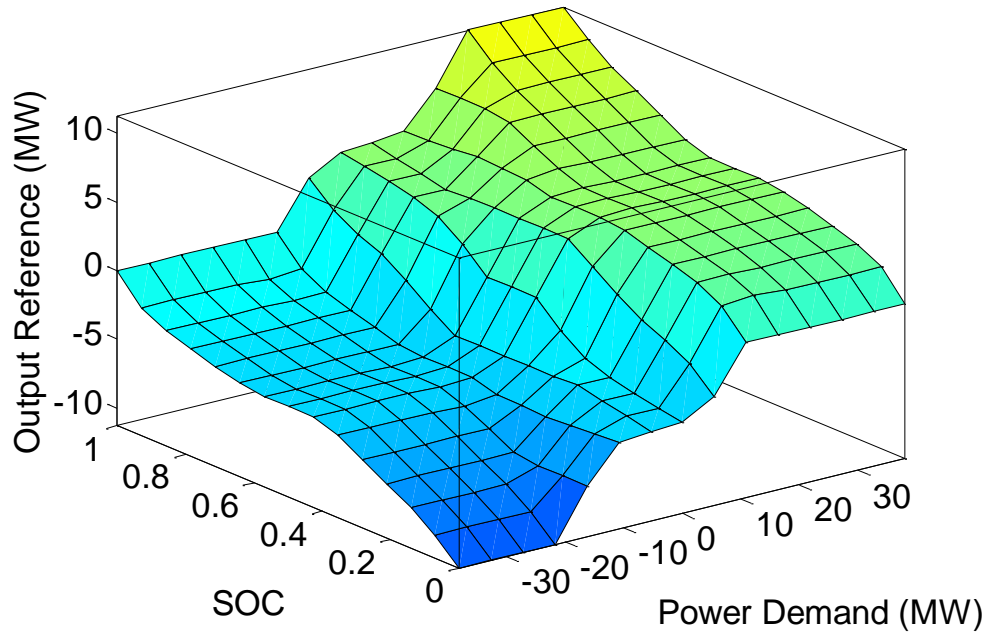


Figure 6.9: Output surface of the fuzzy control (FC) membership functions.

dent. Therefore, in Table 6.5, the less the degree of operational independence, the more information and coordination are required from both ESSs.

Table 6.5: Operational Independence of Control Methods

	Demand Control (DC)	Band Control (BC)	Fuzzy Control (FC)
Series Regulation	**	*	**
Parallel Regulation	***	**	***

*: Degree of operational independence

To evaluate the proposed ESS sizing and control methods with adaptability, wind power data in Year 2 is implemented as source data for the simulation. All power dispatch schemes in Table 6.5 are tested for power variability mitigation effectiveness under persistence and PSC forecast methods.

Figure 6.10 illustrates the results computed by averaged CR via (4.4) and (5.2) with $k = 60$ min and $p = 90\%$. Power variability reduction can be seen by comparing the averaged CR from raw wind power variability and desired variability. To demonstrate the efficacy of the proposed methods, the best case of using fast-response ESS only with DC is provided. The power and energy ratings for the case ‘Fast ESS Only’ uses the aggregated values of the fast- and slow-response ESS ratings applied to other cases. As shown in Figure 6.10, with more cooperation information from both ESSs, the series regulation method achieves better results even than using the fast-response ESS only. Table 6.6 summarizes the lifetime depreciations of the fast ESS during Year 2. By combining the operational independence, power variability mitigation capability, and lifetime usage, the parallel layout has been found less effective but can be controlled more independently with a longer ESS life span.

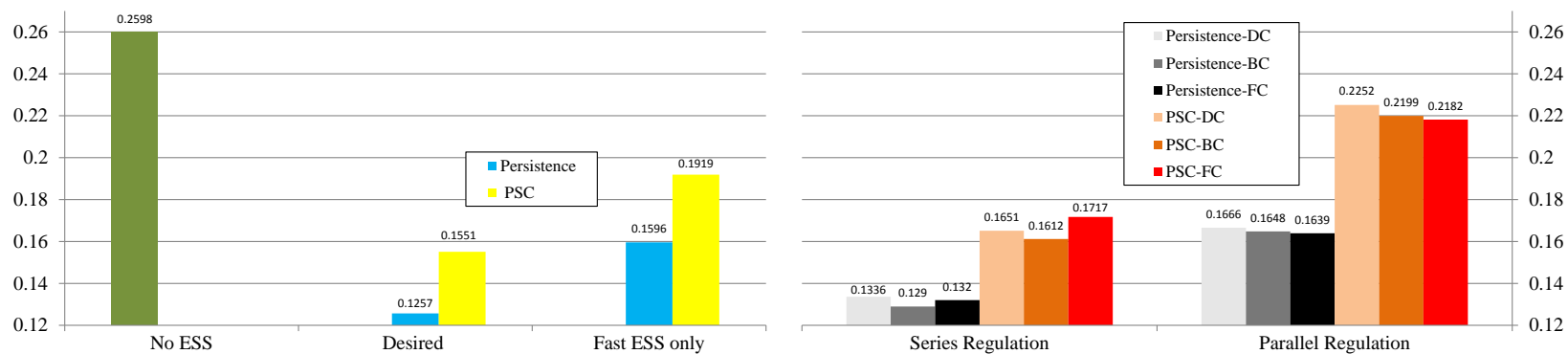


Figure 6.10: Comparison of wind power variability mitigation effectiveness with methods in Table 6.5.

Table 6.6: Lifetime Depreciation Assessment of the Fast-Response ESS

	Fast-Response ESS Only	Series Regulation			Parallel Regulation		
		DC	BC	FC	DC	BC	FC
Persistence Forecast	8.91%	3.12%	5.60%	3.12%	0.21%	0.22%	0.08%
Power Step-Change Forecast	11.9%	3.67%	5.52%	3.80%	0.12%	0.09%	0.04%

Figure 6.11 depicts the CR through the entire production level using Persistence-BC with series regulation layout from Figure 6.10. The power of the fast-response ESSs is 13.4 MW, while the energy capacities are only 2.61 MWh for the persistence forecast and 4.56 MWh for the PSC forecast, compared to a 38 MW wind farm. For larger wind farms, which possess lower power variability due to stochastic aggregations, the per-unitized ESS power and capacity ratings can be reduced even further. By implementing proper sizing and coordination control methods, ESSs with reduced size can successfully mitigate intra-hour power variability up to 90%.

6.6 Summary

To reduce intra-hour wind power variability, this section has presented methods of sizing and controlling a system consisting of a fast-response ESS and a slow-response ESS. The probabilistic ESS sizing method based on the CRM and power throughput can properly determine the required ESS power and capacity ratings in respect to persistence and PSC power forecasts. Regarding operational independence, power dispatch schemes have been proposed in terms of two system layouts and two ESS control strategies. A variety of layout and control combinations have been evaluated in two ways: first, using the averaged CR to compare variability mitigation effectiveness; second, using the rainflow algorithm to assess lifetime depreciation of the fast-response ESS. To summarize the comparisons, with the proper system layout and control, using fast- and slow-response ESSs performs even better than the system with

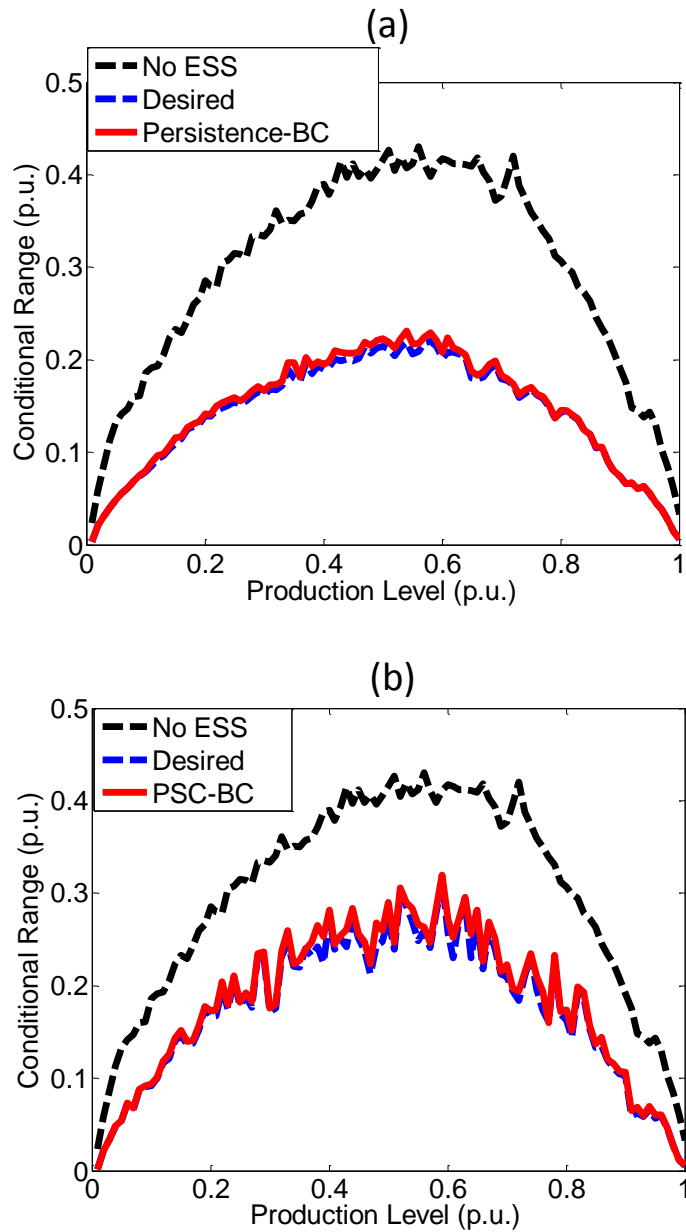


Figure 6.11: CR from series regulation with persistence and PSC power forecasts: (a) CR from persistence forecast; (b) CR from PSC forecast.

only a fast-response ESS under the same power and energy capacity ratings.

Chapter 7

Conclusions

As an inherent characteristic, wind power variability, together with imbalances it has incurred, imposes uncertainties and operation risks onto the traditional electric power grid. Proper probability modeling and variability quantification can extend the knowledge span of wind power variations. With the employment of energy storage systems, the non-dispatchable wind energy can be harnessed by buffering its power output. By studying, quantifying and mitigating wind power variability, this work has presented comprehensive research on wind turbine design and modeling, model reduction, wind power variability quantification, generation scenario generalization, and ESS sizing and coordination. Thus, this dissertation contributes the following conclusions:

- *Modeling and Parametric Design of Direct-Drive Wind Turbines*

With complete manufacturer independence, parametric design and modeling of a 1.5-MW direct-drive Type 4 wind turbine have been outlined with detailed derivation and calculation. Commencing with rotor blade performance and permanent magnet synchronous machine data, a series of equations for determining preliminary aerodynamic and electrical

design parameters of a direct-drive wind turbine with a given converter topology has been presented. Serving as a case study, these equations can determine blade radius, expected cut-in, rated, and cut-out wind speeds, sizes of inline inductors on machine and grid sides and the DC capacitor, and controller limits accurately. Data from simulations demonstrates that the system features a promising performance on both steady-state operation and dynamic response.

- *Model Reduction, Validation and Analysis of Direct-Drive Wind Turbines*

Reduced order models of the designed Type 4 wind turbine have been proposed to fill the gap between fully dynamic models and steady-state models, providing the possibility of simulating a wind turbine through long-term (monthly or annual) operations under an acceptable CPU runtime with the response for major dynamic events such as voltage sags, power systems faults, and controlling and regulating events. These models still possess controllability on the rotor blades, DC-link voltage and reactive power. The final quasi-dynamic model has been validated using real-world wind speed data throughout the year of 2004.

- *Quantification of Wind Power Variability*

Focusing on improving algorithm adaptability and robustness, the probability kernel of the oCRM has been reformulated by a continuous gamma distribution. Distribution parameters have been accurately estimated

by maximum likelihood estimators and evaluated by Bayesian inference with a modified bivariate rejection sampling algorithm. The improved method, namely, the sCRM, has adapted to create a tolerance for noisy sampled data up to 10% in the power time-series, as well as scarce data up to 30 minutes per sample point. This metric is preferable for predicting wind power variability in a short timespan or planning reserved generation. It is also usable to size the power and energy ratings of a ESS.

- *Scenario Generalization of Wind Power Generation*

To generalize stochastic generation scenarios of correlated wind turbines, unsupervised machine learning algorithms for clustering and dimensional reduction has be employed. Using a K -means clustering algorithm, power data samples from three correlated wind turbines have been clustered into scenarios with their respective discrete probability distributions. The feature dimension of these scenarios have also been reduced from 3-D to 1-D with retained variance up to 97.5% using a principal component analysis algorithm.

- *Sizing and Coordinating Fast- and Slow-Response Energy Storage Systems to Mitigate Wind Power Variations*

Considering the controllability, practicability, cost-efficiency, and service lifetime, the employment of a hybrid energy storage system, which contains a fast battery-based energy storage and a slow generator-based

energy storage, has been presented to mitigate wind power variations. Comprehensive methods including sizing, system layout, power dispatch, and coordination control have been proposed. Using optimal power and energy capacity ratings for the fast-response energy storage, the wind power variability can be reduced to meet the desired prediction profile under a proper control scheme a minimum lifetime depreciation on the fast-response energy storage.

Appendices

Appendix A

Machine and Converter Data

Converter data and PMSM parameters are shown in the following table.

Converter Parameters	
Converter type	Two-level voltage source
Power electronic device	IGBT with reverse diode
Grid inline inductor L_{ac}	0.1296 mH (0.23 pu)
DC-link voltage V_{dc}	1220 V (3.06 pu)
DC capacitor size C	24.98 mF (2.0 pu)
Modulation/frequency	SPWM ($m_a = 0.8$) / 2400 Hz
Machine Parameters	
Machine type	PMSM, non-salient pole
Rated apparent power	2.2419 MVA (1.0 pu)
Rated active power	2.0 MW (0.8921 pu)
Rated current	1875.9 A (1.0 pu)
Rated line-to-line voltage (r.m.s.)	690V (1.0 pu)
Rated frequency	9.75 Hz
Rated speed	15 rpm (1.0 pu)
Pole pairs	39
Rated rotor flux (peak: λ_r)	8.2041 Wb (0.8921 pu)
Stator resistance	0.821 m Ω (0.00387 pu)
d axis inductance L_d	1.5731 mH (0.4538 pu)
q axis inductance L_q	1.5731 mH (0.4538 pu)

Bibliography

- [1] “Western wind resources dataset,” National Renewable Energy Laboratory. [Online]. Available: http://wind.nrel.gov/Web_nrel/
- [2] “Global statistics of wind power industry,” Global Wind Energy Council (GWEC), 2015. [Online]. Available: <http://www.gwec.net/global-figures/graphs/>
- [3] H. T. Le, S. Santoso, and T. Q. Nguyen, “Augmenting wind power penetration and grid voltage stability limits using ess: Application design, sizing, and a case study,” *IEEE Transactions on Power Systems*, vol. 27, no. 1, pp. 161–171, Feb. 2012.
- [4] T. K. A. Brekken, A. Yokochi, A. Jouanne, Z. Z. Yen, H. M. Hapke, and D. A. Halamay, “Optimal energy storage sizing and control for wind power applications,” *IEEE Transactions on Sustainable Energy*, vol. 2, no. 1, pp. 69–77, Jan. 2011.
- [5] G. Hug-Glanzmann, “Predictive control for balancing wind generation variability using run-of-river power plants,” in *2011 IEEE Power and Energy Society General Meeting*, July 2011, pp. 1–8.
- [6] Z. Zhang, Q. Zhou, and A. Kusiak, “Optimization of wind power and its

- variability with a computational intelligence approach,” *IEEE Transactions on Sustainable Energy*, vol. 5, no. 1, pp. 228–236, Jan 2014.
- [7] M. Khodayar, M. Shahidehpour, and L. Wu, “Enhancing the dispatchability of variable wind generation by coordination with pumped-storage hydro units in stochastic power systems,” *IEEE Transactions on Power Systems*, vol. 28, no. 3, pp. 2808–2818, Aug 2013.
- [8] T. Boutsika and S. Santoso, “Sizing an energy storage system to minimize wind power imbalances from the hourly average,” in *2012 IEEE Power and Energy Society General Meeting*, July 2012, pp. 1–8.
- [9] F. Vallee, J. Lobry, and O. Deblecker, “Impact of the wind geographical correlation level for reliability studies,” *IEEE Transactions on Power Systems*, vol. 22, no. 4, pp. 2232–2239, Nov 2007.
- [10] D. Gezer, A. Nadar, C. Sahin, and N. Ozay, “Determination of operating reserve requirements considering geographical distribution of wind power plants,” in *2011 International Conference on Clean Electrical Power (IC-CEP)*, June 2011, pp. 797–801.
- [11] P. Zhou, Y. He, and D. Sun, “Improved direct power control of a dfig-based wind turbine during network unbalance,” *IEEE Transactions on Power Electronics*, vol. 24, no. 11, pp. 2465–2474, Nov 2009.
- [12] Y. Liu, Q. Wu, X. Zhou, and L. Jiang, “Perturbation observer based multiloop control for the dfig-wt in multimachine power system,” *IEEE*

- Transactions on Power Systems*, vol. 29, no. 6, pp. 2905–2915, Nov 2014.
- [13] M. Singh and S. Santoso, “Dynamic models for wind turbines and wind power plants,” National Renewable Energy Laboratory, Technical report, 2011.
- [14] M. Singh and S. Santoso, “Dynamic model for full-converter wind turbines employing permanent magnet alternators,” in *2011 IEEE Power and Energy Society General Meeting*, July 2011, pp. 1–7.
- [15] B. Wu, *Power Conversion and Control Wind Energy Systems*. Canada: Wiley-IEEE Press, 2011.
- [16] P. Anderson and A. Bose, “Stability simulation of wind turbine systems,” *IEEE Transactions on Power Apparatus and Systems*, vol. PAS-102, no. 12, pp. 3791–3795, Dec 1983.
- [17] Y. Niu and S. Santoso, “Determination of design parameters for direct-drive wind turbines,” in *2014 IEEE PES General Meeting*, July 2014, pp. 1–5.
- [18] Y. Niu and S. Santoso, “Model reduction and design of direct-drive wind turbines,” *Energies (submitted)*.
- [19] Y. Niu and S. Santoso, “Conditional range metric for determining wind power variability of scarce or noisy data,” *IEEE Transactions on Sustainable Energy*, vol. 6, no. 2, pp. 454–463, Apr. 2015.

- [20] Y. Niu and S. Santoso, “Generalizing wind power generation scenarios using unsupervised machine learning,” in *2016 IEEE PES General Meeting (submitted)*.
- [21] Y. Niu and S. Santoso, “Determining optimal energy storage size to mitigate intra-hour wind power variability,” in *2015 IEEE IAS Annual Meeting*, October 2015.
- [22] Y. Niu and S. Santoso, “Sizing and coordinating fast- and slow-response energy storage systems to mitigate hourly wind power variations,” *IEEE Transactions on Smart Grid (submitted)*.
- [23] T. Iversen, S. Gjerde, and T. Undeland, “Multilevel converters for a 10 mw, 100 kv transformer-less offshore wind generator system,” in *2013 15th European Conference on Power Electronics and Applications (EPE)*, Sept 2013, pp. 1–10.
- [24] J. Conroy and R. Watson, “Low-voltage ride-through of a full converter wind turbine with permanent magnet generator,” *IET Renewable Power Generation*, vol. 1, no. 3, pp. 182–189, September 2007.
- [25] K. Xu, “Research of vector control strategy for wind generation inverter,” Master’s Thesis, Beijing Jiaotong University, December 2007.
- [26] Y. Niu, “Research and design of three-level pwm rectifier system,” Master’s Thesis, Tongji University, March 2012.

- [27] C. Zhang and X. Zhang, *PWM rectifiers and control*. Beijing: China Machine Press, 2003.
- [28] D. Yuan, *AC Permanent Magnet Motor Variable Frequency Drive System*. Beijing, China Machine Press, 2011.
- [29] M. Singh, K. Faria, S. Santoso, and E. Muljadi, “Validation and analysis of wind power plant models using short-circuit field measurement data,” in *2009 IEEE Power Energy Society General Meeting*, July 2009, pp. 1–6.
- [30] Y. Yang and X. Zha, “Aggregating wind farm with dfig in power system online analysis,” in *2009 IEEE 6th International Power Electronics and Motion Control Conference*, May 2009, pp. 2233–2237.
- [31] T. Demiray, F. Milano, and G. Andersson, “Dynamic phasor modeling of the doubly-fed induction generator under unbalanced conditions,” in *2007 IEEE Lausanne Power Tech*, July 2007, pp. 1049–1054.
- [32] D. Vindel, S. Haghbin, A. Rabiei, O. Carlson, and R. Ghorbani, “Field-oriented control of a pmsm drive system using the dspace controller,” in *2012 IEEE International Electric Vehicle Conference (IEVC)*, March 2012, pp. 1–5.
- [33] E. Robles, S. Ceballos, J. Pou, A. Arias, J. Martin, and P. Ibañez, “Permanent-magnet wind turbines control tuning and torque estimation

- improvements,” in *15th IEEE International Conference on Electronics, Circuits and Systems (ICECS 2008)*, Aug 2008, pp. 742–745.
- [34] Z. Wu, W. Gao, J. Wang, and S. Gu, “A coordinated primary frequency regulation from permanent magnet synchronous wind turbine generation,” in *2012 IEEE Power Electronics and Machines in Wind Applications (PEMWA)*, July 2012, pp. 1–6.
- [35] M. Yin, G. Li, M. Zhou, and C. Zhao, “Modeling of the wind turbine with a permanent magnet synchronous generator for integration,” in *2007 IEEE Power Engineering Society General Meeting*, June 2007, pp. 1–6.
- [36] G. Quinonez-Varela and A. Cruden, “Modelling and validation of a squirrel cage induction generator wind turbine during connection to the local grid,” *IET Generation, Transmission Distribution*, vol. 2, no. 2, pp. 301–309, March 2008.
- [37] J. MacDowell, K. Clark, N. Miller, and J. Sanchez-Gasca, “Validation of ge wind plant models for system planning simulations,” in *2011 IEEE Power and Energy Society General Meeting*, July 2011, pp. 1–8.
- [38] L. Trilla, O. Gomis-Bellmunt, A. Junyent-Ferre, M. Mata, J. Sanchez Navarro, and A. Sudria-Andreu, “Modeling and validation of dfig 3-mw wind turbine using field test data of balanced and unbalanced voltage sags,” *IEEE Transactions on Sustainable Energy*, vol. 2, no. 4, pp. 509–519, Oct 2011.

- [39] M. Asmine, J. Brochu, J. Fortmann, R. Gagnon, Y. Kazachkov, C.-E. Langlois, C. Larose, E. Muljadi, J. MacDowell, P. Pourbeik, S. Seman, and K. Wiens, “Model validation for wind turbine generator models,” *IEEE Transactions on Power Systems*, vol. 26, no. 3, pp. 1769–1782, Aug 2011.
- [40] C. d. Boor, “A practical guide to splines,” Springer-Verlag, Technical report, 1978.
- [41] F. N. Fritsch and R. E. Carlson, “Monotone piecewise cubic interpolation,” *SIAM Journal on Numerical Analysis*, vol. 17, no. 2, pp. 238–246, 1980.
- [42] D. Kahaner, C. Moler, and S. Nash, *Numerical Methods and Software*. Prentice Hall, 1988.
- [43] T. Boutsika and S. Santoso, “Quantifying short-term wind power variability using the conditional range metric,” *IEEE Transactions on Sustainable Energy*, vol. 3, no. 3, pp. 369–378, July 2012.
- [44] T. Boutsika and S. Santoso, “Quantifying the effect of wind turbine size and technology on wind power variability,” in *2013 IEEE Power and Energy Society General Meeting*, July 2013, pp. 1–5.
- [45] E. Merran, H. Nicholas, and P. Brian, *Statistical Distributions (Second Edition)*. New York: Wiley, 1993.

- [46] J. F. Lawless, *Statistical Models and Methods for Lifetime Data (Second Edition)*. Hoboken, New Jersey: Wiley, 2003.
- [47] K. O. Bowman and L. R. Shenton, *Properties of estimators for the gamma distribution*. New York: Marcel Decker, 1988.
- [48] W. Q. Meeker and L. A. Escobar, *Statistical Methods for Reliability Data*. New York, Wiley, 1998.
- [49] M. H. DeGroot, *Probability and Statistics (Second Edition)*. Massachusetts: Addison-Wesley, 1989.
- [50] F. A. Moala, P. L. Ramos, and J. A. Achcar, “Bayesian inference for two-parameter gamma distribution assuming different non-informative priors,” *Revista Colombiana de Estadística*, vol. 36, pp. 321–338, Dec 2013.
- [51] Y. S. Son and M. Oh, “Bayesian estimation of the two parameter gamma distribution,” *Communications in Statistics – Simulation and Computation*, pp. 285–293, Feb 2007.
- [52] R. B. Miller, “Bayesian analysis of the two-parameter gamma distribution,” *Technometrics*, vol. 22, no. 1, pp. 65–69, Feb 1980.
- [53] R. Yang and J. O. Berger, “A catalog of non-informative priors,” Institute of Statistics and Decision Sciences, Duke University, Technical report, Dec 1998.

- [54] R. P. Brent, *Algorithms for Minimization Without Derivatives*. New Jersey: Prentice-Hall, 1973.
- [55] G. E. Forsythe, M. A. Malcolm, and C. B. Moler, *Computer Methods for Mathematical Computations. Englewood Cliffs*. New Jersey: Prentice-Hall, 1977.
- [56] G. J. Hahn and S. S. Shapiro, *Statistical Models in Engineering*. Hoboken, New Jersey: Wiley, 1994.
- [57] W. M. Bolstad, *Introduction to Bayesian Statistics (Second Edition)*. Hoboken, New Jersey: Wiley, 2007.
- [58] A. Gelman, J. B. Carlin, H. S. Stern, and D. B. Rubin, *Bayesian Data Analysis (Second Edition)*. Boca Raton, Florida: Chapman, 2004.
- [59] F. A. Moala, P. L. Ramos, and J. A. Achcar, “Bayesian inference for two-parameter gamma distribution assuming different non-informative priors,” *Revista Colombiana de Estadística*, vol. 36, pp. 321–338, Dec 2013.
- [60] R. Yang and J. O. Berger, “A catalog of non-informative priors,” Institute of Statistics and Decision Sciences, Duke University, Technical report, Dec 1998.
- [61] H. Jeffreys, *Theory of Probability (Third Edition)*. Oxford: Oxford University Press, 1961.

- [62] K. Sigman, “Karl sigman’s lecture notes on monte carlo simulation,” Columbia University. [Online]. Available: <http://www.columbia.edu/~ks20/4703-Sigman/Monte-Carlo-Sigman.html>
- [63] W. R. Gilks and P. Wild, “Adaptive rejection sampling for gibbs sampling,” *Applied Statistics*, vol. 41, no. 2, pp. 337–348, 1992.
- [64] D. Görür and Y. W. Teh, “Concave convex adaptive rejection sampling,” *Journal of Computational and Graphical Statistics*, vol. 30, no. 3, pp. 670–691, Jan 2012.
- [65] S. Chakraborty, T. Senjyu, H. Toyama, A. Saber, and T. Funabashi, “Determination methodology for optimising the energy storage size for power system,” *IET Generation, Transmission Distribution*, vol. 3, no. 11, pp. 987–999, Nov 2009.
- [66] S. Bahramirad, W. Reder, and A. Khodaei, “Reliability-constrained optimal sizing of energy storage system in a microgrid,” *IEEE Transactions on Smart Grid*, vol. 3, no. 4, pp. 2056–2062, Dec 2012.
- [67] S. de la Torre, A. Sanchez-Racero, J. Aguado, M. Reyes, and O. Martianez, “Optimal sizing of energy storage for regenerative braking in electric railway systems,” *IEEE Transactions on Power Systems*, vol. 30, no. 3, pp. 1492–1500, May 2015.
- [68] M. Alam, K. Muttaqi, and D. Sutanto, “Mitigation of rooftop solar pv impacts and evening peak support by managing available capacity

- of distributed energy storage systems,” *IEEE Transactions on Power Systems*, vol. 28, no. 4, pp. 3874–3884, Nov 2013.
- [69] Y. Xu and C. Singh, “Adequacy and economy analysis of distribution systems integrated with electric energy storage and renewable energy resources,” *IEEE Transactions on Power Systems*, vol. 27, no. 4, pp. 2332–2341, Nov 2012.
- [70] C. Hill, M. Such, D. Chen, J. Gonzalez, and W. Grady, “Battery energy storage for enabling integration of distributed solar power generation,” *IEEE Transactions on Smart Grid*, vol. 3, no. 2, pp. 850–857, June 2012.
- [71] P. Hu, R. Karki, and R. Billinton, “Reliability evaluation of generating systems containing wind power and energy storage,” *IET Generation, Transmission Distribution*, vol. 3, no. 8, pp. 783–791, August 2009.
- [72] L. de Souza Ribeiro, O. Saavedra, S. de Lima, and J. Gomes de Matos, “Isolated micro-grids with renewable hybrid generation: The case of Lençóis island,” *IEEE Transactions on Sustainable Energy*, vol. 2, no. 1, pp. 1–11, Jan 2011.
- [73] J. de Matos, F. S.F.e Silva, and L. de S Ribeiro, “Power control in ac isolated microgrids with renewable energy sources and energy storage systems,” *IEEE Transactions on Industrial Electronics*, vol. 62, no. 6, pp. 3490–3498, June 2015.

- [74] N. Gyawali, Y. Ohsawa, and O. Yamamoto, "Power management of double-fed induction generator-based wind power system with integrated smart energy storage having superconducting magnetic energy storage/fuel-cell/electrolyser," *IET Renewable Power Generation*, vol. 5, no. 6, pp. 407–421, November 2011.
- [75] R. Takahashi, L. Wu, T. Murata, and J. Tamura, "An application of flywheel energy storage system for wind energy conversion," in *2005 International Conference on Power Electronics and Drives Systems*, vol. 2, 2005, pp. 932–937.
- [76] E. Naswali, C. Alexander, H.-Y. Han, D. Naviaux, A. Bistrika, A. von Jouanne, A. Yokochi, and T. Brekken, "Supercapacitor energy storage for wind energy integration," in *2011 IEEE Energy Conversion Congress and Exposition*, Sept 2011, pp. 298–305.
- [77] X. Li, C. Hu, C. Liu, and D. Xu, "Modeling and control of aggregated super-capacitor energy storage system for wind power generation," in *34th Annual Conference of IEEE Industrial Electronics*, Nov 2008, pp. 3370–3375.
- [78] Y. Chang and J. Yu, "Long term dynamic behavior analysis for power system including wind farms," in *2009. Asia-Pacific Power and Energy Engineering Conference*, March 2009, pp. 1–4.
- [79] Y. Chang and Y. J., "Long term dynamic simulation for power system

- including wind farms,” in *2009 International Conference on Sustainable Power Generation and Supply*, April 2009, pp. 1–6.
- [80] Y. Liu, W. Du, L. Xiao, H. Wang, and J. Cao, “A method for sizing energy storage system to increase wind penetration as limited by grid frequency deviations,” *Power Systems, IEEE Transactions on*, vol. PP, no. 99, pp. 1–9, 2015.
- [81] H. Banakar and B. Luo, C.and Ooi, “Impacts of wind power minute-to-minute variations on power system operation,” *IEEE Transactions on Power Systems*, vol. 23, no. 1, pp. 150–160, Feb 2008.
- [82] T. Lei, M. Barnes, S. Smith, S. Hur, A. Stock, and W. Leithead, “Using improved power electronics modeling and turbine control to improve wind turbine reliability,” *IEEE Transactions on Energy Conversion*, vol. PP, no. 99, pp. 1–9, 2015.
- [83] J. Widen, “Correlations between large-scale solar and wind power in a future scenario for sweden,” *IEEE Transactions on Sustainable Energy*, vol. 2, no. 2, pp. 177–184, April 2011.
- [84] J. Sumaili, H. Keko, V. Miranda, Z. Zhou, A. Botterud, and J. Wang, “Finding representative wind power scenarios and their probabilities for stochastic models,” in *16th International Conference on Intelligent System Application to Power Systems*, Sept 2011, pp. 1–6.

- [85] D. Lee, J. Lee, and R. Baldick, "Wind power scenario generation for stochastic wind power generation and transmission expansion planning," in *2014 IEEE Power and Energy Society General Meeting and Conference Exposition*, July 2014, pp. 1–5.
- [86] J. W. Taylor, P. E. McSharry, and R. Buizza, "Wind power density forecasting using ensemble predictions and time series models," *IEEE Transactions on Energy Conversion*, vol. 24, no. 3, pp. 775–782, Sept 2009.
- [87] N. M. M. Razali and A. H. Hashim, "Backward reduction application for minimizing wind power scenarios in stochastic programming," in *2010 4th International Power Engineering and Optimization Conference*, June 2010, pp. 430–434.
- [88] J. Sumaili, H. Keko, V. Miranda, Z. Zhou, A. Botterud, and J. Wang, "Finding representative wind power scenarios and their probabilities for stochastic models," in *2011 16th International Conference on Intelligent System Application to Power Systems*, Sept 2011, pp. 1–6.
- [89] N. Growe-Kuska, H. Heitsch, and W. Romisch, "Scenario reduction and scenario tree construction for power management problems," in *2003 IEEE Bologna Power Tech Conference Proceedings*, vol. 3, June 2003, pp. 7, 23–26.
- [90] S. Mohammadi, B. Mozafari, S. Solymani, and T. Niknam, "Stochastic

- scenario-based model and investigating size of energy storages for pem-fuel cell unit commitment of micro-grid considering profitable strategies,” *IET Generation, Transmission Distribution*, vol. 8, no. 7, pp. 1228–1243, July 2014.
- [91] M. Cui, D. Ke, Y. Sun, D. Gan, J. Zhang, and B. M. Hodge, “Wind power ramp event forecasting using a stochastic scenario generation method,” *IEEE Transactions on Sustainable Energy*, vol. 6, no. 2, pp. 422–433, April 2015.
- [92] D. Lee, J. Lee, and R. Baldick, “Wind power scenario generation for stochastic wind power generation and transmission expansion planning,” in *2014 IEEE PES General Meeting and Conference Exposition*, July 2014, pp. 1–5.
- [93] R. Xu and D. Wunsch II, “Survey of clustering algorithms,” *IEEE Transactions on Neural Networks*, vol. 16, no. 3, pp. 645–678, May 2005.
- [94] J. MacQueen, “Some methods for classification and analysis of multivariate observations,” in *Proceedings of the Fifth Berkeley Symposium on Mathematical Statistics and Probability, Volume 1: Statistics*. Berkeley, California: University of California Press, 1967, pp. 281–297.
- [95] T. Kanungo, D. M. Mount, N. Netanyahu, C. D. Piatko, R. Silverman, and A. Y. Wu, “An efficient k-means clustering algorithm: analysis and implementation,” *IEEE Transactions on Pattern Analysis and Machine Intelligence*, vol. 24, no. 7, pp. 881–892, Jul 2002.

- [96] D. Michie, D. J. Spiegelhalter, and C. C. Taylor, “Machine learning, neural and statistical classification,” 1994.
- [97] A. Likas, N. Vlassis, and J. J. Verbeek, “The global k-means clustering algorithm,” *Pattern Recognition*, vol. 36, no. 2, pp. 451–461, 2003, biometrics.
- [98] K. R. Žalik, “An efficient k-means clustering algorithm,” *Pattern Recognition Letters*, vol. 29, no. 9, pp. 1385–1391, 2008.
- [99] K. Wagstaff, C. Cardie, S. Rogers, and S. Schroedl, “Constrained k-means clustering with background knowledge,” in *In ICML*. Morgan Kaufmann, 2001, pp. 577–584.
- [100] C. Ding and X. He, “K-means clustering via principal component analysis,” in *Proceedings of the Twenty-first International Conference on Machine Learning*, ser. ICML’04. New York, NY, USA: ACM, 2004, pp. 29–36.
- [101] J. Shlens, “A tutorial on principal component analysis,” *CoRR*, vol. 1404.1100, April 2014. [Online]. Available: <http://arxiv.org/abs/1404.1100>
- [102] I. T. Jolliffe, *Principal Component Analysis, 2nd ed.* New York: Springer-Verlag, 2002.

- [103] H. Abdi and L. J. Williams, "Principal component analysis," *Wiley Interdisciplinary Reviews: Computational Statistics*, vol. 2, no. 4, pp. 433–459, 2010.
- [104] B. C. Geiger and G. Kubin, "Relative information loss in the PCA," *Proc. IEEE Information Theory Workshop*, vol. 1204.0429, pp. 562–566, July 2012.
- [105] "Notrees wind storage project description," Oct. 2011. [Online]. Available: http://www.sandia.gov/ess/docs/pr_conferences/2011/3_Ratnayake_Notrees.pdf
- [106] X. Ke, N. Lu, and C. Jin, "Control and size energy storage systems for managing energy imbalance of variable generation resources," *IEEE Transactions on Sustainable Energy*, vol. 6, no. 1, pp. 70–78, Jan. 2015.
- [107] M. Lu, C. Chang, W. Lee, and L. Wang, "Combining the wind power generation system with energy storage equipment," *IEEE Transactions on Industry Applications*, vol. 45, no. 6, pp. 2109–2115, Nov 2009.
- [108] H. Bludszuweit and J. A. Dominguez-Navarro, "A probabilistic method for energy storage sizing based on wind power forecast uncertainty," *IEEE Transactions on Power Systems*, vol. 26, no. 3, pp. 1651–1658, Aug. 2011.
- [109] A. Tani, M. Camara, and B. Dakyo, "Energy management in the decentralized generation systems based on renewable energy - ultracapacitors

- and battery to compensate the wind/load power fluctuations,” *IEEE Transactions on Industry Applications*, vol. 51, no. 2, pp. 1817–1827, March 2015.
- [110] T. C. Yang, “Initial study of using rechargeable batteries in wind power generation with variable speed induction generators,” *IET Renewable Power Generation*, vol. 2, no. 2, pp. 89–101, June 2008.
- [111] Y. Liu, C. Jiang, J. Shen, and J. Hu, “Coordination of hydro units with wind power generation using interval optimization,” *IEEE Transactions on Sustainable Energy*, vol. 6, no. 2, pp. 443–453, April 2015.
- [112] R. Karki, P. Hu, and R. Billinton, “Reliability evaluation considering wind and hydro power coordination,” *IEEE Transactions on Power Systems*, vol. 25, no. 2, pp. 685–693, May 2010.
- [113] N. Kularatna, “Rechargeable batteries and their management,” *IEEE Instrumentation Measurement Magazine*, vol. 14, no. 2, pp. 20–33, Apr. 2011.
- [114] S. M. Schoenung and W. V. Hassenzahl, “Long- vs. short-term energy storage technologies analysis. a life-cycle cost study. a study for the doe energy storage systems program,” Sandia National Laboratories, Technical report, 2003.
- [115] H. Bindner, T. Cronin, P. Lundsager, J. F. Manwell, U. Abdulwahid, and I. Baring-Gould, “Lifetime modeling of lead acid batteries,” *Risø*

National Laboratory, Technical report, Apr. 2005.

- [116] A. Gee, F. Robinson, and R. Dunn, “Analysis of battery lifetime extension in a small-scale wind-energy system using supercapacitors,” *IEEE Transactions on Energy Conversion*, vol. 28, no. 1, pp. 24–33, Mar. 2013.
- [117] C. Jin, N. Lu, S. Lu, Y. Makarov, and R. Dougal, “Coordinated control algorithm for hybrid energy storage systems,” in *2011 IEEE Power and Energy Society General Meeting*, Jul. 2011, pp. 1–7.
- [118] C. Jin, N. Lu, S. Lu, Y. Makarov, and R. A. Dougal, “A coordinating algorithm for dispatching regulation services between slow and fast power regulating resources,” *IEEE Transactions on Smart Grid*, vol. 5, no. 2, pp. 1043–1050, Mar. 2014.
- [119] H. Madsen, P. Pinson, G. Kariniotakis, H. A. Nielsen, and T. S. Nielsen, “Standardizing the performance evaluation of short-term wind power prediction models,” *Wind Engineering*, vol. 29, no. 6, pp. 475–489, 2005.
- [120] S. D. Downing and D. F. Socie, “Simple rainflow counting algorithms,” *International Journal of Fatigue*, vol. 4, no. 1, pp. 31–40, Jan. 1982.
- [121] W. Li and G. Joós, “Performance comparison of aggregated and distributed energy storage systems in a wind farm for wind power fluctuation suppression,” in *2007 IEEE Power Engineering Society General Meeting*, Jun. 2007, pp. 1–6.

- [122] S. Vazquez, S. M. Lukic, E. Galvan, L. G. Franquelo, and J. M. Carrasco, “Energy storage systems for transport and grid applications,” *IEEE Transactions on Industrial Electronics*, vol. 57, no. 12, pp. 3881–3895, Dec. 2010.
- [123] B. C. Ummels, E. Pelgrum, and W. L. Kling, “Integration of large-scale wind power and use of energy storage in the netherlands’ electricity supply,” *IET Renewable Power Generation*, vol. 2, no. 1, pp. 34–46, Mar. 2008.
- [124] P. Wang, Z. Gao, and L. Tjernberg, “Operational adequacy studies of power systems with wind farms and energy storages,” in *2013 IEEE Power and Energy Society General Meeting*, Jul. 2013, pp. 1–1.
- [125] R. B. Miller, “Bayesian analysis of the two-parameter gamma distribution,” *Technometrics*, vol. 22, no. 1, pp. 65–69, Feb 1980.
- [126] H. T. Le, S. Santoso, and T. Q. Nguyen, “Augmenting wind power penetration and grid voltage stability limits using ess: Application design, sizing, and a case study,” *IEEE Transactions on Power Systems*, vol. 27, no. 1, pp. 161–171, Feb. 2012.
- [127] T. Brekken, A. Yokochi, A. Jouanne, Z. Z. Yen, H. M. Hapke, and D. A. Halamay, “Optimal energy storage sizing and control for wind power applications,” *IEEE Transactions on Sustainable Energy*, vol. 2, no. 1, pp. 69–77, Jan. 2011.

Vita

Yichuan Niu was born in Inner Mongolia, China. He received his B.E. degree in Electrical Engineering from the University of Shanghai for Science and Technology in 2009 and his M.E degree in Power Electronics and Electric Drives from the Tongji University in 2012. Upon his graduation, he worked as an electrical engineer in ABB Inc., Shanghai Branch. The following fall, he enrolled in the Ph.D. program in The University of Texas at Austin, majoring in Electrical Engineering. His research interests include power electronics, wind power plant modeling, and wind power variability control.

Permanent address: yichuan.niu@utexas.edu

This dissertation was typeset with L^AT_EX[†] by the author.

[†]L^AT_EX is a document preparation system developed by Leslie Lamport as a special version of Donald Knuth's T_EX Program.